

Microstructure development during solidification of aluminium alloys

D. Ruvalcaba

This research was carried out under the project MC4.02134b in the framework of the Research Program of the Materials innovation institute M2i (www.m2i.nl), the former Netherlands Institute for Metals Research;



In the Department of Materials Science and Engineering at the Delft University of Technology TUDelft (www.tudelft.nl).



Microstructure development during solidification of aluminium alloys

Proefschrift

ter verkrijging van de graad van doctor
aan de Technische Universiteit Delft,
op gezag van de Rector Magnificus Prof. dr. ir. J.T. Fokkema,
voorzitter van het College voor Promoties,
in het openbaar te verdedigen op woensdag 24 juni 2009 om 10.00 uur

door

Démian Gibrán RUVALCABA JIMÉNEZ

bachelor of engineering in materiaalkunde

Instituto Tecnológico de Saltillo (Mexico)

master of science in materiaalkunde

University of Manchester Institute of Science and Technology (U.K)

geboren te Saltillo, México

Dit proefschrift is goedgekeurd door de promotor:

Prof. ir. L. Katgerman

Copromotor Dr. D.G. Eskin

Samenstelling promotiecommissie:

Rector Magnificus,	voorzitter
Prof. ir. L. Katgerman,	Technische Universiteit Delft, promotor
Dr. D.G. Eskin,	Technische Universiteit Delft, copromotor
Prof. dr. P. Schumacher,	Montanuniversität Leoben
Prof. dr. I.M. Richardson,	Technische Universiteit Delft
Prof. dr. J.T.M. de Hosson,	Rijksuniversiteit Groningen
Prof. dr. R. Boom,	Technische Universiteit Delft & Corus RD&T
Dr. A. Ten Cate,	Corus RD&T
Prof. dr. G.C.A.M. Janssen	Technische Universiteit Delft (reservelid)

Keywords: solidification, aluminium alloys, casting, microstructure.

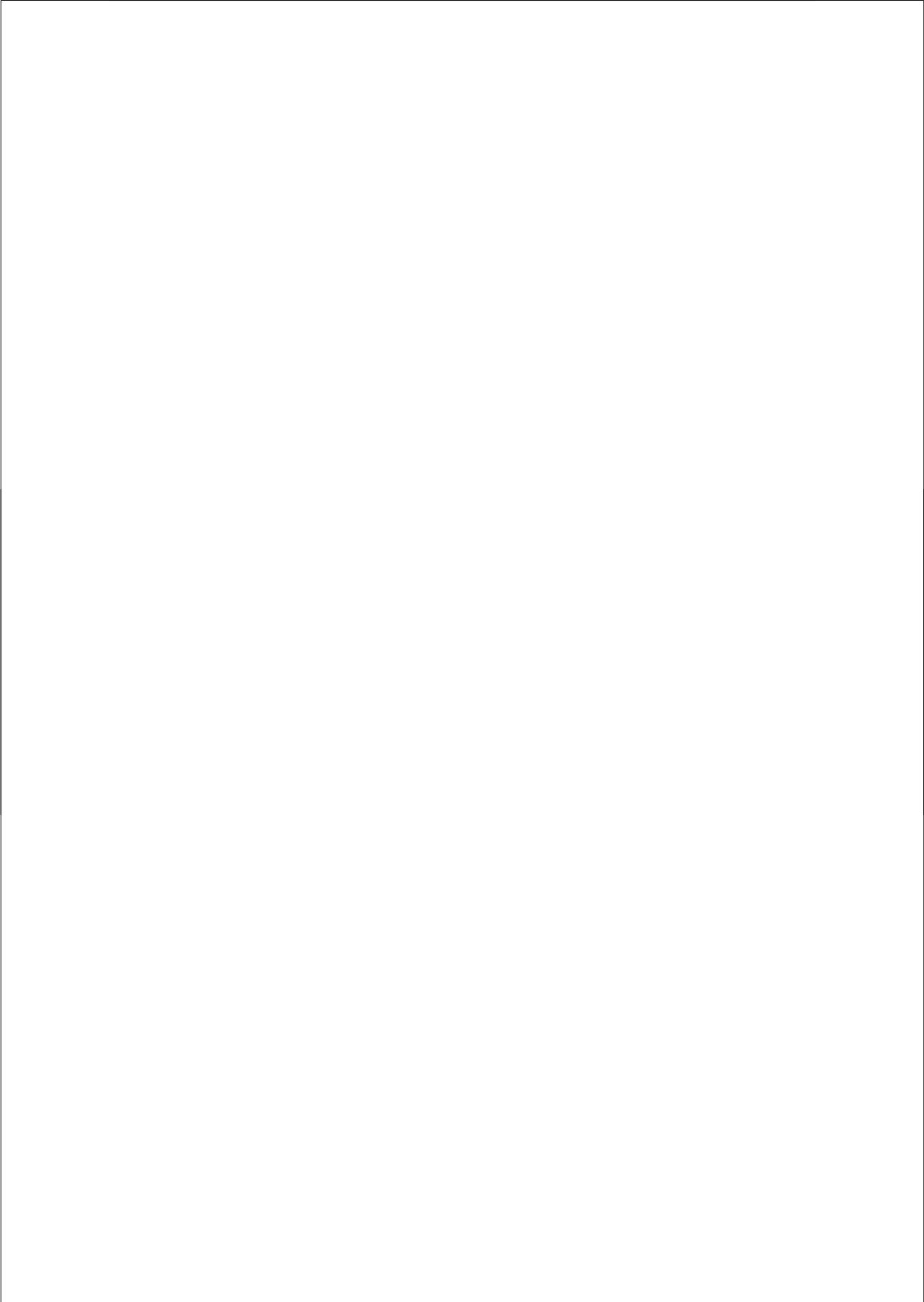
Copyright © 2009 by D. Ruvalcaba

All rights reserved. No part of the material protected by this copyright notice may be reproduced or utilized in any form or by any means, electronic or mechanical, including photocopying, recording or by any information storage and retrieval system, without the prior permission of the author.

ISBN: 9789077172483

Printed in the Netherlands

“This thesis is dedicated to my loving family”



Content

Introduction	1
Thesis Outline	7
Chapter 1. Background	11
1.1. Dendrite Growth during Solidification	12
1.2. Dendrite Growth and Solute Distribution	14
1.3. Morphological Transitions Occurring during Solidification	18
References	28
Chapter 2. Experimental Procedure	31
2.1. Introduction	32
2.2. Interrupted Unconstrained Solidification	36
2.3. Continuous Constrained Directional Solidification	41
2.4. Experimental Procedure for Studying the Microstructure Development and its Influence on the Final Structure	45
References	49
Chapter 3. Microstructure Development during Unconstrained Solidification Conditions	51
3.1. Introduction	52
3.2. Procedure for Data Analysis	54
3.3. Solid Phase Development and Overestimation of Solid Fraction	63
3.4. Solute Distribution of Quenched Structures and Microsegregation	77
3.5. 3D Reconstruction of Instabilities	84
3.6. 3D Estimation of Microstructure Development from 3D Reconstructed Structures	93

3.7. Concluding Remarks	104
References	105
Chapter 4. Microstructure Development during Constrained Solidification Conditions	107
4.1. Introduction	108
4.2. Procedure of Data Analysis	111
4.3. Growth and Coarsening Kinetics during Downward Growth	116
4.4. Growth and Coarsening Kinetics during Upward Growth: Prior to Dendrite Fragmentation	122
4.5. Dendrite Fragmentation due to Solute Enrichment	128
4.6. Concluding Remarks	139
References	142
Chapter 5. Influence of Microstructure Development on the Structure Formation	145
5.1. Introduction	146
5.2. Procedures for Data Analysis	151
5.3. Influence of Coarsening on Non-equilibrium Eutectics	157
5.4. The Role of Fragmentation in the Formation of Duplex Structures	165
5.5. Concluding Remarks	179
References	182
Appendix	185
Summary	191
Samenvatting	195
Publications	199
Acknowledgments	201
About the Author	203

Introduction

Aluminium alloys have been widely utilized in many applications such as construction, aerospace and automotive due to their unique combination of mechanical properties. The main property which characterizes these alloys as being exceptional is the light weight (specific gravity of aluminium is $\sim 35\%$ that of iron). This property along with specific strength and toughness makes aluminium alloys a good candidate material for many applications (e.g. beverage cans, construction materials and automotive body panels) [1]. The main route for producing alloys is casting. The semi-continuous casting process is the main practice for obtaining aluminium alloys which, after the process, are referred to as cast ingots or billets. Afterwards, the cast ingot is processed into the final wrought product through deformation and heat treatment routines, the first of which is homogenization.

The main process to take place during casting, and which is of paramount importance during production in determining the quality of the ingot, is solidification. The final properties of a cast aluminium alloy depend on the final microstructure and defects developing during solidification. Defects that develop during casting such as: macrosegregation (i.e. large-scale inhomogeneities in chemical composition), porosity (i.e. entrapped gas and shrinkage cavities) and hot tearing (i.e. crack formed during solidification) depend on the microstructure development [2]. Even when an ingot is submitted to thermal treatment after casting, such defects may still be imprinted in the structure affecting the final properties.

Accordingly, better understanding of the appearance of casting defects requires experimental studies on microstructure development during solidification.

Evolution of microstructure phenomena such as solid fraction, phase morphology and dendrite coherency during solidification influences permeability and melt flow which in turn influences the formation of cast defects [2-4]. During continuous casting, microstructure development occurs within the sump, which is a zone consisting of a liquid pool followed by a transition region. The transition region is composed by the slurry (liquid with suspended solid) and the mushy zone (liquid within a solid network). This region is represented in the non-equilibrium diagram of the alloy between the liquidus and non-equilibrium solidus temperatures [3,4].

Much of the numerical computer modelling and simulation of solidification analysis has recently advanced significantly. These studies have refined existing fundamental models on structure development during solidification. The models cover a large range of length scales, going from the microstructure (in the range of μm) up to the macrostructure (in the range of m) [5]. Experimental studies in solidification of alloys have been also extensive and have provided basic knowledge on microstructure development. However, until now, there has not been a complete understanding on microstructure development of aluminium alloys and on the formations of cast defects. Much of the experimental studies on microstructure development are based on directionally solidified samples and assuming steady-state conditions. During casting, according to casting dimensions, casting shape and heat flow, solidification implies development of structures which may interact with each other. This affects the development of microstructure through dendrite impingement and interaction, which in turn influences the development of cast defects.

There are several experimental techniques employed in order to follow the microstructure development of aluminium alloys, e.g. the calorimetric technique [6], the optical technique [7], interrupted solidification and optical

microscopy [8-14] and X-ray microscopy [15-17]. The first two methods rely on the use of already “known” solidification characteristics of the alloy (e.g. partition coefficient) which are based on the assumption of equilibrium solidification. These two methods obviously would not give accurate results, especially when non-equilibrium solidification is taking place. Moreover, they do not demonstrate the microstructure development involving morphology of phases which is an important aspect in determining permeability. The last two techniques allow studying the actual microstructure that develops during solidification. These techniques permit the evaluation of: solid fraction, morphology of phases, phase connectivity and segregation. On the other hand, both have their limitations in studying solidification of aluminium alloys.

Interrupted solidification of microstructures is usually done by freezing samples within the transition region by using a quenching medium (e.g. water). This technique provides very adequate results when quenching close to the eutectic reaction of the respective solidifying alloy. Moreover, this technique can be used to study development of microstructure during isothermal holding [11-14]. This technique, however, does not provide reliable results when quenching at higher temperatures during continuous solidification. The main problem is overestimation of solid fraction when quenching at high temperatures [11-14]. This overestimation problem is based on two solidification extremes which are the lever rule and the Gulliver-Scheil model. The solidification path of an alloy should fall within these limits, since these models are based on the partition of elements between the solid and liquid, which in turn determines the amount of these phases. Also, local chemical compositions of the liquid phase cannot be studied from the quenched samples by using techniques such as Electron Probe X-ray Micro Analysis (EPMA). This last drawback is mainly due to the formation of instabilities (or finer continuation of growth of solid phase) in the solidifying liquid which completely erases any possibility to get accurate

measurements about chemical composition. In order to understand the overestimation of solid from quenched structures other analysis techniques should be employed. For example, 3D structure reconstruction of samples exhibiting overestimation may reveal features which cannot be observed from 2D observed structures.

X-ray microscopy, on the other hand, can provide in-situ analysis of microstructure development during solidification. This technique has attracted more recently great attention and, due to improvements in X-ray detectors and the use of 3rd generation synchrotron radiation sources, the analysis of solidifying alloys by this technique has provided new insight into microstructure development during solidification [15-17]. On contrast this technique has the following limitations: 1) only a certain range of materials is suitable to produce enough contrast that can reveal the structure during solidification, 2) the size of the samples to be studied have to be small enough to permit X-ray penetration, 3) the acquisition of the composition within extremely dense phases is not possible (e.g. within the solid phase) and 4) the technique is expensive, time consuming and the cooling rates of the solidifying specimen should be very slow limited by the time resolution of the technique [15-17].

In the present study, both techniques, the quenching technique coupled with optical microscopy and in-situ observations of microstructure development during solidification by using X-ray microscopy, were used to understand microstructural changes during solidification (such as solid fraction evolution, microsegregation, fragmentation, coarsening, morphology of the solid phase, etc). The quenching technique and optical microscopy complemented with 3D microstructure reconstruction allowed the study of the solid fraction evolution, morphology of the solid phase and microsegregation within the solid phase

(under unconstrained growth conditions); whereas, X-ray microscopy allowed the study of fragmentation, coarsening and constitutional variations in the liquid phase during directional solidification (or constrained growth conditions).

Furthermore, cast defects are influenced by variations in local chemical composition and transitions in morphology during solidification. In this thesis, the influence of microsegregation and fragmentation on the formation of the final structure, on the macro-scale level (e.g. macrosegregation and grain size), is demonstrated.

Moreover, at the moment it has not been fully clarified the differences of microstructure development during directional solidification (i.e. constrained growth) and during non-directional solidification (i.e. unconstrained growth). The thesis differentiates the studies according to the solidification condition in order to clearly demonstrate the results.

This thesis demonstrates new insights into microstructure development. The study on microstructure development during solidification presented here reveals aspects which can improve our understanding not just in microstructure development, but also into the formation of cast defects from the fundamental point of view based on experimental observations.

References

- [1] E.A. Starke Jr., Aluminum Alloys: Properties and Applications, Encyclopedia of Mater: Sci. and Tech., Elsevier Sci. Ltd. UK, 2001.
- [2] A.K. Dahle, D.H. StJohn, Acta Mater. 47 (1999) 31.
- [3] M.C. Flemings, Solidification Processing, McGraw-Hill, New York, 1974.
- [4] W. Kurz, D.J. Fisher, Fundamentals of Solidification, 3rd ed. Trans. Tech. Publications, Aedermannsdorf, Switzerland, 1992.
- [5] W.J. Boettinger, S.R. Coriell, A.L. Greer, A. Karma, W. Kurz, M. Rappaz, R. Trivedi, Acta Mater. 48 (2000) 43.
- [6] S.W. Chen, C.C. Huang, Acta Metall. 44 (1996) 1955.
- [7] S. Steinbach, L. Ratke, Scripta Mater. 50 (2004) 1135.
- [8] R. Trivedi, S. Liu, P. Mazumder, E. Simsek, Sci. Tech. Adv. Mater. 2 (2001) 309.
- [9] J. Lacaze, G.R.J. Lesoult, Mater. Sci. Eng. A 173A (1993) 119.
- [10] S.D. McDonald, K. Nogita, A.K. Dahle, Acta Mater. 52 (2004) 4273.
- [11] M. Rettenmayr, O. Pompe, J. Cryst. Growth 173 (1997) 182.
- [12] Ø. Nielsen, S.O. Olsen, Transactions of the American Foundryman's Society 110 (2002) paper 02-096.
- [13] O. Pompe, M. Rettenmayr, J. Cryst. Growth 192 (1998) 300.
- [14] E. Tzimas, A. Zavaliangos, J. Mater. Sci. 35 (2000) 5319.
- [15] R.H. Mathiesen, L. Arnberg, Acta Mater. 53 (2005) 947.
- [16] T. Schenk, H. Nguyen Thi, J. Gastaldi, G. Reinhart, V. Cristiglio, N. Mangelinck-Noël, H. Klein, J. Härtwig, B. Grushko, B. Billia, J. Baruchel, J. Cryst. Growth 275 (2005) 201.
- [17] O. Ludwig, M. Dimichiel, L. Salvo, M. Suery, P. Falus, Metall. Mater. Tras. A 36A (2005) 1515.

Thesis Outline

The structure of this thesis was designed as follows:

Chapter 1 illustrates, based on literature, fundamentals about microstructure development during solidification. This is demonstrated along with the most relevant and significant concepts which describe the topics that are treated in this thesis. Aspects about microstructure development during both unconstrained and constrained growth of aluminium alloys are discussed¹. The chapter contains information about: dendrite growth, solid fraction evolution, coarsening, microsegregation, fragmentation, and columnar-to-equiaxed transition. These phenomena are the most important aspects studied, since they determine not just the final structure but also the formation and evolutions of cast defects.

Chapter 2 describes the procedures for sample preparation along with the description of both experimental techniques employed for the present studies (in Chapter 3 and 4). These techniques are: interrupted solidification (for unconstrained solidification) and directional solidification and X-ray microscopy (for constrained solidification). This chapter only focuses in the main aspects about the samples and experimental set-up. Specific details about analysis of results in the unconstrained and constrained solidification studies are presented at the beginning of Chapters 3 and 4 respectively. Finally, the sample preparation and experimental techniques for studying the microstructure

¹ Unconstrained growth or solidification is referred here to as solidification occurring with no directionally imposed thermal gradient and thus having asymmetrical dendritic growth. On the other hand, constrained growth or solidification is defined as solidification occurring with and imposed thermal gradient which enables growth of dendrites in a single direction(i.e. directional solidification).

development and its influence on the final structure is described (for the studies shown in Chapter 5).

Chapter 3 is divided in subchapters which contain different aspects of structure development during unconstrained growth. First, the procedure for the analysis of results is presented. Then, the studies of solid fraction development, overestimation of solid fraction, microsegregation within the solid phase, morphology development during quenching and 3D microstructure development are presented. Based on the results, new insights into coarsening, coalescence and solid fraction development are given based on qualitatively and semi-quantitatively analysis of evolving 3D microstructures under unconstrained solidification conditions.

Chapter 4 is also divided in subchapters, where at the beginning the procedure for the analysis of results is presented. The following subchapters demonstrate microstructure development during continuous directional solidification experiments (i.e. constrained growth) focusing in the following aspects: coarsening during downward and upward solidification and fragmentation. In this chapter a new mechanism of fragmentation is demonstrated which can be more feasible to occur during solidification. Also, new insights into local growth and coarsening kinetics are presented. All these results are based on in-situ solidification experiments.

Finally, Chapter 5 contains the procedure for the analysis of results and two subchapters which demonstrate the effect of microstructure development, i.e. coarsening and fragmentation, on the developing structure during solidification. This last chapter highlights the importance of understanding fundamentals about microstructure development during the entire solidification range from experimental studies in order to understand the formation of cast defects and

final structure. The analysis of results in this Chapter is in part based on the experimental methods developed in Chapter 3.

The structure of the thesis was designed in this way so that the reader can adapt progressively into the main concepts described in the thesis. This structure also allows for better appreciation of the results avoiding redundancies and confusion.

Chapter 1

Background

The fundamental aspects related to microstructure development during solidification of alloys are presented here. Growth, solute distribution and morphological transitions that occur during solidification such as: coarsening, coalescence, fragmentation and the columnar-to-equiaxed transition are the main features illustrated in this chapter. These evolving morphological phenomena will influence the formation of cast defects and eventually final structure. Attention is given to the dendritic structure, which is the typical ramified structure found in castings.

This Chapter describes fundamental concepts which have been well documented in literature [e.g. 1, 2] and also the most relevant literature related to the aspects studied in this thesis.

1.1. Dendrite Growth during Solidification

The most common morphology evolving during the solidification of aluminium alloys is a ramified tree-like structure called “dendrite”. This terminology is derived from the Greek word “dendros” which means tree. Dendrites form as a result of the crystallographic structure and preferred growth orientation of the alloy (i.e. [100] in aluminium alloys). Such ramified structure develops high-order branches, and their growth is influenced by the solidification conditions [1-3]. Figure 1.1 shows a dendrite structure which was revealed after liquid drainage of a solidifying solid-liquid mixture.

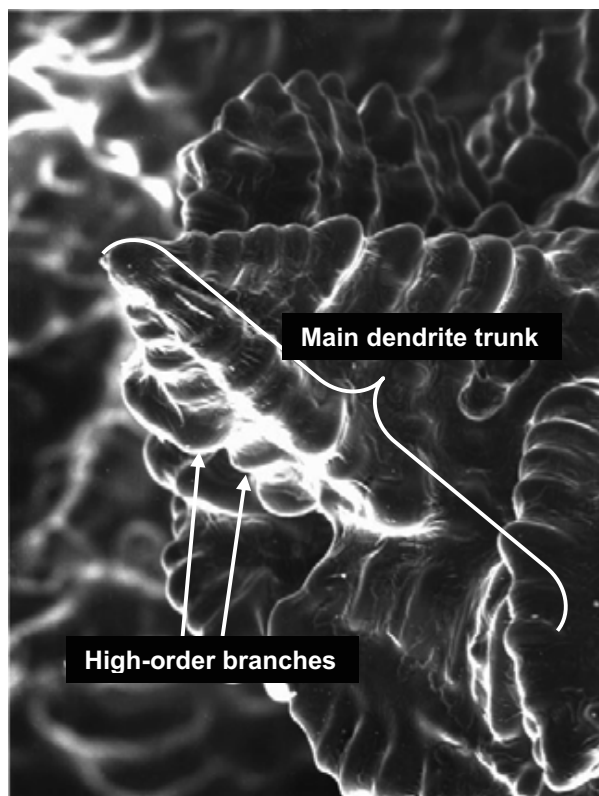


Figure 1.1. Dendrite revealed after liquid drainage of a solidifying metal. The main dendrite trunk and high-order branches are shown [4].

The final structure of a solidified casting may be conformed by a mixture of columnar and equiaxed dendrites. Three structures can be found in solidified castings i.e. a chill zone, a columnar zone and an equiaxed zone (Figure 1.2). Finer equiaxed dendrites develop at the first zone that forms on the chilled surface (chill zone) due to fast freezing of the structure during cooling. Following by these equiaxed dendrites, columnar dendrites evolve towards the middle part of the cast. At a certain point coarser equiaxed dendrites develop. The type of structures that form in a solidifying cast depends on the cooling conditions and type of alloy that is being cast [1-3].

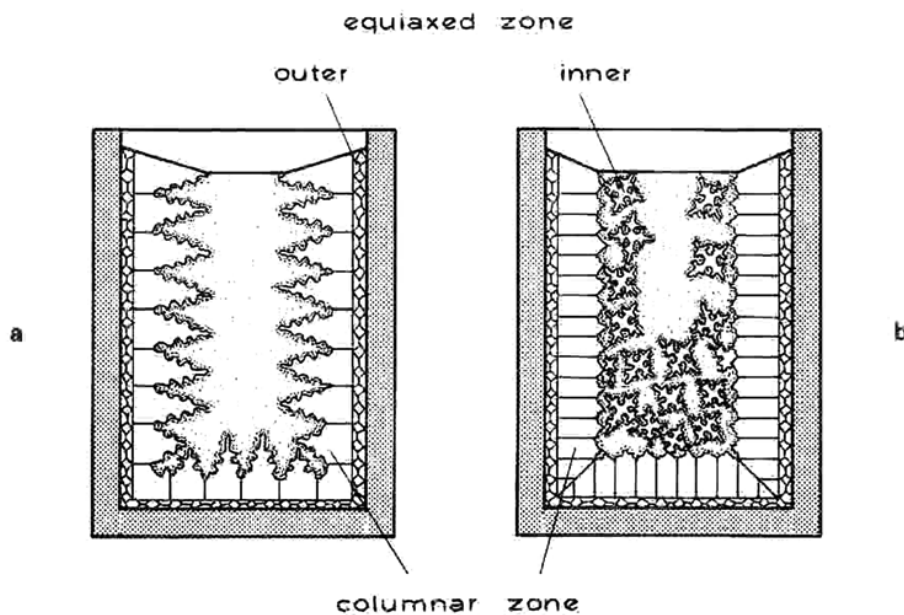


Figure 1.2. Structural zones developing during casting, where: (a) demonstrates the development of columnar dendrites after finer equiaxed dendrites have been formed (stage at which the heat extraction is towards the solid phase) and (b) shows the formation of coarse equiaxed dendrites after the formation of columnar dendrites (stage at which heat is released from the solid phase into the columnar dendrites and also into the liquid) [2].

The development of dendrite structures has been of great interest over the years [1,2]. In the case of solidifying aluminium alloys, the development of dendrites during solidification influences permeability which in turn affects the dendrite growth conditions. This development of structure influences the formation of cast defects such as macrosegregation (i.e. large-scale chemical distribution), porosity (i.e. holes or gaps) and hot tearing (i.e. crack formed during solidification) [1-5]. Development of dendrites involves phenomena such as dendrite growth, coarsening and dendrite fragmentation which depend on the solidification conditions.

1.2. Dendrite Growth and Solute Distribution

1.2.1. Undercooling promoting growth

As soon as the solidification of an alloy starts, temperature gradients start to build up at the solid-liquid interface provoking a localized depression in local liquid temperature i.e. thermal undercooling ΔT_t . Also, due to solute partitioning between the solid and liquid phases, rejection of solute occurs at the solid-liquid interface into the liquid (i.e. when solute has less solubility in the solid compared to that in the liquid) leading to solute gradients from the interface deep into the liquid lowering the melting temperature i.e. constitutional undercooling ΔT_c . Geometrical gradients according to the evolving shape of the solid-liquid interface also lowers the melting temperature, according to the Gibbs–Thomson capillarity effect, i.e. undercooling due to curvature change ΔT_r . The total undercooling which provokes growth at the interface will then be $\Delta T = \Delta T_t + \Delta T_c + \Delta T_r$.

During constrained growth (i.e. directional solidification), the thermal undercooling at the dendrite tips is considered to be insignificant, since the heat (latent heat of solidification) tends to be released opposite to the growth directions towards the solidifying dendrites, thus $\Delta T_i \sim 0$. On the other hand, during equiaxed growth and unconstrained growth (free dendritic growth), some heat would be diffused into the liquid affecting the total undercooling.

The effect of solute partitioning on constitutional undercooling is illustrated in Figure 1.3. This figure demonstrates the nominal composition of the alloy as C_0 and the partition coefficient k which provokes the build up of a diffusion boundary layer in the liquid ahead of the solid-liquid interface $\delta = D/V$ (D is the diffusion coefficient of the solute element in the liquid and V is the growth rate). The temperature gradient due to heat flux will impose a temperature at the interface T_q which, along with the constitutional undercooling $\Delta T_0 = T_L(C_0) - T_S(C_0)$ induced by the solute gradient at the interface $\Delta C_0 = C_0/k - C_0$ in the direction of growth z , will depress the melting temperature of the evolving interface (dashed area in Fig. 1.3) [1,2]. The microstructure evolves during solidification according to the changes in undercooling which it turn is determined by the solidification conditions; thus, influencing eventually the formation of the final structure of the alloy.

1.2.1. Solute distribution and solid fraction evolution

The partition coefficient k determines not only the rejection of solute into the liquid, but also solute distribution in the evolving solid. In the case of alloys, k is determined by the phase diagram of the respective alloy. This coefficient depends on the solute solubility in the solid and liquid following the solidus and liquidus lines in the phase diagram lines respectively. The partition coefficient

or distribution coefficient is described as $C_S^* = kC_L^*$, where C_S^* is the solute content in the solid at the solid-liquid interface and C_L^* is the solute content in the liquid at the solid-liquid interface at a given temperature.

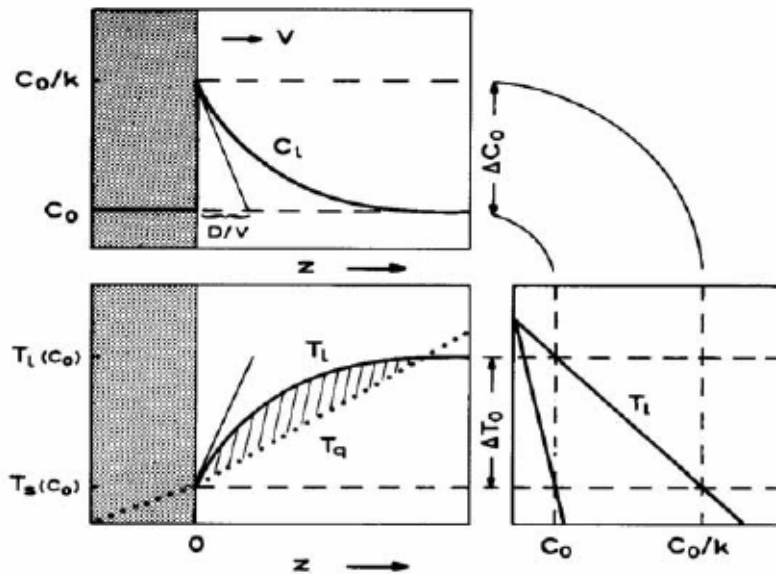


Figure 1.3. Constitutional undercooling at the solid-liquid interface [2].

During the solidification of alloys assuming local equilibrium at the solid-liquid interface (i.e. the solute content in the solid and liquid at the solid-liquid interface follows the equilibrium diagram) solidification follows a route between two extremes. The first extreme route is when it is considered that solute has infinite diffusivity in the solid according to the partition coefficient of the alloy. In this case, at first, the starting composition of the solid is kC_0 which then immediately adjusts to C_S on cooling following the solidus line. Since the amount of solute distribution determines the ratio of solidifying phases (solid and liquid), the amount of solid phase f_S can be determined by following the equilibrium diagram from the lever rule:

$$f_S = \frac{C_L - C_0}{C_S - C_L}, \quad (1.1)$$

This solidification route is called equilibrium or lever rule.

On the other hand, when solute has negligible diffusivity in the solid, the fraction of solid differs from that evolving during equilibrium or lever rule solidification. When solute is left imprinted in the evolving solid at the interface following the solidus line (according to k) due to limited diffusivity, the solid fraction evolves as follows:

$$f_{SS} = 1 - \left(\frac{C_S^*}{kC_0} \right)^{\frac{1}{k-1}}, \quad (1.2)$$

Equation 1.2 is known as the Gulliver–Scheil approximation. Since the solute content is left imprinted in the evolving interface in the solid, the solute distribution has a profile denominated “coring” or microsegregation. This second route is called non-equilibrium solidification or Gulliver–Scheil approximation. The solid fraction in the Gulliver–Scheil approximation is less than in the lever rule.

Both, the lever rule and the Gulliver–Scheil approximation assume local equilibrium at the solid-liquid interface during solidification. The denotation of “global” equilibrium and non-equilibrium solidification in the lever rule and in the Gulliver–Scheil approximation respectively should not be confused with “local” equilibrium at the interface which applies to both solidification routes.

Other solidification models consider other parameters which can influence the partition of solute k , e.g. growth rate. When considering normal dendritic growth conditions (normal convective conditions and low cooling rates), the solidification pattern (solid fraction as a function of temperature) should fall within the limiting extremes, i.e. Gulliver–Scheil and lever rule [1,2].

A so-called transition zone develops continuously during columnar dendrite growth (constrained growth). Under these conditions the solidification path (i.e. solid fraction vs temperature) lies within the mushy zone as shown in Figure 1.4. It is of great importance to be acquainted with the solidification path of alloys since it determines their structure transitions which in turn influences permeability and thus the formation of cast defects during solidification as described next.

1.3. Morphological Transitions Occurring during Solidification

During dendritic growth, morphological transitions can occur during solidification. Morphological phenomena, such as coarsening, coalescence and fragmentation, usually develop along with the dendrite growth and play an important role in determining the evolution of the cast structure and eventually the final structure.

Another important morphological transition occurring during solidification is the columnar-to-equiaxed transition (CET). This transition can influence greatly the structure development (Fig. 1.2). The CET is still not well

understood, especially in non-grain refined alloys and where natural convection is present during solidification.

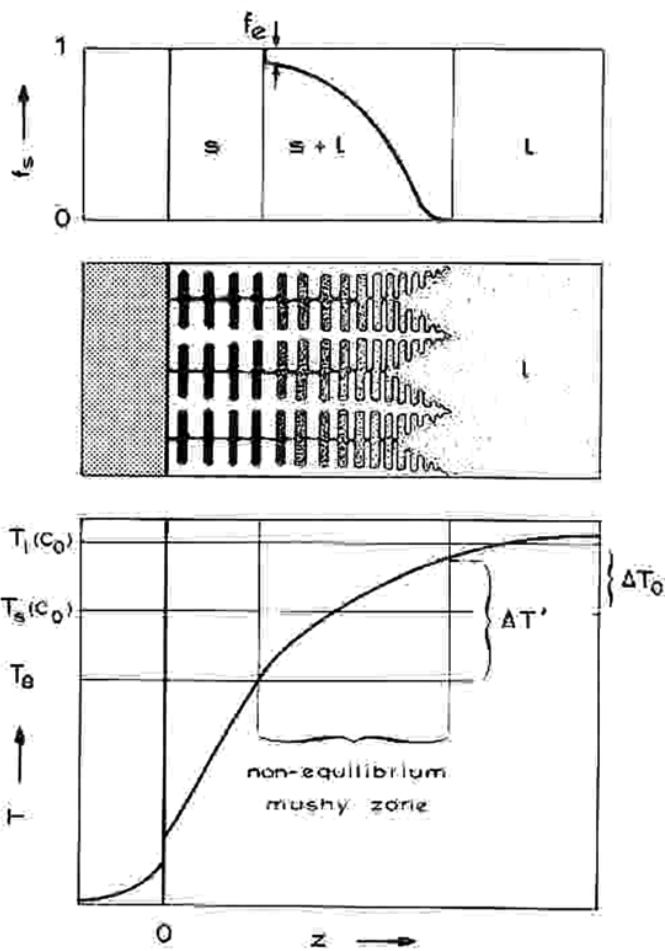


Figure 1.4. Solidification path and temperature profile continuously developing during directional solidification in the transition mushy zone [2].

The fundamental aspects about coarsening, coalescence, fragmentation and CET are described here.

1.3.1. Coarsening, fragmentation and coalescence

During solidification, material flux may occur within dendrite branches due to differences in curvature and compositional gradients. These differences in curvature and composition can influence solute diffusivity in the solid and liquid. Strong dendrite branches having low curvature will tend to coarsen while weak dendrite having a high curvature will tend to be dissolved. Solvent transport then occurs from the weak branches to the strong branches and vice versa for the solute element. Coarsening alters the growth of dendrites and influences the morphology of branches. The influence of curvature on the composition in the liquid at the solid-liquid interface has been defined by the Gibbs–Thomson equation [1,2]:

$$C_L^* = C_\infty + 2l_c H, \quad (1.3)$$

where C_L^* is the solute content in the liquid at the solid-liquid interface, C_∞ is the equilibrium composition in the liquid at the interface, l_c is the capillarity length and H is the mean curvature of the interface, i.e. $(1/R_1 + 1/R_2)/2$, where R_1 and R_2 are the principal radii of curvature. Differences in curvature lead to local solute gradients in the liquid at the interfaces of the dendrite boundaries which in turn provokes solute flux and material deposition or dissolution (remelting). In the case of remelting, a depression of the equilibrium melting temperature ΔT_r occurs at the interface according to [1,2]:

$$\Delta T_r = \frac{\sigma T_L}{r \rho_s H_f}, \quad (1.4)$$

where σ is the solid-liquid surface energy, T_L is the equilibrium liquidus temperature, r is the radius of curvature, ρ_S is the solid density and H_f is the heat of fusion.

A change in secondary dendrite arm spacing has been related to coarsening during solidification. Figure 1.5 demonstrates the situation when remelting of a weak arm (slim arm in the middle in Fig. 1.5a) and thickening of neighbouring arms by material deposition (arms at both sides in Fig. 1.5a) leads to an increase in secondary dendrite arm spacing SDAS also designed as λ_2 .

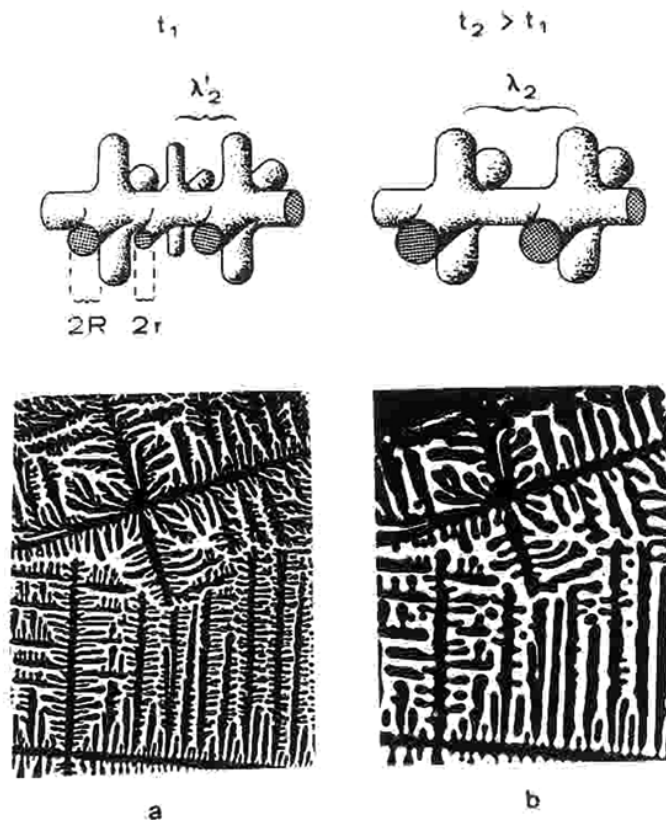


Figure 1.5. Secondary dendrite arm spacing SDAS (or λ_2) related to coarsening, where (a) indicates the spacing prior to coarsening and (b) the spacing after coarsening [2].

A relationship between the SDAS and local solidification time has been described as:

$$SDAS = At_S^n, \quad (1.5)$$

where A is the alloy-sensitive constant, t_S is the local solidification time and n is a constant. The coarsening exponent, defined as n , has been generally related to values between 0.3 and 0.5. The local solidification time is the time that takes to the alloy to go from liquid to solid. The SDAS is also inversely proportional to the cooling rate (V_c) i.e. $t_S^n = V_c^{-n}$. Figure 1.6 shows the SDAS as a function of local solidification time, it can be seen that at prolonged solidification times (i.e. lower cooling rates) the SDAS increases. Materials transport and deposition in stronger dendrite branches, i.e. coarsening, is enhanced when increasing the local solidification time, since more time is available for high-order branches to develop [1,2].

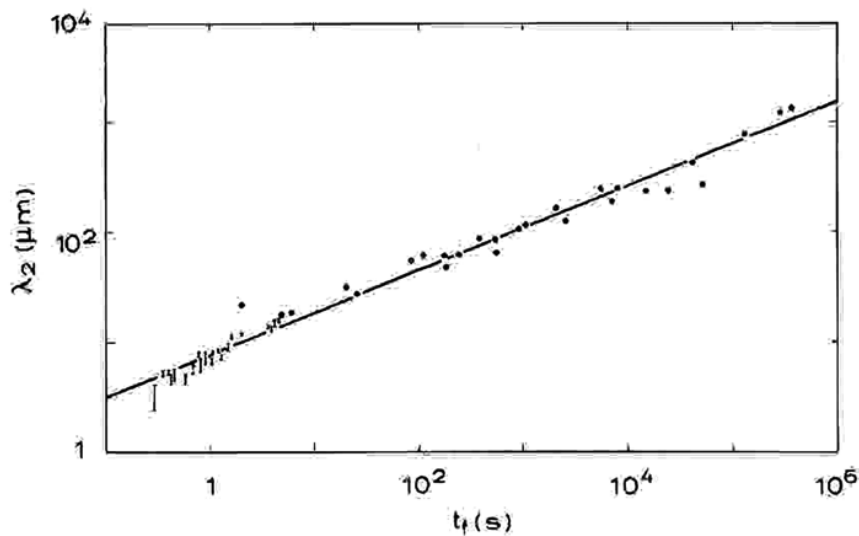


Figure 1.6. SDAS (λ_2) as a function of local solidification time [2].

Several coarsening mechanisms have been described in literature, these are:

- 1) radial dissolution of weak arms and thickening of large ones [6],
- 2) dissolution of roots of weak arms (which may lead to fragmentation) [6-8],
- 3) dissolution from tip to root of weak arms [9], and
- 4) coalescence between arms [10].

These mechanisms leading to morphology transitions of dendrites are illustrated in Figure 1.7. Liquid flow or permeability between dendrite arms (interdendritic flow) during solidification depends greatly on the transition of dendrite arm morphology.

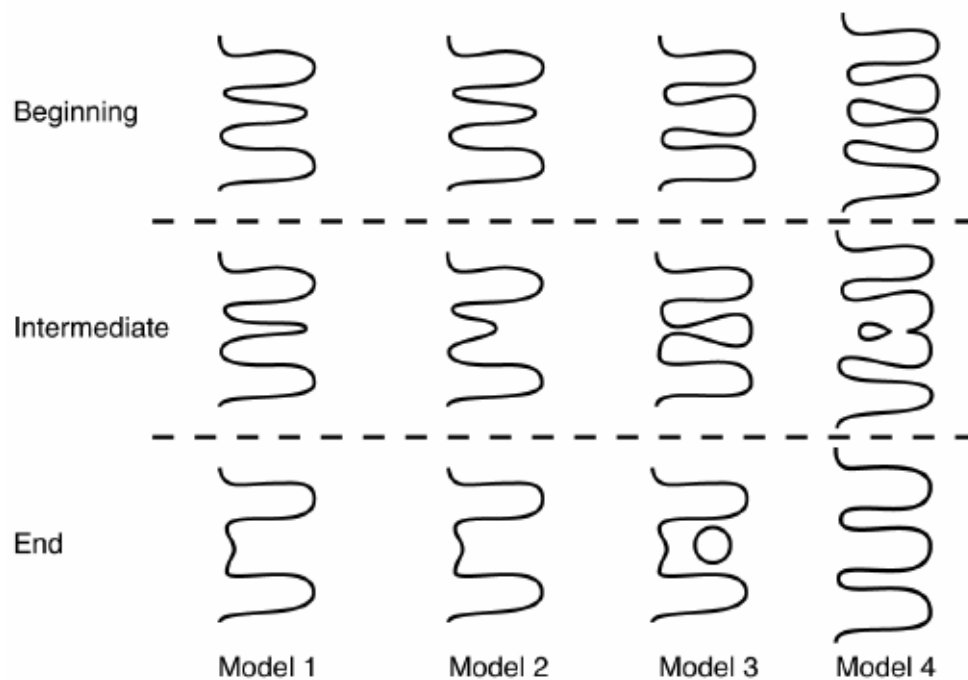


Figure 1.7. Coarsening mechanisms occurring during solidification where: Model 1 refers to radial remelting of arms, Model 2 refers to remelting from tip to root, Model 3 refers to root remelting and Model 4 refers to coalescence [11].

1.3.2. Columnar-to-equiaxed-transition (CET) and fragmentation

During solidification of non-grain refined alloys, the columnar dendritic structure may change to equiaxed during solidification (CET). This is an important transition since it will determine the formation of cast defects during solidification. Different theories for the CET have been formulated based on experimental observations and these are:

- 1) nucleation of equiaxed dendrites due to constitutional undercooling [12],
- 2) free crystals dragged from the chilled surface [13,14],
- 3) dendrite arm remelting and fragmentation [15],
- 4) showering of crystals from the surface [16], and
- 5) mechanical breakdown of dendrite arms [17].

Thermo-solutal convection and fluid flow may affect the structure formation during casting influencing CET according to the mechanisms shown above. On the other hand, the CET that may occur during natural-convective solidification conditions has not yet been completely understood. Detachment of crystals from the dendritic network during solidification, so-called fragmentation, has been proposed as one of the feasible mechanisms to cause CET [18-22], grain refinement and the appearance of stray crystals in commercial castings [1, 2].

1.3.3. Microstructure transitions influencing cast defects

The global structure transition from slurry to mush is determined by the transitions in microstructure mentioned above. The slurry–mush shift occurs within the solid–liquid transition region in the phase diagram of the alloy.

Slurry is the region (or solidification stage) where solid particles are suspended in the liquid and mush is where solid becomes interconnected forming a continuous dendritic network. The starting point where dendrites meet and start to impinge depends on the microstructure development involving: coarsening, coalescence, fragmentation and more drastic transitions such as the columnar-to-equiaxed transition.

During DC casting, the appearance of cast defects during solidification, such as macrosegregation, porosity and hot-tearing, influences the progress of the casting and eventually the quality of the final billet. The evolution of such defects depends on the progress of the interdendritic liquid filling during solidification which depends on the permeability of the evolving structure. Permeability depends on the microstructure evolution which determines the slurry-mush shift. Accordingly, a lack of interdendritic feeding could lead to voids, or even worse to crack formation i.e. hot tearing. Also, the chemical distribution will depend on permeability. A permeable structure will permit a more homogeneous chemical distribution than a less permeable structure.

The Carman–Kozeny relationship determines permeability according to solid fraction f_s and surface-to-volume ratio S_V which determine the amount and morphology of solid, respectively. Permeability K , thus, can be determined as follows:

$$K = \frac{(1 - f_s)^3}{CS_V^2}, \quad (1.6)$$

where C is an adjustable constant.

Also, the K can be determined by considering the secondary dendrite arm spacing λ_2 as the structural length-scale instead of S_V from [23]:

$$K = \frac{[1 - f_s]^3}{f_s^2} \frac{\lambda_2^2}{180}, \quad (1.7)$$

It can be noticed that the solid fraction and dendrite arm spacing influence permeability. Thus, precise knowledge on microstructure transitions occurring during solidification is required in order to determine permeability accurately and thus to predict the formation of cast defects within a cast.

The formation of complex structures such as duplex structures (i.e. structures conformed by fine and coarse grains) have been commonly found in cast ingot produced from DC casting. These structures are related to macrosegregation i.e. variation in solute distribution in relation to the cross-section of a casting. This relation is determined by the partition of elements during solidification. Solute lean grains found in a duplex structure are usually related to the coarse grains while more solute-containing grains are related to fine and less developed grains. Coarse grains usually denominated as floating grains are contributors of the negative centreline segregation. The formation of floating grains is a phenomenon that accompanies the complex solidification process occurring during continuous casting where thermo-solutal convection, shrinkage, melt flow etc. determine the solidification conditions. The theory on the formation of floating grains and its relation to macrosegregation has not yet been fully developed. The evolution of duplex structures depends on microstructure development and corresponding transitions in structure [24-33].

The formation of non-equilibrium eutectics is also related to the chemical distribution in the structure which accompanies the formation of grains with the

partition of solute elements of the alloy. This process is called microsegregation. It is important to understand the formation of non-equilibrium eutectics since this structural characteristic it is related to hot-tearing sensitivity [28]. During non-equilibrium solidification it is expected to have more liquid solidifying as eutectic (i.e. non-equilibrium eutectics) as compared to equilibrium solidification (as discussed in Section 1.2.1). This is due to a lack of diffusion of solute in the solid phase leading to solute saturation in the liquid. The relation between the amount and distribution of non-equilibrium eutectics with cooling rate has not been clarified especially when considering the variation in the structure length scale upon solidification.

The final structure will depend on the evolution of the features mentioned above. Thus, it is required, especially by means of experimental analysis, to understand how the microstructure develops during solidification by considering all structure phenomena occurring during the process.

References

- [1] M.C. Flemings, Solidification Processing, McGraw-Hill, New York, 1974.
- [2] W. Kurz, D.J. Fisher, Fundamentals of Solidification, 3rd ed. Trans. Tech. Publications, Aedermannsdorf, Switzerland, 1992.
- [3] B. Chalmers, Principles of Solidification, Wiley, New York, 1964.
- [4] L.M. Hogan, Dendritic Solidification of Crystals, Encyclopedia of Materials: Science and Technology, Elsevier Science Ltd. 2001, 1913.
- [5] A.K. Dahle, D.H. StJohn, Acta Mater. 47 (1999) 31.
- [6] T.Z. Kattamis, J.C. Coughlin, M.C. Flemings, Trans. TMS_AIME 239 (1967) 1504.
- [7] A.A. Chernov, Kristallografiya 1 (1956) 583.
- [8] M.O. Klia, Kristallografiya 65 (1956) 576.
- [9] M. Kahlweit, Scripta Met. 2 (1968) 251.
- [10] S.C. Huang, M.E. Gliksmann, Acta Metal. 29 (1981) 717.
- [11] R. Mendoza, Morphological and Topological Characterization of Coarsened Dendritic Microstructures, PhD Thesis, Northwestern University, Evanston Illinois, 2004.
- [12] W.C. Winegard, B. Chalmers, Trans. ASM 46 (1954) 1214.
- [13] R. Genders, J. Inst. of Metals 35 (1926) 259.
- [14] B. Chalmers, J. Aust. Inst. of Metals 8 (1963) 255.
- [15] K. Jackson, J. Hunt, D. Uhlmann, T. Seward, Trans. AIME 236 (1966) 149.
- [16] R.T. Southin, Trans. Met. Soc. AIME 239 (1967) 18.
- [17] A. Ohno, T. Motegi, H. Soda, Trans. ISIJ 11 (1971) 18.
- [18] R.H. Mathiesen, L. Arnberg, P. Bleuet, A. Somogyi, Metall. Mater. Trans. A 37A (2006) 2515.

- [19] A. M. Mullis, R. F. Cochrane, *J. Appl. Phys.* 82 (1997) 3783.
- [20] M. Shwarz, A. Karma, K. Eckler, D. M. Herlach, *Phys. Rev. Lett.* 73 (1994) 1380.
- [21] S.C. Flood, J. D. Hunt, *ASM Metals Handbook, Casting* 15 (1990) 130.
- [22] M.A. Martorano, C. Beckerman, Ch.-A. Gandin, *Metall. Mater. Trans. A* 34A (2003) 1657.
- [23] Ch. Pequet, M. Gramaud, M. Rappaz, *Metall. Mater. Trans. A* 33A (2002) 2095.
- [24] T.L. Finn, M.G. Chu, W.D. Bennon, *Micro/Macro Scale Phenomena in Solidification*, C. Beckermann, ed., ASME, New York, NY, 1992, 17.
- [25] R.C. Dorward, D.J. Beersten, *Light Metals 1990*, C.M. Bickert, ed., TMS, Warrendale, PA, 1990, 919.
- [26] A.M. Glenn, S.P. Russo, P.J.K. Paterson, *Metall. Mater. Trans. A* 34A (2003) 1513.
- [27] D.G. Eskin, J. Zuidema, V.I. Savran, L. Katgerman, *Mater. Sci. Eng. A* 384 (2004) 232.
- [28] Suyitno, D.G. Eskin, V.I. Savran, L. Katgerman, *Metall. Mater. Trans. A* 35A (2004) 3551.
- [29] D.G. Eskin, V.I. Savran, L. Katgerman, *Metall. Mater. Trans. A* 36A (2005) 1965.
- [30] H. Yu, D.A. Granger, *Int. Conf. Aluminium Alloys – Their Physical and Mechanical Properties*, E.A. Starke Jr., T.H. Sanders Jr, eds., EMAS, Warley, U.K., 1986,17.
- [31] M.G. Chu, J.E. Jacoby, *Light Metals 1990*, C.M. Bickert, ed., TMS, Warrendale, PA, 1990, 925.
- [32] R. Nadella, D.G. Eskin, L. Katgerman, *Metall. Mater. Trans. A* 39A (2008) 450.

[33] D.G. Eskin, R. Nadella, L. Katgerman, *Acta Mater.* 56 (2008) 1358.

Chapter 2

Experimental Procedure

Chapter 2 presents the experimental procedures for sample preparation and experimental set-ups. The interrupted solidification (i.e. quenching) experiments for studying the microstructure development during unconstrained solidification conditions is demonstrated. Also, the in-situ solidification experiments are also shown for studying solidification during constrained growth (i.e. directional solidification experiments). Finally, the experimental procedure for studying dendrite coarsening, the formation of eutectics and duplex structures is described.

2.1. Introduction

2.1.1. Interrupted unconstrained solidification

Unconstrained growth involves the “free” development of dendrites. In this case, solidification conditions should allow nucleation and growth of dendrites from different places in a solidifying volume. This sort of dendritic development involves heat flow from the solid into the melt in addition to having heat transfer through the solid for releasing the latent heat during solidification. The microstructure evolves in a complex manner, having dendrite impingement and coalescence which will eventually result in a continuous solid network [1,2].

In order to study microstructure solidification under unconstrained conditions, the experimental technique has to allow for heat extraction from different directions and let the structure to develop freely during solidification. The technique which has been widely used to study microstructure development during solidification is quenching. This technique provokes the sample to “freeze” its structure during rapid solidification, as long as the heat extraction is large enough in order to produce an increase in cooling rate. By defining the structures both prior to quenching and after quenching by increasing the cooling rate, the structure that existed at the quenching temperature can be extracted.

Several experimental set-ups have been designed for studying the solidification of alloys at a laboratory scale by using the quenching. The samples, also, have to be very small to allow rapid increase in heat extraction during quenching. These techniques have failed before in providing adequate freezing of samples

to study the microstructure during the entire solidification range of aluminium alloys. Especially at high temperatures, overestimation of solid fraction has been identified as the main problem existing when quenching samples [3-7]. The observations about overestimation in solid are based on the solidification models i.e. the lever rule and the Gulliver-Scheil approximation which determine the extreme amounts of phases during solidification according to solute distribution [2] as described in Chapter 1.

Experiments have failed in providing quenched samples with the amount of phases falling within range predicted by the two solidification models in the entire solidification range. For example Nielsen and Olsen [4] tried to study the structure development of an Al-10 wt.% Cu alloy by translating and then dropping the samples in water. The time during translation and dropping could have been enough to allow some continuation of growth of the solid phase and/or to permit some coarsening. Also, continuous measurement of temperature changes prior and during quenching was not monitored in the sample but by considering temperature changes in a reference sample [4].

In the present chapter the description of the experimental set-up employed for the preparation of quenched samples is given. This set-up was designed in a way that quenching can be done more accurately in terms of controlling the freezing of a sample than the experimental techniques used before [3-7]. Temperature changes in the samples were monitored during the entire solidification and quenching stages. Moreover, vertical translation of the furnace, having the samples immobile, allowed fast quenching by moving the quenching medium from the bottom to the upper part where the sample was positioned.

2.1.2. Continuous constrained directional solidification

Directional growth of dendrites or constrained solidification permits one to study the microstructure development and to relate the solidification parameters with the evolving structure. In this case, heat flow is opposite to the growth direction. Dendrites develop towards one direction having their tips in contact with the undercooled liquid [2]. Also, this experimental procedure permits the relation of existing solidification models with experiments since much of the models widely described in literature were deduced assuming directionally solidification to simplify the solidification process [2].

In order to promote directional solidification, the molten sample has to be continuously translated from the liquidus temperature towards the solidus temperature. A Bridgman-type furnace is the experimental set-up which has been used over the years to promote these solidification conditions. This furnace can promote vertical or horizontal directional solidification depending on its configuration. Much of the work done for studying the microstructure development during solidification has been done using the Bridgman furnace along with quenching [1,2]. Much of these studies (in the case of opaque alloys) have been done assuming constant growth and no in-situ observation of the solidifying structure was performed.

In this Chapter, the description of the Bridgman-type furnace used in the present studies is given. This furnace was employed to promote directional solidification of aluminium alloys by having vertical sample translation parallel and anti-parallel to gravity. The experimental set-up along with the use of thin samples of high-solute aluminium alloys allowed the in-situ analysis of microstructure development by using X-ray microscopy. The sample

preparation and experiments were performed by Mathiesen et al. [8]. The present thesis employed the visual results of these experiments to study the microstructure development during constrained growth conditions. For the sake of completeness of the thesis the description of the experimental set-up and sample preparation is given here.

2.1.3. Experimental procedure for studying the microstructure development and its influence in the final structure

This chapter also describes the method utilized for studying dendrite coarsening and its influence on the formation of non-equilibrium eutectics. This experimental method corresponds to that developed for studying solidification during unconstrained solidification conditions (see Section 2.2) but employing a different approach which is shown here. For studying the influence of fragmentation on the formation of duplex structures, samples obtained from cast billets were used. These samples were obtained from billets produced by conventional hot-top DC casting. The billets were produced by utilizing the casting facility at the Delft University of Technology [9,10]. The samples correspond to those obtained by R. Nadella et al. [11]. The samples contain a structure conformed by fine-cell and coarse-cell grains (i.e. a duplex structure).

The materials and corresponding experimental studies are shown in this chapter. The following Chapters (i.e. Chapters 1,2 and 3) describe the methods used for analysing the resulting samples.

2.2. Interrupted Unconstrained Solidification

2.2.1. Materials and sample preparation

Binary hypoeutectic Al–3 wt.% Si and Al–7 wt.% Cu alloys were selected for unconstrained growth studies. These alloys were chosen from the Al–Si and Al–Cu phase diagrams considering the part of the diagrams where a large solidification range is located. The selection of alloys having a wide transition range was done in order to reproduce accurate quenching at selected temperatures within the solidification range of the respective alloy.

The equilibrium liquidus and eutectic temperatures for the Al–3 wt.% Si alloy are: $T_L = 642$ °C and $T_{eut} = 577$ °C respectively. For the Al–7 wt.% Cu alloy these temperatures are: $T_L = 642$ °C and $T_{eut} = 548$ °C. These temperatures were obtained from the *Thermocalc* software, TTA13 database, version 3.0.

The alloys were prepared from 99.999 wt.% Al, 99.999 wt.% Si, and Al–47.7 wt.% Cu commercially pure ingots. Table 2.1 demonstrates the chemical composition of the Al–3 wt.% Si and Al–7 wt.% Cu alloys which was obtained by using a spark spectrum analyzer *SpectroMax*. The alloys were cast as rods and cut as small cylindrical samples. The samples were drilled in the middle to permit the insertion of a thermocouple.

The small samples were placed inside Al₂O₃ and graphite crucibles in order to achieve two different quenching rates during the experiments. The dimensions of the Al₂O₃ and graphite crucibles were 32 mm-high × 25 mm-Ø and 15 mm-high × 14 mm-Ø, respectively. The final dimensions of the cast samples after

the quenching experiments were 30 mm-high \times 15 mm- \varnothing and 14 mm-high \times 11 mm- \varnothing when using Al₂O₃ crucibles and graphite crucibles, respectively. Thin-walled graphite crucibles (0.25 mm thick) 15 mm-high \times 14 mm- \varnothing were utilized for most of the experiments.

Table 2.1. Chemical composition for the Al-3 wt.% Si and Al-7 wt% Cu alloys.

Al-3 wt.% Si						
Element	wt.% Si	wt.% Fe	Wt.%Cu	Wt.% Mg	wt.% Ti	wt.% Al
Average	3.21	0.033	0.003	0.001	<0.001	96.73
\pm (wt.%)	0.07	0.001	0.000	0.001	0.000	0.088
Al-7 wt.% Cu						
Element	wt.% Si	wt.% Fe	wt.%Cu	wt.% Mg	wt.% Ti	wt.% Al
Average	0.035	0.063	7.15	0.000	<0.001	92.71
\pm (wt.%)	0.000	0.002	0.16	0.000	0.000	0.167

2.2.2. Experimental set-up

Figure 2.1 illustrates the experimental set-up. The sample was placed inside a holder which permitted to place it steadily and to reproduce fast quenching in the later stage of the experiment. Once the sample was placed in the holder, the furnace was positioned down for heating. The sample was heated until a temperature of ~ 700 °C was achieved. Then, the sample was carefully stirred for ~ 3 s by tapping the crucible at the surface walls with a thin alumina tube. After the sample had been stirred, the furnace was placed down again for heating until the temperature of ~ 700 °C was reached again. Once achieving this temperature, the furnace was turned off and continuous slow cooling was promoted over the samples. A cooling rate of $dT/dt \sim 0.2\text{--}0.5$ K/s ± 0.15 was obtained from Eq. 2.1 by measuring reference samples that solidified completely. Prior to the estimation of the cooling rates of the studied samples,

several experiments were performed in order to determine the right experimental and cooling rate analysis procedures and thus enabling reproducibility of results.

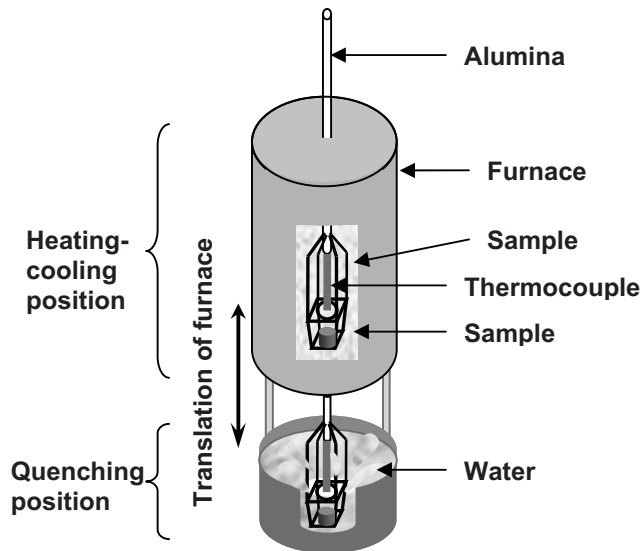


Figure 2.1. Schematic representation of the experimental set-up which permitted solidification and quenching.

Water quenching was used in order to “freeze” the microstructure at different temperatures during solidification. The temperatures $T = 635, 630, 620, 595, 585$ and $550 \text{ }^\circ\text{C}$ ($\pm 2 \text{ }^\circ\text{C}$) within the solidification transition region for the Al–7 wt.% Cu alloy were selected. And for the Al–3 wt.% Si alloy, the selected temperatures were: $T = 635, 625, 615, 595, 580$ and $575 \text{ }^\circ\text{C}$ ($\pm 2 \text{ }^\circ\text{C}$). When reaching a selected temperature, the furnace was translated upwards and the sample was immediately immersed in water. The thermocouple was kept inside of the sample and the quenching rate dT_q/dt was determined from the recorded cooling curves as $\sim 50 \text{ K/s}$ when cooling inside the Al_2O_3 crucibles and $\sim 100 \text{ K/s}$ when cooling inside the thin-walled graphite crucibles (estimated from Eq.

2.2). The experimental set-up allowed quenching at relatively high temperatures with no drastic changes in the sample shape, as compared to other experimental set-up that had exploded samples when quenching at high temperatures [7]. Figure 2.2 demonstrates, as an example, a cooling curve of an Al-7 wt.% Cu sample quenched at 550 °C. It can be seen the slopes when solidification started (region A) and when quenching was promoted (region B).

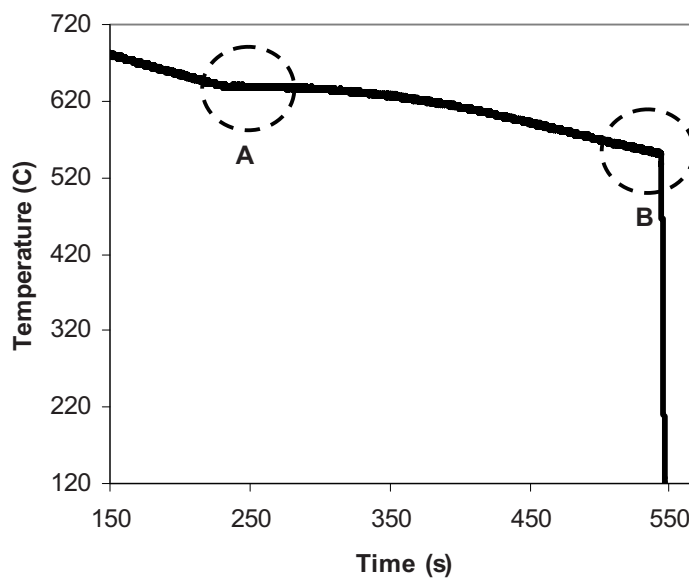


Figure 2.2. Cooling curve of an Al-7 wt.% Cu sample quenched at 550 °C. Region A shows the slope when solidification started and region B shows when quenched was promoted.

The cooling and quenching rates were estimated from the cooling curves as follows:

$$dT / dt = \dot{T} = \frac{T_L - T_{eut}}{t_L - t_{eut}}, \quad (2.1)$$

$$dT_q / dt = \dot{Q} = \frac{T_q - T_{500}}{t_q - t_{500}}, \quad (2.2)$$

where \dot{T} is the cooling rate, T_L is the temperature of liquidus, T_{eut} is the eutectic temperature, t_L is the time at which T_L was reached and t_{eut} is the time at which T_{eut} was reached in Eq. 2.1. \dot{Q} is the quenching rate, T_q is the temperature of quenching, T_{500} is a temperature below the eutectic reaction, t_q is the time at which T_q was reached and t_{500} is the time at which T_{500} was reached in Eq. 2.2.

The liquidus T_L and eutectic T_{eut} temperatures were estimated from the cooling curves by detecting slope changes during cooling which correspond to the start of solidification and eutectic reaction respectively (Table 2.2). It can be seen that the temperatures are quite similar, differing for about ± 5 °C comparing the conditions when quenching at 50 K/s and 100 K/s (i.e. cooling in the alumina crucibles and graphite crucibles, respectively).

Finally, the samples were transversally cut, ground and polished. For grinding and polishing, a *RotoPol-31* and a *LaboPol-21* apparatus from *Struers* were used respectively.

Table 2.2. Measured eutectic temperatures from cooling curves (error $\pm 2^\circ$).

Al-3 wt% Si			Al-7 wt.% Cu		
dT_q/dt	50 K/s	100 K/s	dT_q/dt	50 K/s	100 K/s
T_q (°C)	T_{eut}	T_{eut}	T_q (°C)	T_{eut}	T_{eut}
634	570	566	637	540	537
627	572	566	631	541	537
616	570	566	620	540	540
595	572	566	595	540	540
582	577	565	583	540	540
578	582	566	551	541	540

2.3. Continuous Constrained Directional Solidification

2.3.1. Materials and sample preparation

Sample preparation, directional solidification experiments and image acquisition demonstrated here were performed by Mathiesen et al. in refs [8,12,13]. The present thesis employed the images for further image processing and analysis of microstructure phenomena i.e. coarsening and dendrite fragmentation.

Binary Al–30 wt.% Cu and Al–20 wt.% Cu alloys were selected for the directional solidification studies. The high-solute content alloys chosen for these studies, together with the coherency characteristics of the synchrotron beam, provided enough contrast at the solid–liquid interface to identify solid regions even for dendrite branches down to a thickness of 3–4 μm [8].

The equilibrium liquidus and solidus temperatures for the Al–20 wt.% Cu alloy are: $T_L = 603$ °C and $T_{eut} = 548$ °C respectively. For the Al–30 wt.% Cu alloy the temperatures are: $T_L = 563$ °C and $T_{eut} = 548$ °C. These temperatures were using the Al–Cu phase diagram obtained from *Thermocalc* software.

The alloys were prepared from aluminium and copper having both 99.999 wt.% purity. Alumina crucibles were utilized to contain the samples during melting. The samples were prepared as rectangular slices of the alloy, 1.5×3.0 cm² in area and 200 μm thick, and sealed between 100 μm thick quartz glass plates after being pre-oxidized at 720 K for 2 h and spray-coated with boron nitride.

Then, the samples were directionally solidified in an insulating mould which promoted these conditions by having a chill at the bottom. Directionally solidified samples should provide a homogeneous structure avoiding porosity and macrosegregation [8,12,13].

2.3.2. Experimental set-up

A Bridgman-type furnace facilitated directional solidification and control of the solidification conditions. This furnace can operate at temperatures up to 1200 K for small samples (with the dimensions mentioned above). Figure 2.3 illustrates the experimental set-up. High-brilliance synchrotron X-radiation microscopy along with the furnace configuration allowed in-situ microstructure observation during solidification. The set-up consisted of two furnaces that allowed directional solidification and between them an aperture allowed the X-rays to penetrate the sample (Fig. 2.3).

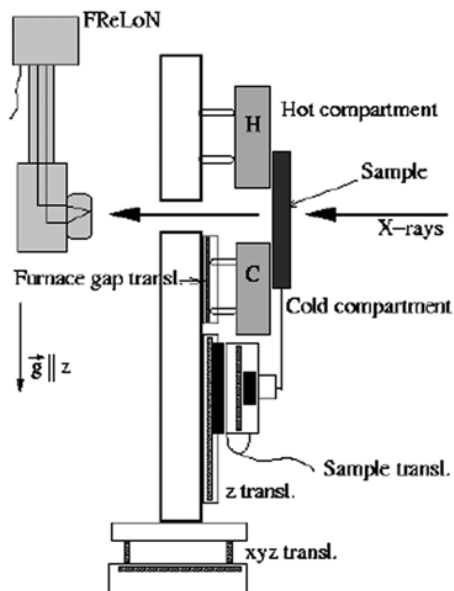


Figure 2.3. Bridgman-type furnace and X-ray Microscopy (after Mathiesen et al. [8]).

The experiments were performed at beamline ID22 at the European Synchrotron Radiation Facility (ESRF) in Grenoble, France. These were done under experiment codes: HS-1332 and E-595 for the Al–30 and 20 wt.% Cu alloys experiments, respectively.

An incident monochromatic X-ray energy of 15 KeV was employed, yielding a flux density at the sample of $\sim 10^{12}$ photons $\text{mm}^{-2}\text{s}^{-1}$. A detector dead time of 0.15 s, together with an exposure time of 0.3 s gave a frame-grabbing rate of 2.22 s^{-1} (i.e. images were obtained every 0.45 s). The full image field of view corresponded to $1.35 \times 1.35 \text{ mm}^2$. Transverse beam coherency lengths were about $l_z \sim 50 \text{ }\mu\text{m}$ vertically and $l_y \leq 5 \text{ }\mu\text{m}$ horizontally. Image acquisition was facilitated by using a Fast Readout Low Noise (FReLoN II) high-resolution X-ray microscope. A distance between the sample and detector was set as 55 cm. Specific details and relevant information about the experimental set up and X-ray microscopy are given elsewhere [8].

The temperature gradient within the gap, where the sample is located, can be changed depending on the temperatures of the furnaces. These temperatures can be varied within 850 to 990 K in the heating section and 700 to 840 K in the cooling section. The spacing between the furnaces can be changed within 2 to 9 mm of aperture.

The Al–30 wt% Cu and the Al–20 wt% Cu alloys were solidified downwards and upwards, respectively. To promote downward growth (solidification parallel to gravity), the sample was first kept in the liquid state in the hot section of the furnace for a short period of time. The sample was then translated upwards from the hot section towards the cold section of the furnace. The sample was translated with a constant velocity $v_{sp} = -22.5 \text{ }\mu\text{m/s}$. In this experiment the thermal gradient was $G_T = 27 \text{ K/mm}$. In the case of upward

dendrite growth opposite to gravity, the sample was moved downwards from the hot section towards the cold section of the furnace ($v_{sp} = 25 \mu\text{m/s}$). The hot section was located on the top of the furnace in contrast to downward solidification, where the hot section was located at the bottom of the furnace. During upward growth, $G_T = 48 \text{ K/mm}$.

Two series of images were selected from the experiments [8]. The quality of the images (i.e. brightness and contrast) permitted an accurate quantitative analysis. Also, these series of images demonstrated well developed columnar dendrites showing clearly the solidification and eutectic fronts. This is required in order to determine the solidification parameters (e.g. local solidification time) according to solidification theory. It was not possible to compare the solidification process during upward and downward growth with series of images having the same composition and solidification conditions. The actual solidification of the samples was different from experiment to experiment along with the quality of the images.

The acquired images during the solidification experiments were further processed and analyzed. This is described in Chapter 4.

2.4. Experimental Procedure for Studying the Microstructure Development and its Influence on the Final Structure

2.4.1. Experimental procedure for studying the formation of non-equilibrium eutectics

2.4.1.1. Materials and sample preparation

The chemical compositions of the binary Al–Cu alloys used for the experiments are shown in Table 2.3. The alloys were prepared from 99.9 wt.% Al and Al–48 wt.% Cu master alloy. The alloys were non-grain refined and no further metal treatment was done to the melt. The impurities, according to the chemical analysis, were less than 0.1 %.

Table 2.3. Alloy samples demonstrating the estimated cooling rates (see Fig. 2.4).

Alloy	1	2	3	4	5	6
Cu, wt.%	0.98	2.12	3.24	4.3	1.83	1.86
Range of total cooling rate, K/s	0.3–13.5	0.2–10	0.2–12.5	0.2–9	0.15–16	0.15–23
Range of linear cooling rate, K/s	0.4–12	0.3–10.5	0.3–13	0.3–12	–	–

The samples were prepared under different conditions as follows:

1) The melt was heated up to 725 °C and then poured in different moulds of different materials (i.e. materials having different thermal conductivity) and volumes (in the range of 160 to 10 cm³) which were exposed to different cooling conditions (i.e. by heating the mould or cooling with water). During solidification the cooling curves were continuously recorded by using a thermocouple. The cooling curves allowed to determine two cooling rates defined here as “total” and “linear” (Fig. 2.4).

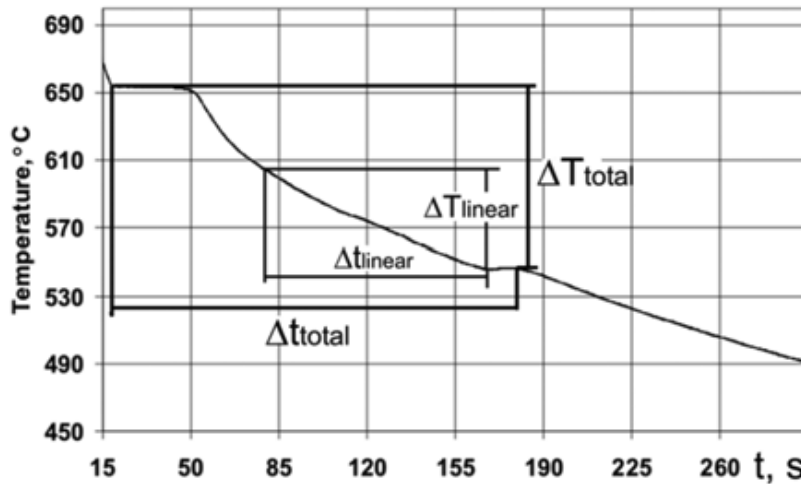


Figure 2.4. Cooling curve showing the local regions in the curve employed for determining both: the “total” $V_C = \Delta T_{total} / \Delta t_{total}$ and “linear” $V_C = \Delta T_{linear} / \Delta t_{linear}$ cooling rates.

The total cooling rate was determined as the total solidification temperature range divided by the total solidification time (Fig. 2.4). This method of determining the cooling rate may not reflect the actual heat extraction rate by the mould since the effect of latent heat evolution may overshadow the results. This is why the following method was also used for determining the cooling rate and comparing results. The linear cooling rate was estimated from the same cooling curve by considering the lower linear part of the curve (Fig. 2.4), also

dividing the respective solidification temperature range by the solidification time in that part of the curve. For this set of experiments different alloys were utilized (alloys 1–4 in Table 2.3).

2) The other set of experiments corresponds to the analysis of Al–1.83 wt.% Cu alloy samples (alloy 5 in Table 2.3). The samples were melted inside a cylindrical vertical furnace in alumina crucibles having $\sim 4 \text{ cm}^3$ of internal volume. During heating and cooling of the sample, the cooling curve was continuously recorded by having a thermocouple inside the sample. In this set of experiments, the samples were first melted at a temperature of 710 °C and then cooled down to room temperature under the following conditions: inside of the furnace, outside of the furnace, with still air, with forced air, in oil and in water. Then, the cooling rates were determined from the cooling curves.

3) The last set of experiments corresponds to samples prepared from Al–1.86 wt.% Cu (alloy 6 in Table 2.3). Cooling conditions were similar to those in 2), however, in this case, the samples were quenched at 544 °C for a cooling rate of 0.15 K/s, at 541 °C for 0.35 K/s and at 536 °C for 0.8 K/s. The samples cooled in water were not further quenched.

2.4.2. Experimental procedure for analyzing the influence of fragmentation on the formation of duplex grain structures

2.4.2.1. Materials and sample preparation

A cast 7075 billet alloy with the composition: 5.68 Zn, 1.32 Mg, 0.29 Cr, 0.10 Fe and 0.007 Si (wt.%) was used for studying the formation of duplex

structures. The round billet 192 mm in diameter was cast in a DC casting facility at the Delft University of Technology. A hot-top mould configuration was used for casting with a level-pour metal delivery system. A more detailed description about the DC casting experimental set-up can be found elsewhere [9, 10]. The casting speed was 80 mm/min during steady state having a water flow rate of 170 l/min. The melt temperature was 715 °C.

An amount of 0.005% Ti, from an Al–3% Ti–1% B master alloy, was added to the alloy prior to casting as a grain refiner. The billet was stress-relieved after casting at 400 °C for 4 hours in an electrical furnace with air circulation. A more detailed description about the characteristics of the cast such as structure and chemical composition variation along the billet diameter can be found in ref. [11]. The samples analyzed were taken from the centre of the billet (i.e. intersection between the billet vertical axis and the billet diameter). The size of the samples was 20 × 20 mm in cross-section.

The analysis procedure of the samples obtained here is presented in the respective Chapters.

References

- [1] M.C. Flemings, Solidification Processing, McGraw-Hill, New York, 1974.
- [2] W. Kurz, D.J. Fisher, Fundamentals of Solidification, 3rd ed. Trans. Tech. Publications, Aedermannsdorf, Switzerland, 1992.
- [3] M. Rettenmayr, O. Pompe, J. Cryst. Growth 173 (1997) 182.
- [4] Ø. Nielsen, S.O. Olsen, Transactions of the American Foundryman's Society 110 (2002) paper 02-096.
- [5] O. Pompe, M. Rettemayr, J. Cryst. Growth 192 (1998) 300.
- [6] E. Tzimas, A. Zavaliangos, J. Mater. Sci. 35 (2000) 5319.
- [7] S.W. Chen, C.C. Huang, Acta Metall. 44 (1996) 1955.
- [8] R.H. Mathiesen, L. Arnberg, K. Ramsøskar, T. Weitkamp, C. Rau and A. Snigirev, Metall. Mater. Trans. B 33B (2002) 613.
- [9] D.G. Eskin, J. Zuidema, V.I. Savran, L. Katgerman, Mater. Sci. Eng. A 384A (2004) 232.
- [10] D.G. Eskin, V.I. Savran, L. Katgerman, Metall. Mater. Trans. A 36A (2005) 1965.
- [11] R. Nadella, D.G. Eskin, L. Katgerman, Mater. Sci. Technol. 23 (2007) 1327.
- [12] R.H. Mathiesen, L. Arnberg, Adv. X-Ray Anal. 49 (2006) 37.
- [13] R.H. Mathiesen, L. Arnberg, P. Bleuet and A. Somogyi, Metall. Mater. Trans. A 37A (2006) 2515.

Chapter 3

Microstructure Development during Unconstrained Solidification Conditions¹

Chapter 3 contains studies on microstructure development during unconstrained solidification conditions. The quenching technique described in Chapter 2 allowed studying the structure evolving during solidification from 2D images at temperatures close to the eutectic reaction of the aluminium alloys. Also, by identifying features that represent coalescence of instabilities from 3D reconstructed microstructures, overestimation of solid fraction when quenching at high temperatures can be reduced. Thus, based on these observations and on microsegregation measurements, the solidification path during solidification can be suggested.

¹ Chapter 3 is based on publications: 1–3, 6, 8, 9 (see publications on pages 199, 200).

3.1. Introduction

During unconstrained solidification conditions solutal and thermal gradients build up within the solidifying volume. Under these conditions, dendrites (the solid phase) nucleate and grow up from different regions. Unconstrained dendritic growth is a more representative solidification condition to real-industrial castings than unidirectional or constrained solidification. During casting, according to casting dimensions, casting shape and heat flow, solidification implies development of dendrites which may interact with each other (dendrite impingement). Also, the microstructure develops in a complex manner influencing the evolution from slurry to mushy state within the transition region. Under, these conditions the solid phase develops in a more complex way and a well developed columnar dendritic structure may no longer prevail during solidification. [1-4]. Thus, it is vital to understand microstructure development under unconstrained growth conditions.

Much of the research in microstructure development during solidification is based on experimental studies where constrained solidification is imposed on the solidifying sample. This condition is achieved by using a Bridgman-type furnace where directional growth occurs via translating of a molten sample from the hot section into the cold section. This enables growth of dendrites in a single direction and facilitates the analysis of the structure with relation to solidification theories. However, as mentioned before, this sort of solidification has limited applicability or relation to real-cast solidification conditions.

It is also important to understand how the microstructure develops during unconstrained solidification conditions, since the formation of cast defects is

influenced by the permeability that depends on solid fraction evolution as described in Chapter 1.

The quenching technique has been widely used to study the solidification of alloys and provides observation of the microstructure. Thus, the solid fraction f_S and secondary dendrite arm spacing SDAS or surface-to-volume ratio S_V may be obtained by image analysis of the quenched samples. This technique gives reasonable result when quenching close to the eutectic reaction or when studying coarsening during isothermal holding and quenching [5-9]. One disadvantage of this technique is that in-situ observation of the microstructure is not possible to perform. Other disadvantage is that quenching at high temperatures does not provide reliable results, giving an overestimation of solid fraction. It has been shown, that even when carefully processing 2D images from cross-sections and not considering the fine instabilities developing during quenching as the solid developing prior to quenching, the solid fraction is still overestimated compared to the two solidification extremes (lever rule and Gulliver–Scheil model) [5-9]. However, not many studies have analysed the reasons for overestimation of solid fraction and further analysis of it has not been presented.

Moreover, much of the analysis of microstructure development has been done by studying 2D cross-sections of samples. As mentioned before, unconstrained solidification conditions involve 3D evolution of the entire structure, thus, analysis of such structures in 2D may lead to errors during the morphological interpretation of evolving phases. Therefore, 3D microstructure analysis is required to compensate for such 2D stereological errors.

The present chapter starts with the microstructure development evaluated from 2D metallographic images; this encompasses solid fraction and

microsegregation. Then, the overestimation of solid fraction from 2D images is analyzed. 3D reconstruction of quenched samples by using the serial sectioning technique is furthermore employed in order to reveal the true 3D morphology of phases. 3D reconstruction reveals that part of the overestimation problem is related to coalescence of instabilities developing during quenching. This analysis enabled us to reduce overestimation of solid fraction at different temperatures. In addition, the microstructure development during unconstrained solidification conditions is described based on the 2D and 3D structure analysis.

3.2. Procedure for Data Analysis

The procedure for the sample preparation, solidification and quenching at selected temperatures within the transition region has been described before (Chapter 2). Al-3 wt.% Si alloy and Al-7 wt.% Cu alloy quenched samples were used here to estimate the solid fraction and microsegregation within the solid phase. 3D reconstruction and analysis of microstructures were done for the Al-7 wt.% Cu alloy and are also presented here.

3.2.1. Solid fraction

The solid fraction was estimated from a series of images from the cross-section of the samples. A *Leica DMLM* Optical Microscope was utilized in order to observe and obtain the images. The images were taken close to the thermocouple tip which recorded the temperature during continuous cooling and quenching. The selection of phases (solid and liquid prior to quenching) was done by considering finer dendrites (i.e. instabilities), and quenched eutectic as the former liquid phase and coarse dendrites as the solid developing

prior to quenching (during continuous solidification). The consideration of instabilities or finer dendrites as part of the liquid prior to quenching is based on the assumption that, at the moment of quenching, the remaining liquid to solidify develops as finer dendrites due to the increased cooling rate. The solid phase prior to quenching can be preserved and distinguished as long as the heat extraction during quenching is adequate enough to produce differences in cooling rate.

In order to perform the separation of phases, the *AnalySIS* software for image processing and analysis was employed. The image was first filtered by using an open filter followed by erosion. Then a threshold is applied to make the separation of phases (Fig. 3.1). Black colour represents the solid phase prior to quenching, while the white colour represents the liquid existing prior to quenching. As it is shown in Fig. 3.1, the processed images are not good enough for separation of phases. The existence of finer features, which should not be present, is still visible from the processed images. The measurements would be wrong if the features would be considered as part of the solid prior to quenching (black features), giving the overestimation. Therefore, the images can be better processed by manually delineating the boundaries of the solid phase without considering finer features and quenched liquid. The procedure was done by considering several images at high magnifications. The solid fraction was estimated by measuring the occupied area of the solid phase divided by total area of the image. This quantitative analysis was done automatically by using also *AnalySIS* software.

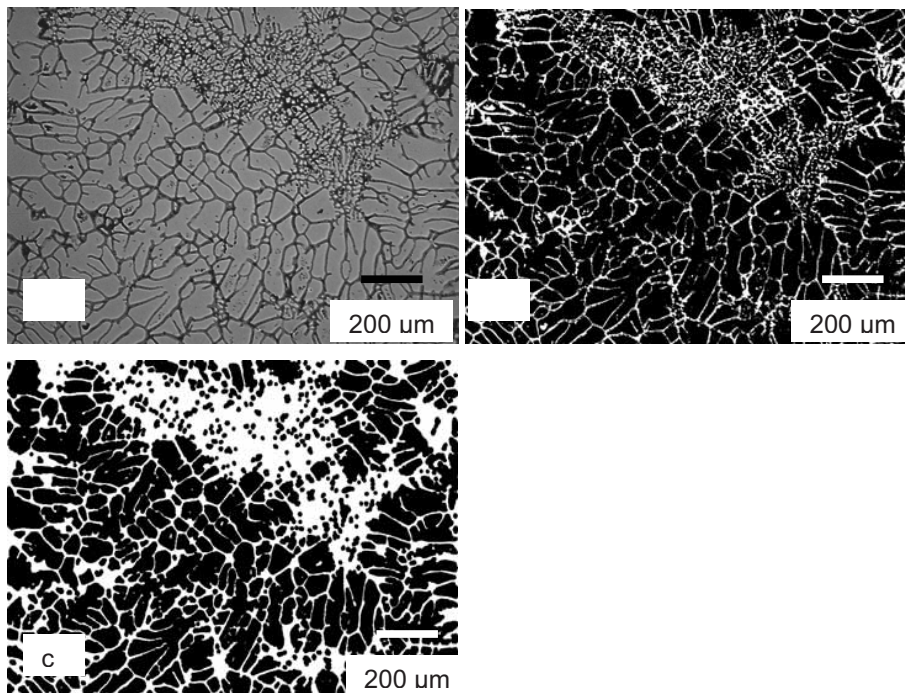


Figure 3.1. Al-7 wt.% Cu alloy sample quenched at a temperature of 631 °C; (a) original image, (b) image showing the solid phase in black and the liquid phase in white, and (c) filtered image showing the instabilities + liquid that represent the liquid prior to quenching as a white phase and the solid as a black phase.

Thermocalc software was used to determine the solidification path (solid fraction as a function of temperature) of the studied alloy using both Gulliver–Scheil model and lever rule. The measured solid fraction f_S was then compared to the calculated solid fraction, i.e. f_{S_l} from lever rule and f_{S_s} from Gulliver–Scheil approximation.

3.2.2. Microsegregation

Microsegregation measurements were performed over the coarse solid phase developing prior to quenching and over the instabilities evolving during quenching. Also, some measurements over the quenched liquid are presented,

although these measurements may not be as accurate as those for the solid phase, due to destabilization of the composition in the liquid during quenching.

In order to obtain solute content in the microstructure, Scanning Electron Microscopy (SEM) and Electron Probe Micro Analysis (EPMA) were employed. Prior to the analysis, the samples were cleaned ultrasonically. This was done in acetone followed by isopropanol.

The SEM was used to visualize the samples and to perform local chemical analysis in selected regions. Microsegregation profiles along dendrite arms and finer instabilities were obtained by EPMA. This equipment consisted of a JEOL JXA 8900R microprobe using an electron beam with energy of 15 KeV and a current of 200 nA. The concentration of solute elements in the alloys was obtained, i.e. Si and Cu. The detection limits of the measured X-ray line are demonstrated in Table 3.1. The distance between the measuring points was between 0.5 and 2 μm .

Table 3.1. Detection limits of the X-ray lines.

Element	X-ray Line (Energy keV)	Detection Limit (ppm)
Al	K α (1.487)	12
Si	K α (1.740)	14
Fe	K α (6.403)	33
Cu	K α (8.047)	130

3.2.3. Serial sectioning

Images for serial stacking and 3D rendering were obtained by serial sectioning. Representative areas within the microstructure were selected for the

reconstruction. The areas were marked with a microhardness indenter in order to identify the regions to be reconstructed and to measure the polishing depth at each polishing step (Fig.3.2a). Then a series of images were obtained and stacked successively according to the section thickness (Fig. 3.2b).

The quenched samples were mounted in an Epoxy hot mounting resin with mineral filler in a *Predopress* apparatus from *Struers*. Successive grinding and polishing was done on the cross-section of the samples using an automatic grinding-polishing machine *Roto Pol-31* from *Struers*. The machine allowed reproducing approximately the same depth. Accordingly, the depth between sections was varied between ~ 0.5 and $\sim 2 \mu\text{m} \pm 0.5 \mu\text{m}$. This depth allowed the reconstruction of features for an appropriate mesh rendering and 3D surface reconstruction according to the length scale of the structure.

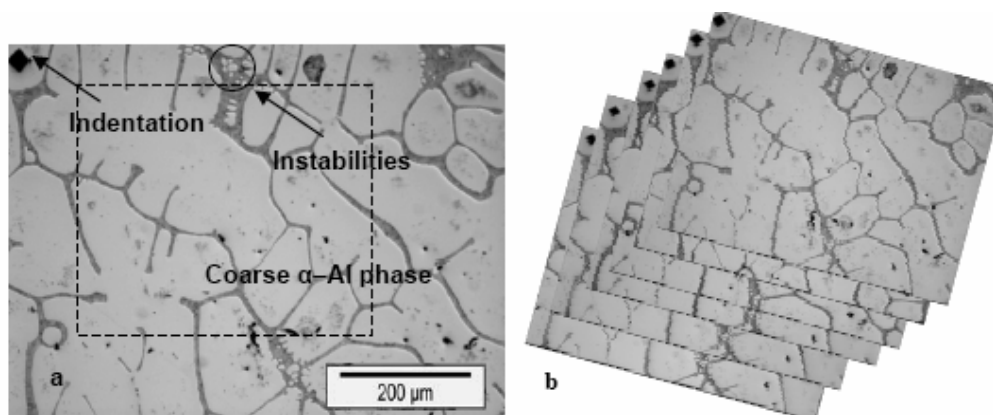


Figure 3.2. (a) 2D cross-section demonstrating the different microstructural features and indentation mark, and (b) image section stacking.

3.2.4. 3D microstructure reconstruction

Reconstruct software [10] facilitated section alignment and was subsequently used to select features, to render 3D meshes, and to visualize a 3D model.

Representative samples were selected for the reconstructions. First, the samples cross-sections were aligned using the indentation marks and coarse features within the solid dendrites that do not change much from one section to another (e.g. junction points). *Reconstruct* contains a function that permits alignment of images by fitting in the z direction selected points within the images. After alignment the field of view was reduced due to image displacement and image fitting. Figure 3.3 demonstrates a series of images which were aligned.

Second, the solid phase was selected by manually tracing lines around it (Fig. 3.3). By alternating between sections, finer and coalesced features, that represented the liquid prior to quenching and that solidified during quenching, were identified and not considered during tracing for the reconstruction.

And third, 3D rendering was produced from the traces that delimit the solid phase (dendrites) (Fig. 3.4). A Boissonnat surface algorithm within the *Reconstruct* software allowed mesh reconstruction for further 3D image visualization [10]. 360 ° rotation and image displacement can be done during visualization in *Reconstruct*. The different features within the reconstructed structure can also be distinguished by using different colours. In order to appreciate the 3D structure configuration, it is recommended to visualize the images by using different colours and sometimes by using different degrees of transparency between the objects.

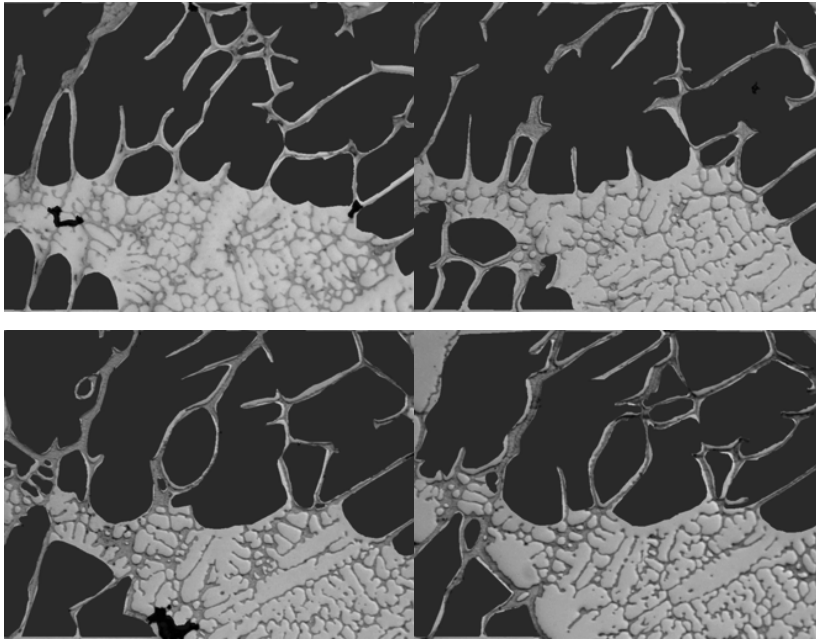


Figure 3.3. Series of images aligned using coarse features and indentation marks within the structures as fitting points. Also, the solid phase selection is demonstrated in dark-grey colour.

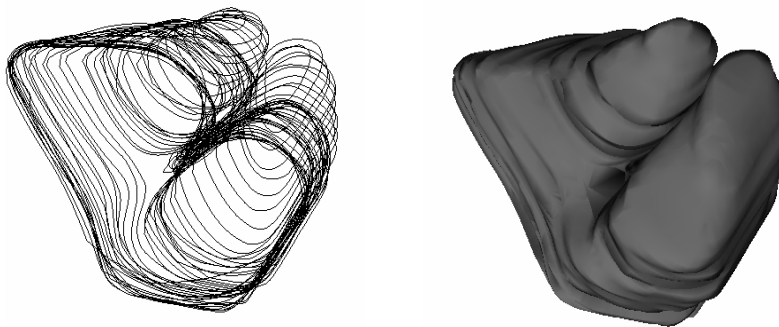


Figure 3.4. Serial tracing of boundaries and 3D mesh generation by using the Boissonnat surface algorithm.

3.2.5. 3D visualization and analysis

The dimensions of the reconstructed 3D volumes were $x = 318$, $y = 420$ and $z = 155$ μm . 3D visualization and quantitative analysis was done using *Reconstruct*. The solid volume fraction f_{sv} was estimated from:

$$f_{sv} = \frac{V_S}{V_T}, \quad (3.1)$$

where V_S is the volume occupied by the solid phase and V_T is the total volume.

The total volume $V_T = x \times y \times z \sim 21 \times 10^6$ μm^3 and V_S is estimated from the Cavalieri equation [10]:

$$V_S = \sum_{\text{Sections}} \text{area} \times \text{thickness}, \quad (3.2)$$

where the *area* corresponds to that occupied by the solid phase multiplied by the section *thickness*.

In order to estimate morphology evolution of the solid phase, the specific surface or surface-to-volume ratio was determined. This is an estimate of the total curvature of the interface dS/dV . This parameter is of great importance as being the driving force in determining microstructure development since it influences the internal energy of the system [11].

The surface-to-volume ratio S_V from the 3D reconstructed solid phase was determined from:

$$S_V = \frac{A_S}{V}, \quad (3.3)$$

where A_S is the surface area of the 3D reconstructed solid phase and V is the internal volume of the solid phase. The surface area and internal volume were determined from the *Reconstruct* software [10]:

$$A_S = \sum_{all\ sections} L \times thickness, \quad (3.4)$$

where L is the length of the trace that delimits the solid boundaries and *thickness* is the section thickness. The internal volume V was determined from:

$$V = \sum_{all\ sections} A_i \times thickness, \quad (3.5)$$

where A_i is the internal area of the delimited solid and *thickness* is the section thickness.

3.3. Solid Phase Development and Overestimation of Solid Fraction

3.3.1. Solidification path and overestimation of solid fraction

As mentioned earlier the solid fraction was determined for both: Al–3 wt.% Si and Al–7 wt.% Cu alloys during solidification. The estimated cooling rates were quite low ~ 0.2 and 0.5 K/s (± 0.15), and the quenching rates were ~ 50 K/s and 100 K/s for the solidification in Al_2O_3 crucible and for the thin-walled graphite crucible, respectively. The results are differentiated according to the quenching rate.

3.3.1.1. Solidification of an Al–3 wt.% Si alloy

Figure 3.5 demonstrates the typical microstructures quenched during the solidification of the Al–3 wt.% Si alloy. It is clear that instabilities in the quenched liquid are more pronounced when interrupting solidification at higher temperatures i.e. at $f_S < 0.4$. As solidification proceeds, instabilities become less evident. The separation between phases after quenching is due to an increase in cooling rate which refines the portion remaining to solidify. As demonstrated in Fig. 3.5, some instabilities were present in the liquid pools and at the boundaries of the coarse dendritic solid phase. During quenching, instabilities form at the boundaries of the solid phase which was already solid prior to quenching, and then they are displaced away from this interface due to the sudden increase in the solidification rate.

Figures 3.5 and 3.6 demonstrate the quenched structures observed for the Al–3 wt.% Si alloy when quenching at ~ 50 K/s and ~ 100 K/s respectively. Difference in the extent of solid phase was observed when quenching at different rates. Also, a more uniform microstructure in the entire examined area was observed in samples quenched at a higher rate.

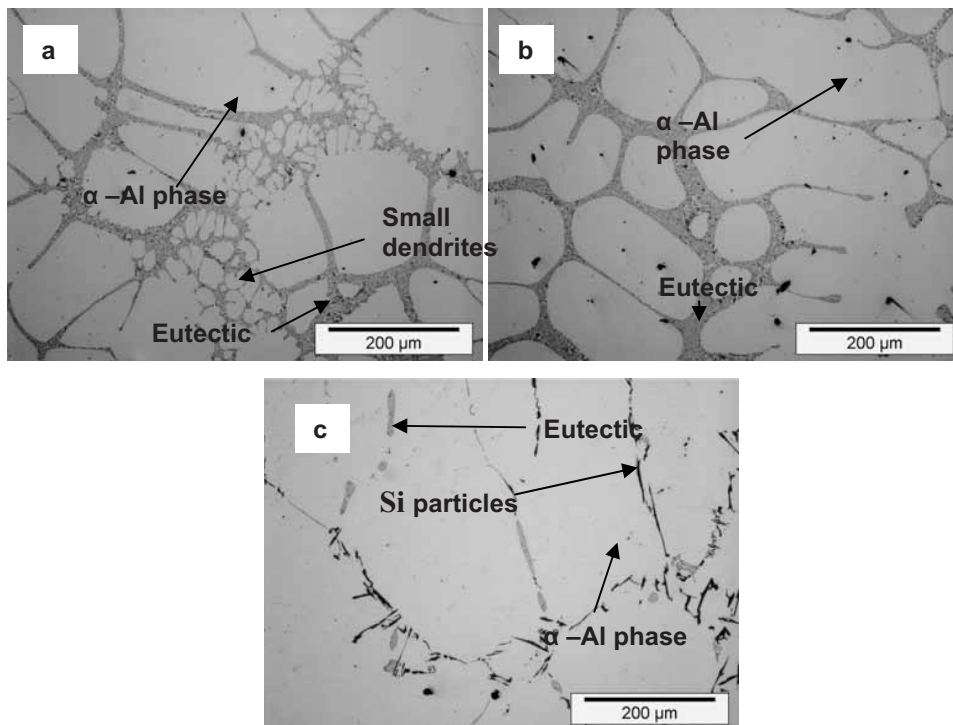


Figure 3.5. Al–3 wt.% Si alloy samples quenched at ~ 50 K/sec showing the quenched structures at: (a) 634°C, (b) 595 °C and (c) 578 °C.

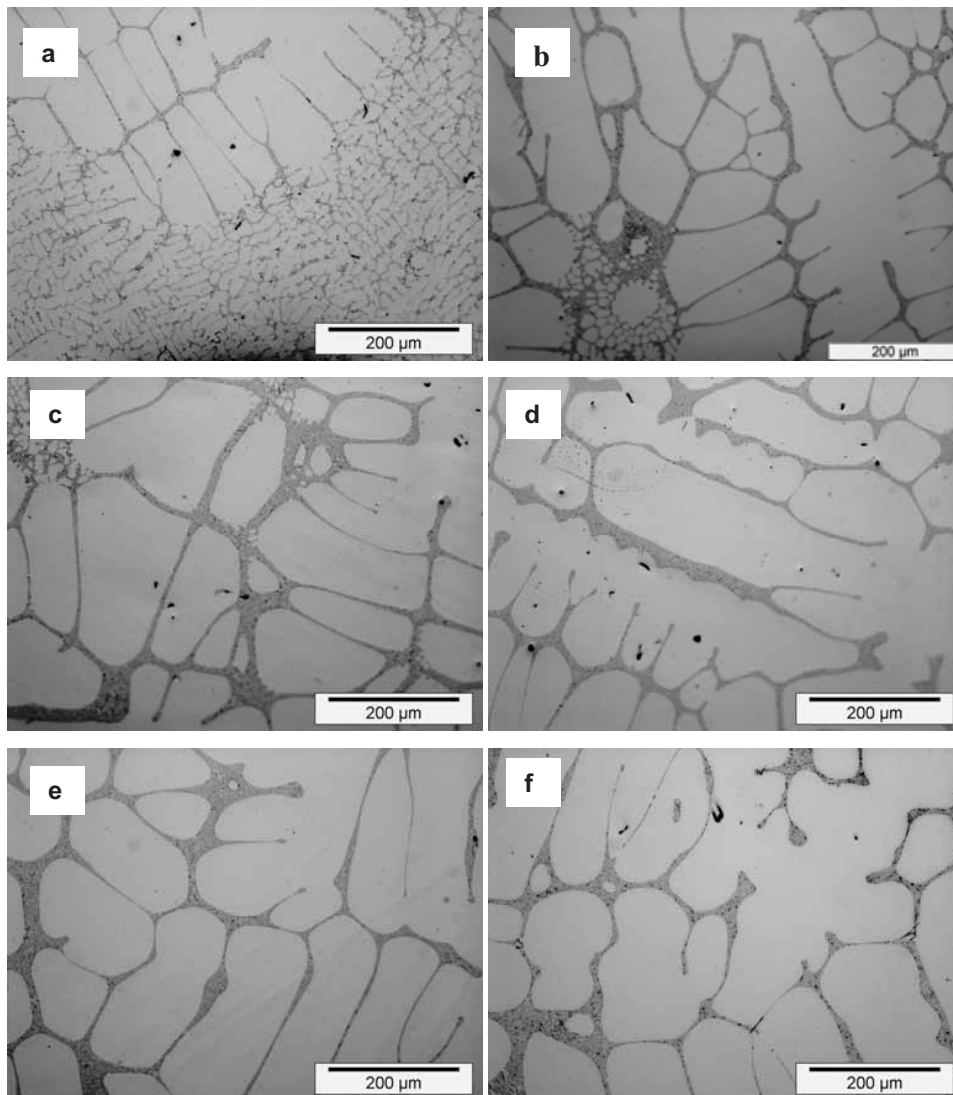


Figure 3.6. Al-3 wt.% Si alloy samples quenched at ~ 100 K/sec showing the quenched structures at: (a) 634 °C, (b) 627 °C, (c) 616 °C, (d) 595 °C, (e) 582 °C and (f) 578 °C.

The samples quenched close to the eutectic reactions, i.e. at 578 °C, exhibited clearly the effect of cooling rate and quenching rate on microstructure evolution. The samples which solidified in the alumina crucible with a quenching rate of $dT_q/dt = 50$ K/s, demonstrated two morphologies of binary Al-Si eutectics, i.e. needle-like Si particles from divorced slowly solidified

eutectic and from quenched eutectic (Fig. 3.5c). On the other hand, the samples solidified inside thin-walled graphite crucibles, i.e. $dT_q/dt= 100$ K/s, did not show needle-like Si particles but a finer distribution of particles (Fig. 3.6f).

The solidification path for the Al–3 wt.% Si alloy was calculated considering two databases from *Thermocalc* software. The TTA13 database and the SBIN2 database were employed. The TTA13 database considers the Si solubility limit in the solid to be ~1.56 wt.% Si (according to the Al–Si phase diagram). This solubility limit changes the slope of the solidus line (i.e. solute partition) affecting solute distribution in the solid. According to this, the TTA13 database estimates an initial solute content in the solid, which is ~0.33 wt.% Si at $T_L= 642$ °C. On the other hand, the SBIN2 database establishes the Si solubility limit in the solid to be ~ 2.4 wt.% Si which is 0.84 wt.% Si higher than the one determined by the TTA13 database. This alters the slope of the solidus line in the Al–Si phase diagram in a different manner. Considering the SBIN2 database, the initial solute content in the solid phase is ~0.48 wt.% Si. Higher solubility of solute in the solid means less solute rejected into the solidifying liquid and thus less amount of eutectic.

It is clear that calculations performed with the SBIN2 database are not according to the values shown in the literature [12], since the solubility limit of the solute element (Si) in the solid should not be higher than ~1.56 wt.% Si. Thus, the SBIN2 database is only used here for comparison. Therefore, the two solidification paths calculations were considered for comparison.

Figure 3.7 demonstrates the solidification path for the Al–3 wt.% Si alloy obtained from the 2D experimental solid fraction measurements and compared to the solidification path according to the TTA13 database. It is evident from the graph that at high temperatures overestimation of solid fraction as compared to

the solidification theoretical limits (lever rule and Gulliver–Scheil approximation) is large. The results fit between the limits when quenching at temperatures closer to the eutectic reaction.

Little differences were found with respect to the cooling and quenching rates in the samples quenched at low temperatures (below 595 °C); however, in the case of the samples quenched at 578 °C at $dT_q/dt= 50$ K/s, the solid fraction becomes larger than in the sample quenched at the same temperature but at 100 K/s. The sample having more solid corresponds to the one having coarse needle-like Si particles (Fig. 3.5c).

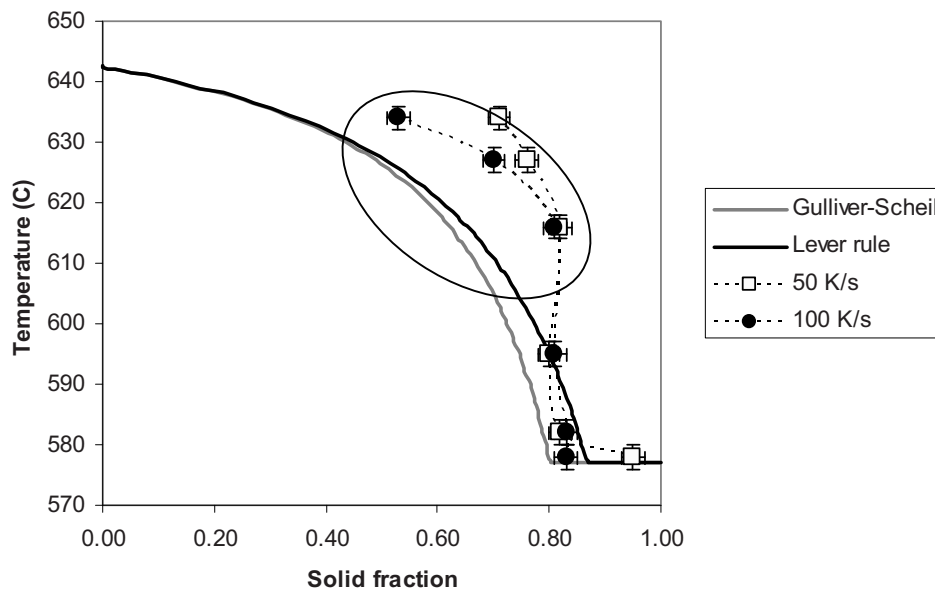


Figure 3.7. Solidification path of the Al-3 wt.% Si alloy, demonstrating the comparison between the calculated path according to the TTA13 database in *Thermocalc* and the experimentally obtained path.

On the other hand, differences in quenching rate do affect the solid fraction at temperatures above 616 °C (Fig. 3.7). This emphasises the sensitivity of this alloy to quenching at high temperatures. From the experimental solidification curves it is clear that overestimation overshadows the true solid fraction evolution.

By using the SBIN2 database, overestimation of solid fraction becomes considerably lower as demonstrated in Fig. 3.8. Also a greater tendency towards the Gulliver–Scheil approximation is observed at temperatures below 595 °C. But, still overestimation is present at high temperatures.

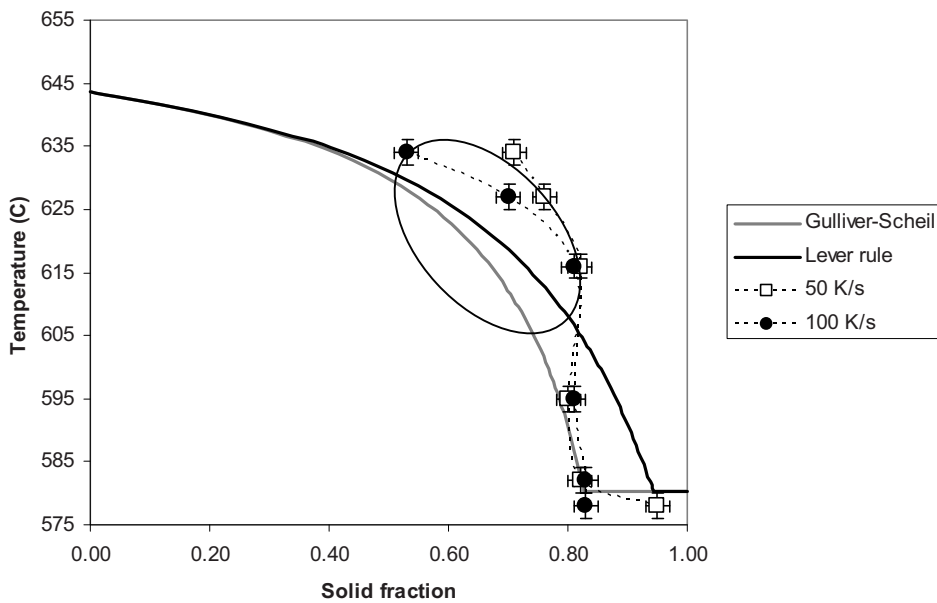


Figure 3.8. Solidification path of the Al–3 wt.% Si alloy, demonstrating the comparison between the calculated path according to the SBIN2 database in *Thermocalc* and the experimentally obtained path.

In order to determine if solute distribution in the solid phase obeys the Lever rule or Gulliver–Scheil approximation, microsegregation measurements were performed. These results are demonstrated in section 3.4 and a discussion about the structure development prior to and during quenching is given based on these results and constitutional analysis.

3.3.1.2. Solidification of an Al–7 wt.% Cu alloy

The microstructure evolution of the Al–7 wt.% Cu alloy quenched at ~50 K/s and 100 K/s is shown in Figs. 3.9 and 3.10 respectively. There are similarities in solid phase morphology between samples quenched at the same temperatures but different quenching rates. On the other hand, the samples quenched inside thin-walled graphite crucibles (i.e. $dT_q/dt= 100$ K/s) showed a regular distribution of the structure since liquid pools were found alternatively distributed between the solid phase. In contrast, the samples quenched in alumina crucibles (i.e. $dT_q/dt= 50$ K/s) demonstrated a rather irregular distribution of phases.

For comparing the solidification extremes, the TTA13 database and the SBIN2 database were used in *Thermocalc* software. From both databases, no differences were found in the phase diagram and therefore in the solidification paths, for that reason only the TTA13 database was used for comparison with experimental results. Accordingly, the solubility limit of Cu in the solid was found to be ~5.6 wt.% Cu (according to the phase diagram) and the initial solute content in the solid at the beginning of solidification was 0.7 wt.% Cu at 642 °C.

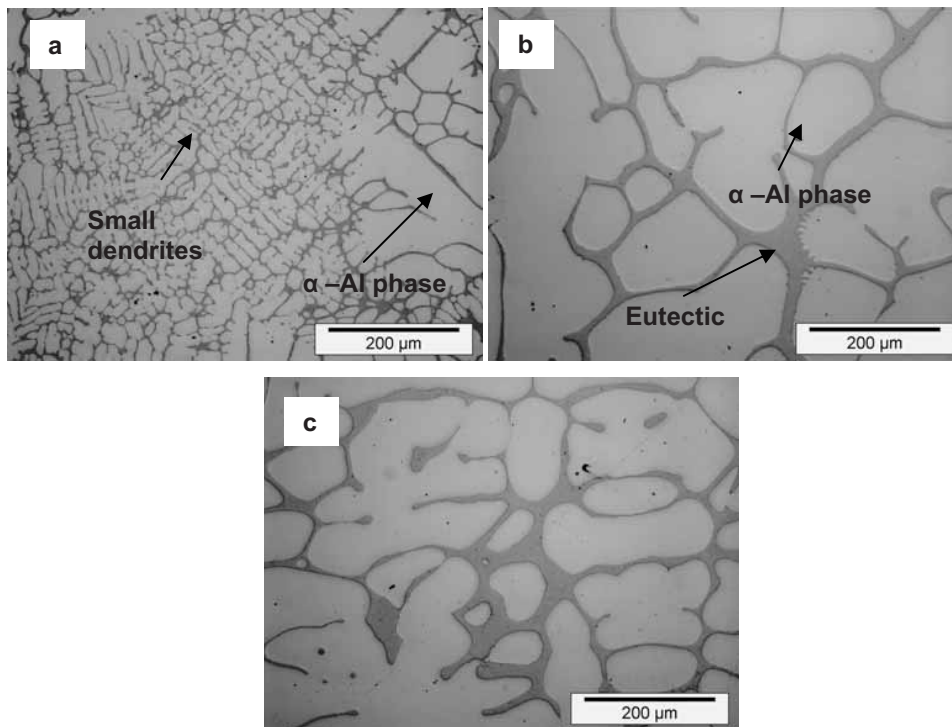


Figure 3.9. Al-7 wt.% Cu alloy samples quenched at ~ 50 K/sec showing the quenched structures at: (a) 637°C, (b) 595 °C and (c) 551 °C.

Figure 3.11 demonstrates the solidification path for the Al-7 wt.% Cu alloy based on the two solidification extremes (i.e. lever rule and Gulliver-Scheil approximation) according to the TTA13 database. The measured solid fraction is plotted on the same graph. The deviation of the experimentally obtained graph from the limiting theoretical models means that the solid fraction is overestimated based on the 2D image analysis. However, overestimation of solid fraction is lower as compared to the Al-3 wt.% Si alloy. Overestimation of solid fraction is only present at high temperatures and the differences in quenching rates (used in the present study) do not influence the solid fraction, at contrast to the Al-3 wt.% Si alloy. It can also be appreciated that the solidification tendency is towards Gulliver-Scheil approximation.

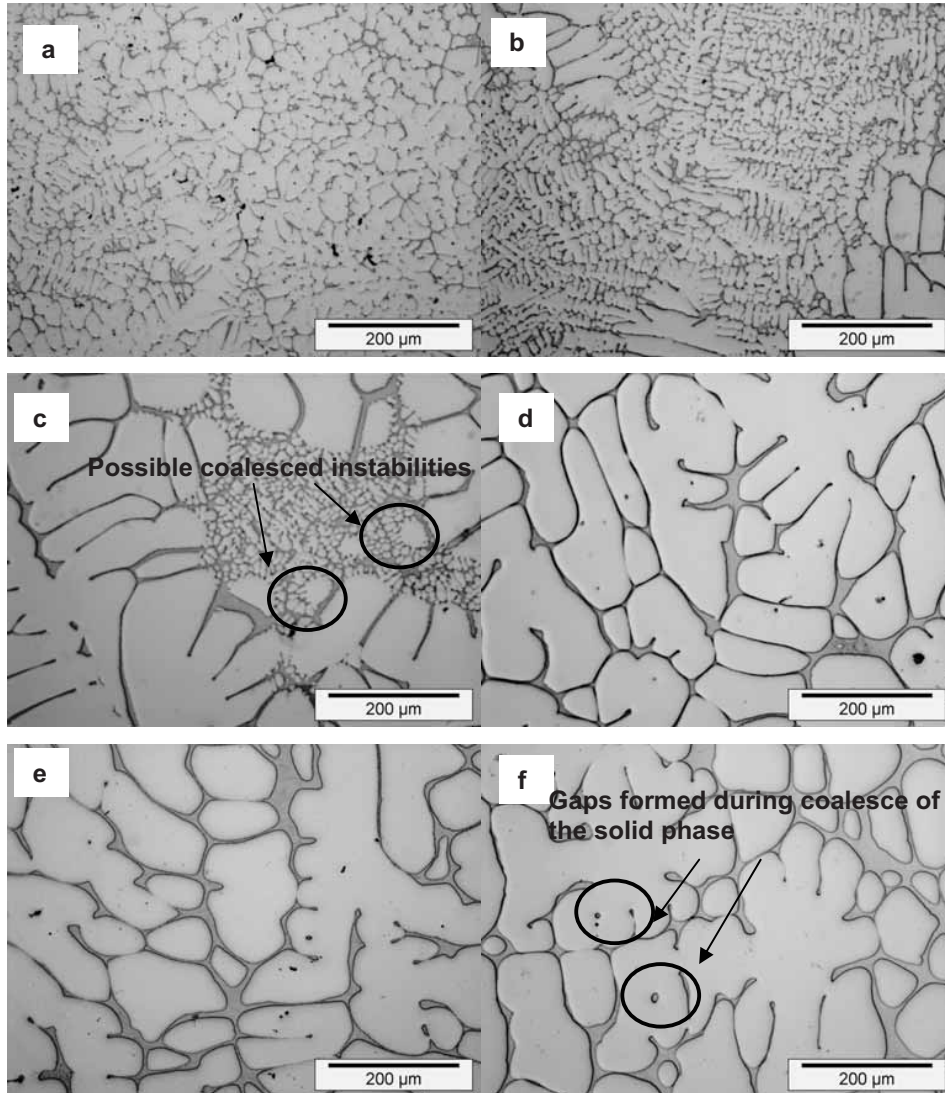


Figure 3.10. Al-7 wt.% Cu alloy samples quenched at ~ 100 K/sec showing the quenched structures at: (a) 637 °C, (b) 631 °C, (c) 620 °C, (d) 595 °C, (e) 583 °C and (f) 551 °C.

The sample quenched at 637 °C (equivalent to a solid fraction of ~ 0.23 according to Gulliver–Scheil and lever rule) demonstrated a highly interconnected structure involving both finer dendrites or instabilities and small dendrites developing during solidification (Fig. 3.10a). Due to this

interconnectivity and due to a structural length-scale that is rather similar between instabilities and small dendrites it was difficult to separate both structures for the measurements. Figure 3.12 demonstrates the structure of the sample quenched at 637 °C at a lower magnification. The similarities in length-scale between finer dendrites developing prior to quenching and instabilities are evident.

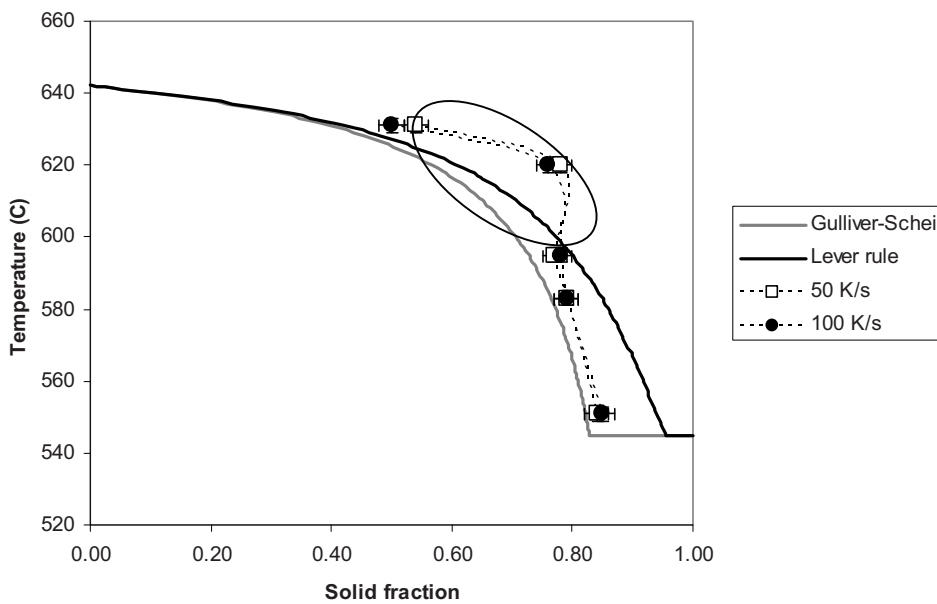


Figure 3.11. Solidification path of the Al-7 wt.% Cu alloy, demonstrating the comparison between the calculated path according to the TTA13 database in *Thermocalc* and the experimentally obtained path.

In the present study, the same overestimation tendency was observed for both alloys when quenching between solid fractions of 0.40 – 0.60. Therefore, it is required to understand the reasons for this overestimation within this solidification range.

Earlier the overestimation of solid fraction has been attributed to continuation of growth and coarsening during quenching [5-9]. Some experimental works

have refined the analysis of solid fraction by having a homogeneous globular structure or by holding isothermally the samples in order to stabilize the solid-liquid interface [6-9]. These procedures however do not demonstrated solid fraction evolution or morphology of solid phase during continuous dendritic unconstrained growth.

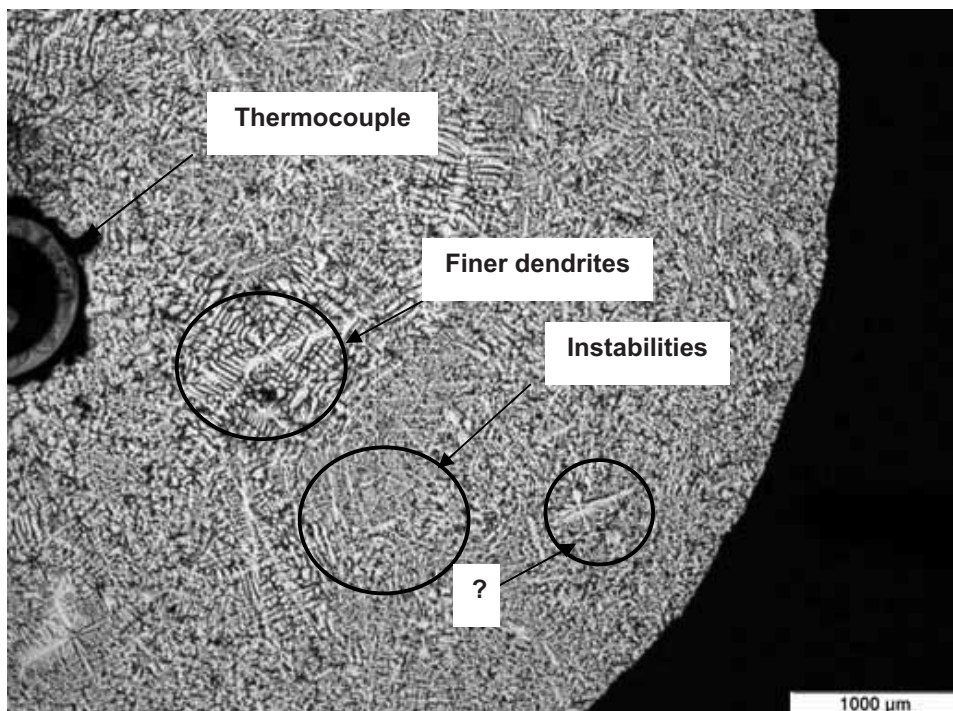


Figure 3.12. Image taken at a low magnification of the Al-7 wt.% Cu alloy quenched at a high temperature of 637 °C demonstrating the rather similar length-scale between finer dendrites developing prior to quenching and instabilities developing during quenching.

Since a dendritic structure developing under unconstrained conditions involves distribution of phases in 3D, a 2D analysis of such structures may give an erroneous stereological interpretation. Figure 3.10c shows small solid portions that could correspond to a destabilized quenched surface (i.e. dendrite branch tip) which may lead to overestimation of solid. In addition, since instabilities

development involves nucleation and propagation from the solid interface, quenching may produce coalesced instabilities. Also, during unconstrained growth conditions, dendrite envelopes may impinge onto each other during dendritic growth and quenching, producing coalescence. Microsegregation analysis could demonstrate if continuation of growth occurred during quenching giving overestimation of solid, this will be shown in section 3.4. Also, 3D microstructure reconstruction and analysis may explain the existence of overestimation by refining the stereological analysis of the structure. 3D reconstruction of representative samples is presented in section 3.5.

3.3.2. Morphology development during solidification from 2D analysis of quenched samples

From the present 2D analysis of images (Figs. 3.5, 3.6, 3.9 and 3.10) it can be seen that solidification of alloys has tendency towards Guilliver–Scheil approximation. It is possible to qualitatively study development of solid phase morphology during solidification assuming that this phase was preserved after quenching. Just as an observation, it can be seen in Figures 3.13a and b that dendrite branches are rather similar for both alloys, i.e. Al–3 wt.% Si and Al–7 wt.% Cu alloys. It is difficult to appreciate the extension of the size of the dendrites and degree of ramification since the structure develops in a 3D space. The 3D effect on structure development promotes dendrite branches to develop with different orientation.

Some rather small portions appeared as small globular dendrites, however in reality they correspond to transversal cross sections of other branches (highlighted in Fig. 3.13 inside rectangles). In contrast some other finer

globular solid portions may be coalesced instabilities developed during quenching (discussed in section 3.5). In Figure 3.13, the possible coalesced instabilities are demonstrated with two arrows. They were mainly located in liquid pools, regions where, apparently, dendrite envelopes meet.

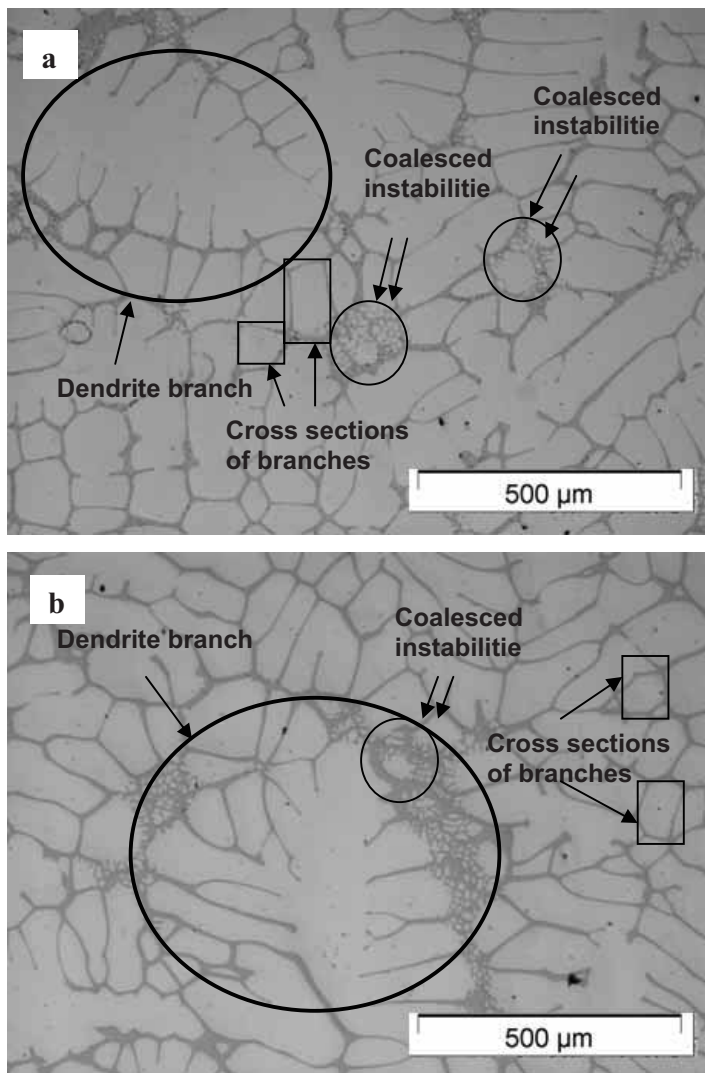


Figure 3.13. Dendrite branch morphology in the (a) Al-3 wt.% Si alloy and (b) Al-7 wt.% Cu alloy quenched at 627 and 620 °C (i.e. $f_{SS} \sim 0.5$ for both) respectively.

At lower magnifications (Figure 3.14), it can be appreciated how dendrite branches develop having different orientation and that liquid pools are distributed throughout the entire structure. Figure 3.14 shows the Al-7 wt.% Cu alloy quenched at 631 °C and at 100 K/s. Unconstrained solidification conditions implies growth of dendrites from different positions in a 3D space (Fig. 3.14). This sort of dendrite arrangement may lead to impingement of dendrite envelopes at certain places leading to overestimation of solid fraction after quenching. The following sections (based on solute distribution and 3D structure analysis) complement these observations in demonstrating that unconstrained solidification conditions may influence growth of dendrites in a more complex manner; and that overestimation of solid may be due to coalescence of instabilities during quenching.

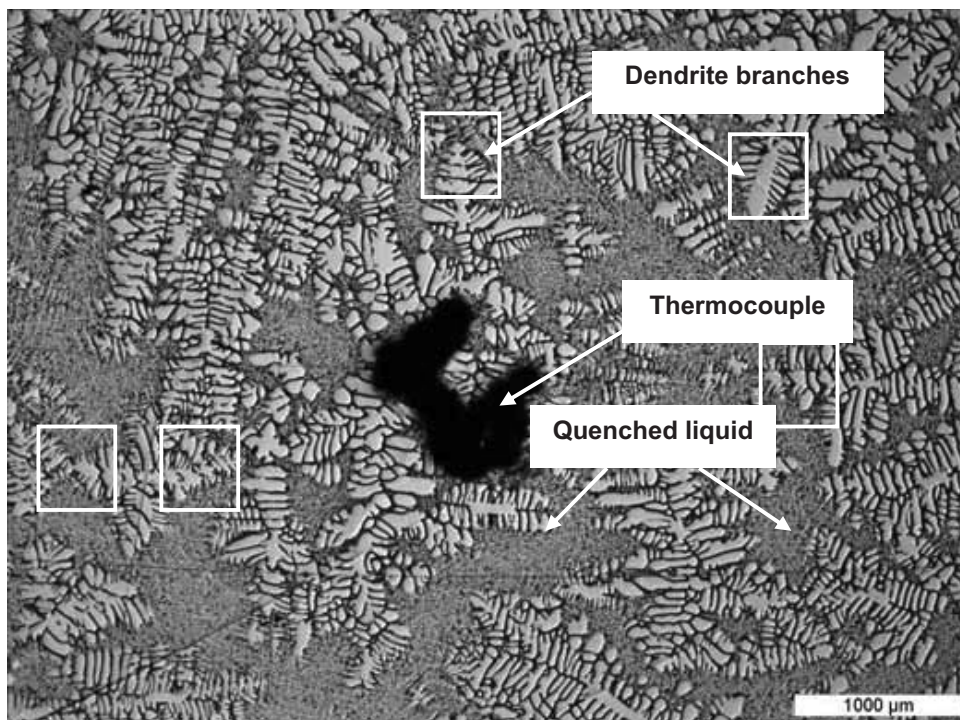


Figure 3.14. Al-7 wt.% Cu alloy quenched at 631 °C and at 100 K/s demonstrating homogeneous distribution of solid dendrites and former liquid pools during solidification.

3.4. Solute Distribution of Quenched Structures and Microsegregation

3.4.1. Solute distribution within the solid phase evolving prior and during quenching

The objective of the analysis of composition, i.e. solute distribution, was: 1) to determine a possible location, within the solid phase, where solute distribution starts to show discrepancies i.e. larger content values of solute compared to local equilibrium solidification calculations (i.e. Gulliver–Scheil and lever rule); based on this 2) to determine where the solid phase starts to develop during quenching; and 3) to determine the solid fraction which correspond to that developing prior to and during quenching.

From cross-sectioned images, the solute distribution within the solid phase or microsegregation was estimated as described in section 3.2.2. Figure 3.15a shows the image of a quenched structure and solute distribution along the dotted line shown in the image of the Al–3 wt.% Si alloy quenched at 616 °C. In the microsegregation profile it is possible to notice a sudden increase in solute content after a certain extent of the solid phase which indicates the beginning of instability development at the moment of quenching (Fig. 3.15b). This is schematically illustrated in Figure 3.16, where C_S^* is the solute content in the solid at the solid-liquid interface prior to quenching and $C_{S_q}^*$ is the solute content in the solid at the quenched interface. Figure 3.15 indicates a sudden change of slope after $\sim 85 \mu\text{m}$ indicating the growth of a finer instability during quenching. At this point the solute content corresponds to $C_S^* \sim 1.50 \text{ wt.\% Si}$. Later, in the solid at the solid–liquid interface, a solute content of $C_{S_q}^* \sim 1.98$

wt.% Si can be observed. Immediately after this point a larger increase in solute content appears, corresponding to the solute content in the liquid at the solid–liquid interface (eutectic composition), i.e. $C_S \sim 18$ wt.% Si. Fluctuations in solute content in the quenched liquid indicate destabilization of the former liquid during quenching. Thus, constitutional measurements in the quenched liquid are not as reliable as the measurements obtained in the solid.

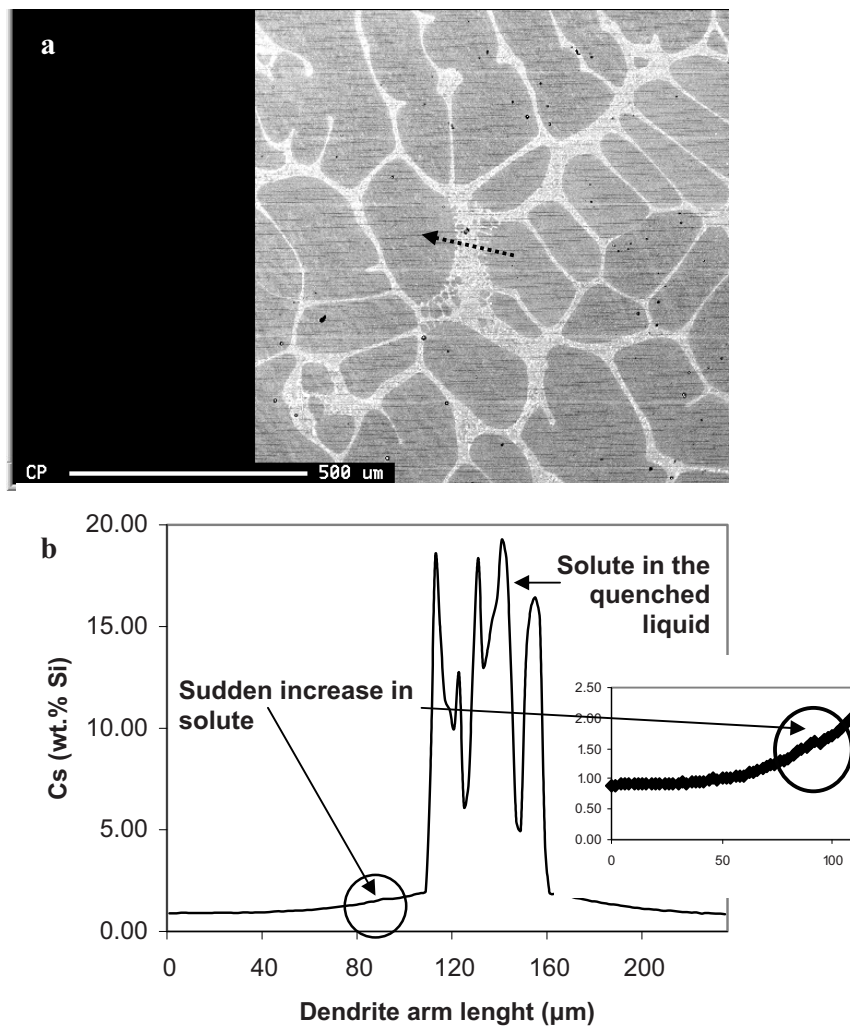


Figure 3.15. (a) Cross-section of an Al-3 wt.% Si alloy quenched at 616 °C and (b) microsegregation profile along the dotted line showed in (a).

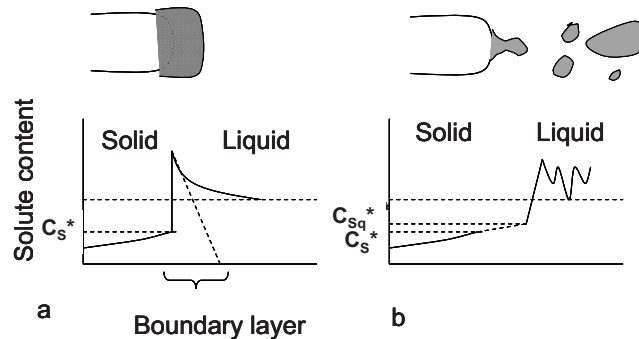


Figure 3.16. Schematic demonstration of solute profiles: (a) prior to quenching and (b) after quenching.

A continuous increase in solute distribution within the solid phase in Fig. 3.15b gives an indication of coring or microsegregation. This evidently indicates that the solidification process follows a non-equilibrium solidification path. In order to determine whether or not the Al–3 wt.% Si alloy, under the studied solidification conditions, obeys Gulliver–Scheil approximation during the entire solidification process, composition analysis was done on the samples quenched at different temperatures. The analysis of results indicated that all microsegregation profiles have the same behaviour of solute distribution i.e. same increase in solute in the solid. This indicates that the Al–3 wt.% Si alloy has tendency towards non-equilibrium solidification, i.e. Gulliver–Scheil approximation.

From spot chemical analysis the maximum solute content in the solid at the solid-liquid quenched interface was estimated to be $C_s^* \sim 2.15$ wt.% Si; this was obtained from the sample quenched close to the eutectic reaction (i.e. 578 °C). This value is larger compared to the solute limit solubility in the Al–Si phase diagram from the TTA13 database (obtained from *Thermocalc*) i.e. 1.56 wt. % Si; the solubility limit is closer to that obtained when using the SBIN2 database

i.e. 2.4 wt.% Si. This apparently means that the SBIN2 database determines the solidification path more closely to the present results. And as indicated in Fig. 3.8, the solidification path clearly lies close to the Gulliver–Scheil approximation.

Table 3.2 shows the measured solute content in the solid at the solid-liquid interface C_S^* in the samples quenched at different temperatures and quenching rates compared to the solute content C_S estimated from *Thermocalc*. It is clear that the studied alloy solidifies with a larger solute diffusivity in the solid as compared to the solidification path estimated using the TTA13 database. The SBIN2 database reveals that Si diffusivity in the solid may be indeed larger.

Table 3.2. Evolution of solute (Si) in the solid at the solid-liquid interface during solidification of an Al–3 wt.% Si alloy.

	SBIN2	TTA13 database	50 K/s	100 K/s
T (°C)	C_S	C_S	C_S[*]	C_S[*]
627	0,87	0,61	1,12	0,88
616	1,13	0,84	1,5	1,15
595	1,62	1,22	1,63	1,54
582	1,95	1,46	1,74	1,7
578	2,05	1,56	–	1,77

The Al–3 wt.% Si alloy is quite sensitive to the quenching rate as it is seen in the solidification paths (Figs. 3.7 and 3.8). Table 3.2 emphasizes this quenching sensitivity showing large differences in solute content at the interface due to quenching rate at 627 and 616 °C. Low quenching rates may allow coarsening and growth of the solid phase and thus overestimating the solid fraction developing prior to quenching. The quenching rate of ~100 K/s is more suitable for quenching experiments in order to preserve the solid phase evolving during solidification.

Moreover, it was found that the composition in the liquid ahead of the interface at different temperatures within the transition region does not correspond to that calculated from the solidification models. As demonstrated in Fig. 3.15, the solute content in the eutectic goes above 15 wt.% Si which is higher than the solute content at the eutectic point of the alloy (i.e. 12.5 wt.% Si). This means that solute diffused into the liquid during quenching, thus undercooling the liquid and shifting the eutectic point towards a larger solute composition value. It has been demonstrated elsewhere [13], that increasing the cooling rate of solidifying Al–Si alloys provokes undercooling of the liquid, which in turn leads to extension of the transition region by lowering the eutectic point. Since the quenching rate is rather high, the eutectic phase evolves in a very fine manner. Figure 3.17 shows the true morphology of eutectic phase (former liquid) at higher magnification.

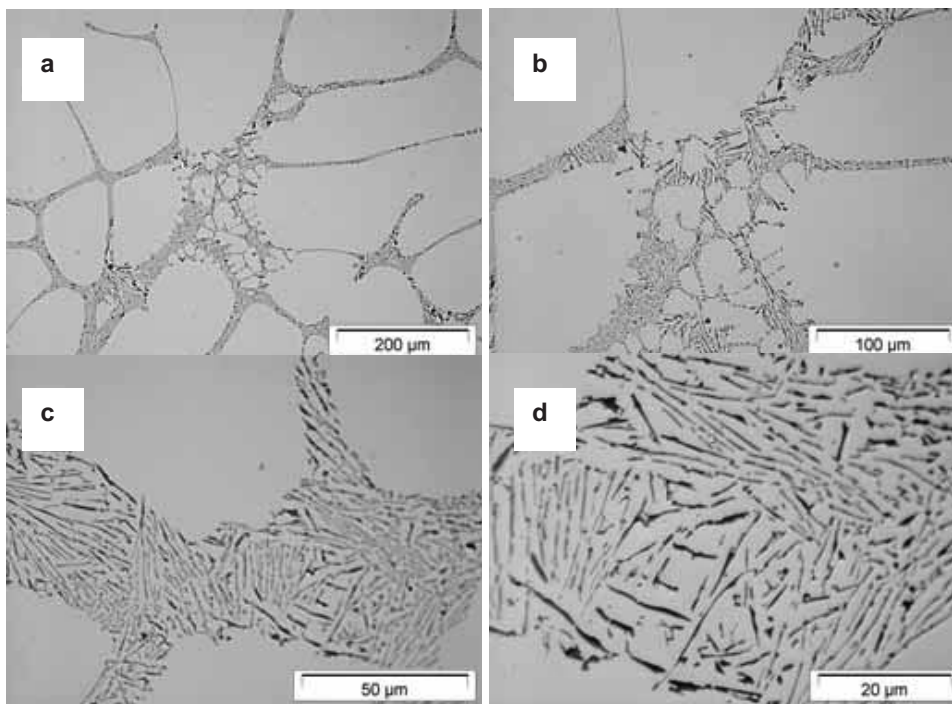


Figure 3.17. Eutectic morphology of the sample quenched at 627 °C at 50 K/s. The magnification of the image is increased from (a) to (d).

Figure 3.18 demonstrates the comparison of eutectic morphology between the sample quenched at 616 °C and that close to the eutectic reaction 578 °C at the same magnification. It is evident that quenching at high temperatures refines the eutectic phase due to an increase in cooling rate in the remaining part solidifying and to a higher undercooling achieved.

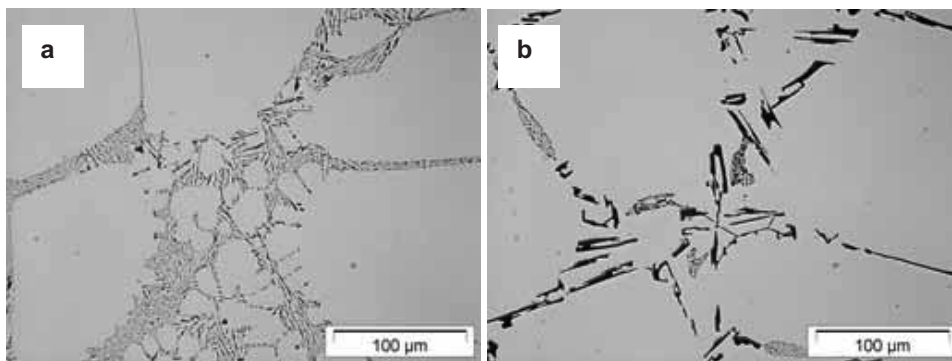


Figure 3.18. Comparison of eutectic morphology between (a) the sample quenched at 616 °C and (b) the one quenched close to the eutectic reaction 578 °C.

In the case of microsegregation in the solid phase, we can assume based on the line-scan measurements that a higher diffusivity of solute in the solid phase may be occurring during the solidification of the Al–Si alloy [14]. Also, due to the eutectic undercooling, some growth may be occurring during quenching at the quenching rate of 50 K/s, and thus under this conditions it is not possible to preserve the solid phase existing prior to quenching.

Even so, solute content analysis of the Al–Si alloy samples quenched at different rates does not explain the existence of solid phase overestimation. The samples quenched at 100 K/s presented solute contents at the solid–liquid interface C_S^* not larger than those calculated from local equilibrium analysis, which suggests that the measured solid fraction in the samples should be

roughly the same as the calculated equilibrium solid fraction, which is not the case.

For the case of the Al–7 wt.% Cu alloy, measurements in solute distribution demonstrated somewhat the same behaviour at the solid-liquid interface as illustrated in Fig. 3.19. Although, the slope in solute distribution within the solid phase was less pronounced, which suggests a more pronounced microsegregation in the solid as compared to the Al–3 wt.% Si alloy. The solute content in the solid at the solid-liquid interface, on the samples quenched at 551 °C close to the eutectic reaction was estimated from spot analysis and line-scan measurements, the value was found to be ~ 4.85 wt.% Cu, this value is fairly close to the maximum solute solubility in the solid i.e. 5 wt.% Cu at 551 °C according to the Al–Cu phase diagram.

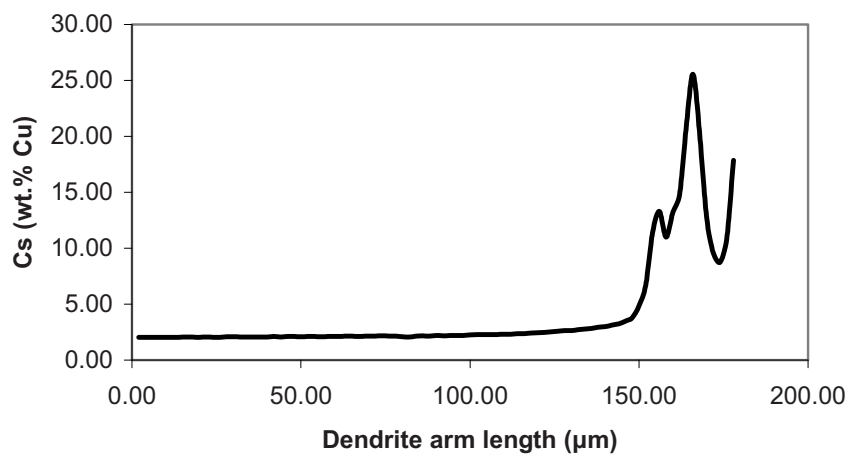


Figure 3.19. Line-scan measurement showing the microsegregation path along a dendrite arm in the sample quenched at 620 °C at 100 K/s.

Chemical distribution analysis did not give an explanation to the existence of overestimation of solid fraction when quenching at high temperatures during

the solidification of the Al–Si and Al–Cu alloys, but it provided the following conclusions which permit to understand their solidification path:

- 1) The solute content in the solid phase at the solid–liquid interface prior to quenching can be revealed as long as the quenching rate is high enough (i.e. ~ 100 K/s);
- 2) The solute content in the solid phase at the solid–liquid interface prior to quenching is close to the solute content calculated using the Gulliver–Scheil approximation; and
- 3) Both alloys demonstrated Gulliver–Scheil type solidification which means that microsegregation occurs during solidification.

The following section explores another possible reason for the existence of overestimation of solid fraction when quenching at high temperatures. The hypothesis of having solid portions within the quenched structure corresponding to portions that developed during quenching (i.e. coalesced instabilities) is further studied by 3D analysis of the microstructure. In order to analyse this possibility, the Al–7 wt.% Cu alloy was employed since it demonstrated less susceptibility to quenching rate, and thus a lower margin of error.

3.5. 3D Reconstruction of Instabilities

3.5.1. 3D-true morphology of instabilities: finer instabilities in the former liquid and at solid boundaries

As mentioned earlier, a proper stereological appreciation of a developing structure during unconstrained growth may be facilitated by reconstructing it in

3D. This section presents 3D reconstruction of the quenched structure. Samples exhibiting overestimation of solid fraction were partially reconstructed as spatial portions in order to visualize the morphology in 3D of the existing morphological features (such as coarse dendrite branches and instabilities).

Figure 3.20 shows 3D reconstructions of the main apparent features corresponding to overestimation found on the samples. These features are: true 3D morphology of fine instabilities (blob-like morphology or clusters) present in the as-quenched liquid (Fig. 3.20a) and instabilities at the coarse solid phase boundaries (Fig. 3.20b). The fine instabilities were found to be highly interconnected in 3D, some of them have a dendritic-like shape and others are more compacted having the appearance of clusters. Places where most of the instabilities were identified (at the solid boundaries and in the former liquid pools) were observed close to large liquid pools. Coarse equiaxed dendrites exposed to large liquid pools are more susceptible to solidification front destabilizations during quenching than regions that are in close proximity to developing neighbouring dendrites and where only narrow liquid channels are present (i.e. between high-order branches).

Interconnectivity of finer solid giving the appearance of a blob-like structure has earlier been demonstrated elsewhere in the case of stirred melts, also by reconstructing the structure in 3D [15]. The interconnectivity between instabilities suggests that during quenching they spread from existing solidified surfaces in a chain-like manner. The present observation shows the importance of having 3D reconstructions to visually appreciate the actual morphology.

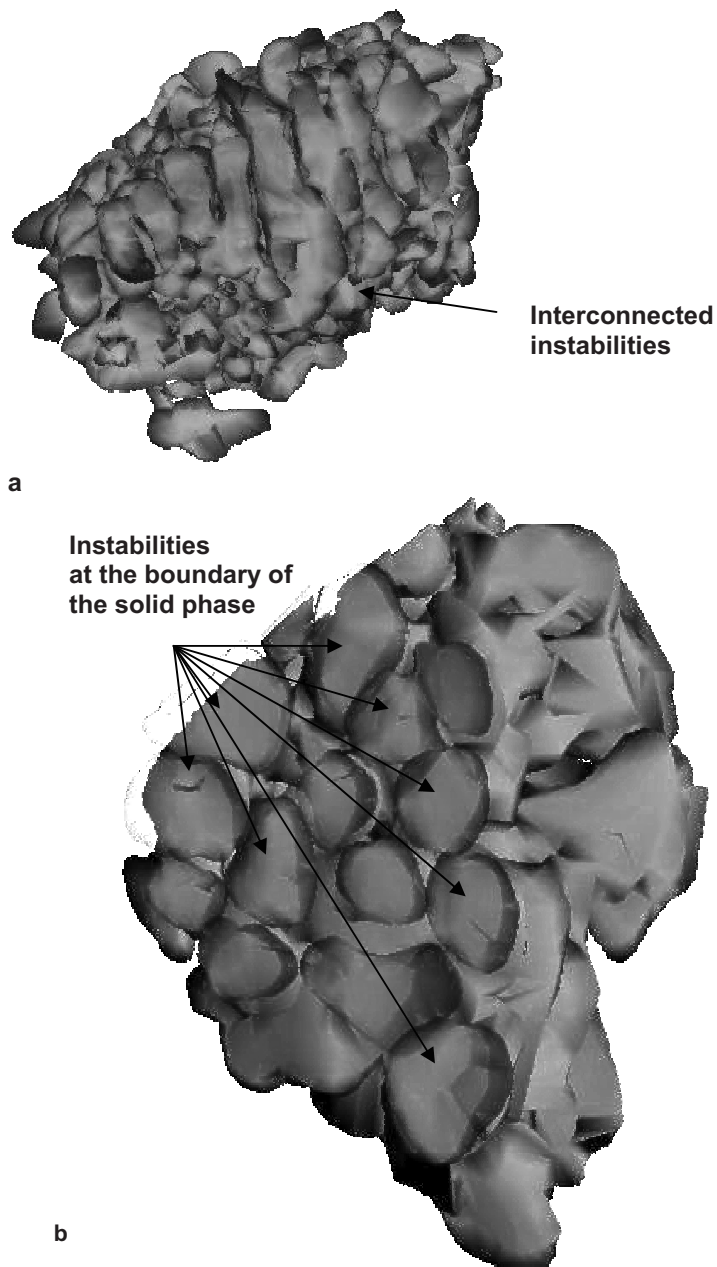


Figure 3.20. (a) Blob-like dendritic morphology of instabilities developed in liquid pools, and (b) instabilities developed at the boundaries of the solid phase, for the Al-7 wt.% Cu sample quenched at 631 °C.

3.5.2. 3D-true morphology of instabilities contributing to overestimation: coalesced instabilities

During quenching, instabilities that form at the solid boundary tend to propagate quite rapidly into the constitutionally and thermally undercooled liquid ahead. In regions where large liquid pools are present, instabilities easily propagate from the solid-liquid interface, whereas in rather confined spaces, instabilities from different regions may collapse and coalesce (not considering spaces within high-order branches of dendrites).

Coalesced instabilities can be easily and mistakenly considered as part of the solid phase prior to quenching from 2D sections, giving the overestimation of solid (Fig. 3.13). In the present study it was found that these coalesced instabilities actually exist. Figure 3.21 demonstrates portions of reconstructed dendrite branches found in the sample quenched at 631 °C which showed overestimation of solid fraction. It was found that dendrite branches exhibited coalescence between the solid phase boundary and finer instabilities ahead. As mentioned earlier, these coalesced portions were found in places that correspond to rather compact liquid pools where dendrite branches are coming from opposite directions meet (dendrites with different orientation).

Figure 3.22 demonstrates some of the image sections that were used for the 3D portion reconstructions in Figure 3.21. The arrows in the first image (Fig. 3.22a) demonstrate the apparent directions of dendrites in 2D. It is clear that dendrites meet around the region where coalescence was found (circled regions in Fig. 3.22). The section images have a thickness of $\sim 0.5\text{--}1\ \mu\text{m}$. The subsequent images in Fig. 3.22 were taken at different depths. From the series

of images it can be seen the change in morphology of coalesced instabilities in the z polishing direction.

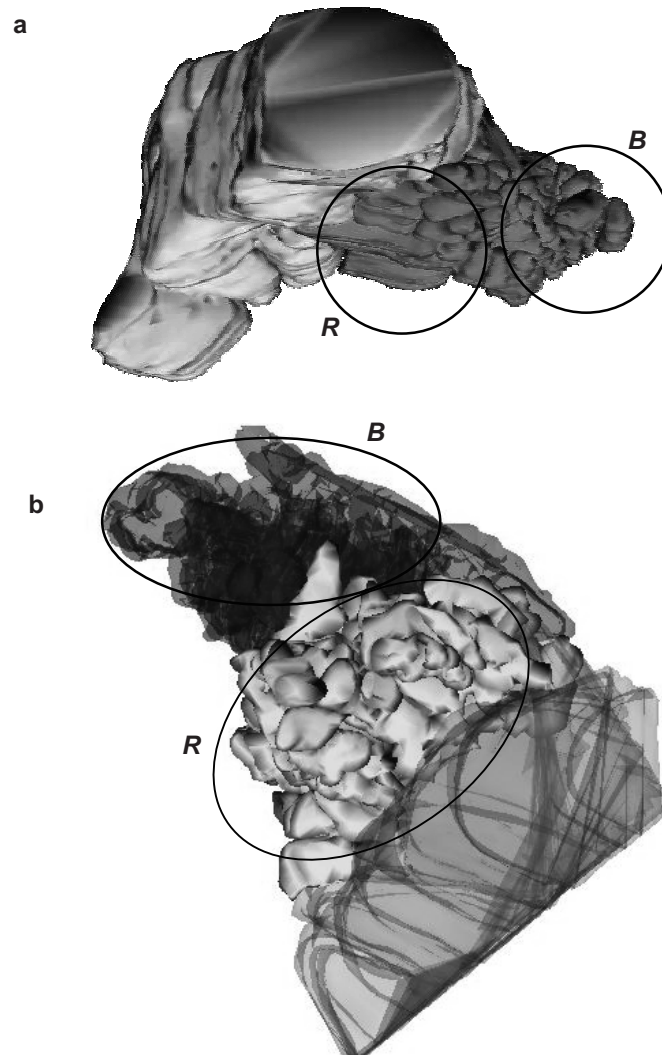


Figure 3.21. (a) Dendrite arm showing coalesced instabilities (highlighted in the R circle) between the solid boundary and finer instabilities (highlighted in the B circle) and (b) dendrite tip showing coalescence of instabilities between the solid boundary and finer instabilities. 3D portion reconstructions taken from the Al-7 wt.% Cu alloy quenched at 631°C. For the colour version of this figure see Figure A1 in Appendix.

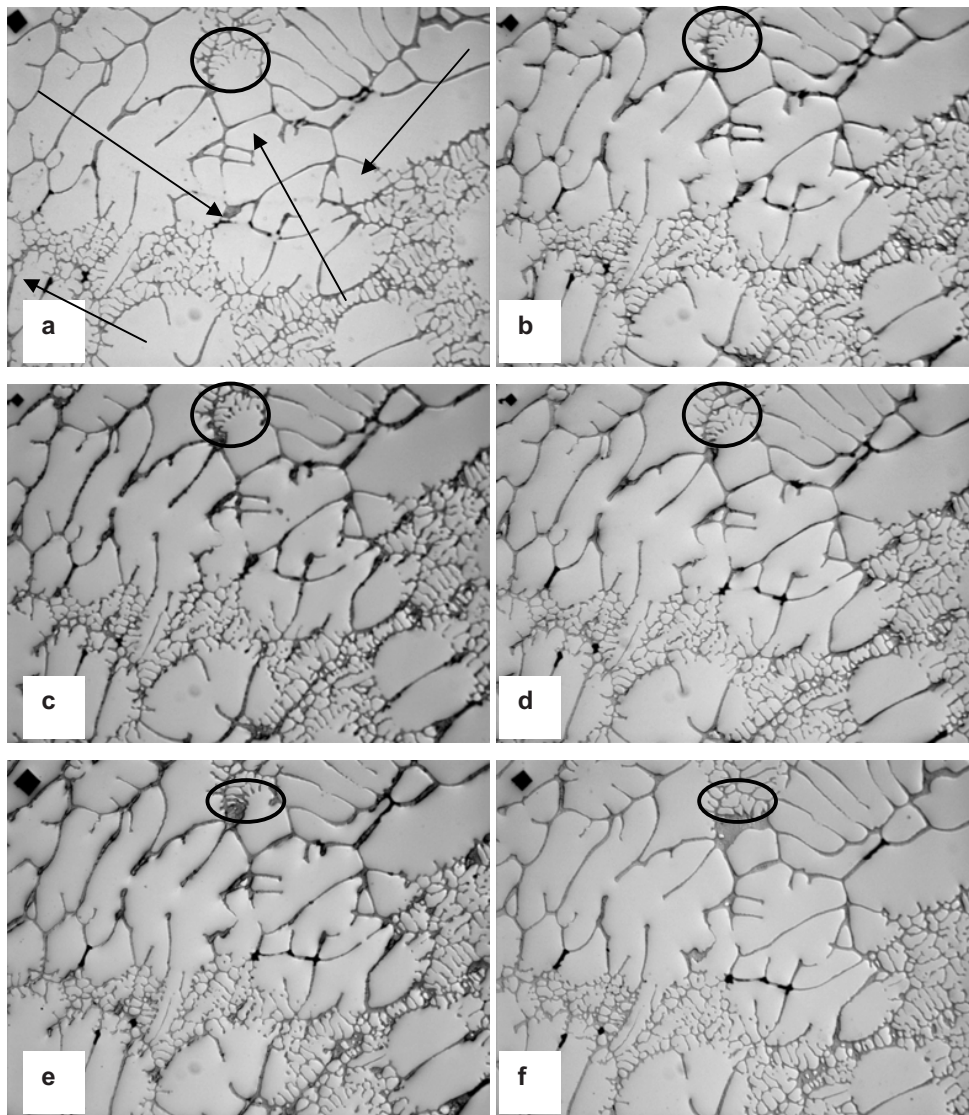


Figure 3.22. Images taken at different depths (thickness of sections $\sim 0.5\text{--}1\ \mu\text{m}$) demonstrating the region where coalescence shown in Fig. 3.21a was found. The arrows in first image demonstrate the apparent orientation of dendrites. The field of view corresponds to a size of $x=470\ \mu\text{m} \times y=498\ \mu\text{m}$.

Within the same volume of the Al-7 wt.% Cu alloy quenched at 631°C another dendrite branch exhibited coalescence at the tip. Figure 3.23 demonstrates a

360° visualization of this branch in 3D (image in transparent blue) showing in transparent red colour the coalesced instabilities.

In addition, a peculiar 3D morphological configuration was observed within the same structure. It was demonstrated for the first time that in reality dendrite branches can have a more complex accommodation in 3D when developing under unconstrained solidification conditions. Figure 3.23 differentiates with colours two dendrite branches which are apparently accommodated beside each other (branch 1 in colour blue, branch 2 in colour green). We named this morphological configuration “coupled dendrite branches”. In this sort of arrangement, a dendrite branch has a concave side (green dendrite branch) while another has a convex side (blue dendrite branch) where they are fitted together. It would be impossible to detect such accommodation if the 3D reconstructions were simply done by image stacking. In order to separate individual portions, the reconstruction has to be done manually by identifying the different corresponding features of each portion. This was done by identifying the different features during selection along with image selection during the reconstruction. 3D microstructure reconstructions done until now do not differentiate features existing within a complex dendritic structure. Typically 3D representations of structures only present a volume reconstructed from image overlapping [e.g. ref. 16]. This sort of reconstructions obviously cannot demonstrate true 3D geometrical arrangement of dendrites and their actual morphology as it is presented here.

Coupled dendrites branches are joined together at the base (not presented here). This adjunction between branches was noticed during image selection. This sort of dendritic configuration could develop within confined spaces of the structure. A number of images demonstrated similar configuration, having a sandwich-like accommodation of several dendrite branches.

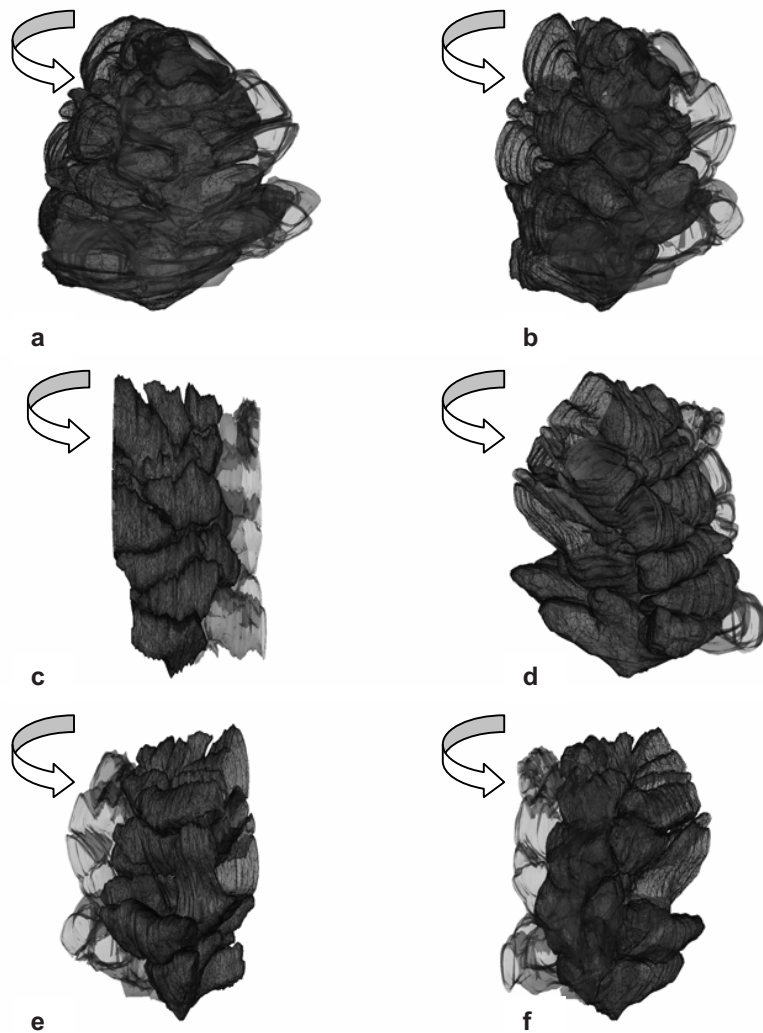


Figure 3.23. Couple dendrite branches developing due to tip splitting; where the transparent red portion corresponds to coalesced instabilities while the transparent green and transparent blue features correspond to a concave dendrite branch and to a convex dendrite branch, respectively. For the colour version of this figure see Figure A2 in Appendix.

Moreover, we found a triple tip splitting in the concave dendrite branch (green branch in Fig. 3.23c). Figure 3.24 demonstrates a close up to this branch. Tip splitting explains the development of coupled dendrite branches.

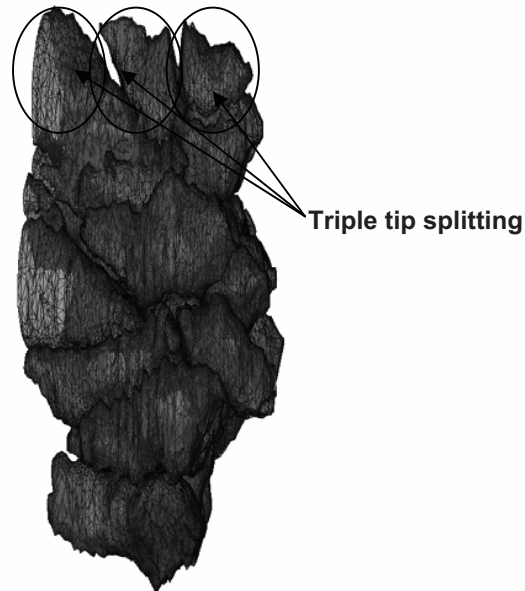


Figure 3.24. Dendrite branch after removing neighbouring dendrite branch exhibiting triple tip splitting. For the colour version of this figure see Figure A3 in Appendix.

It has been demonstrated that 3D microstructure reconstructions, along with visual identification of different features during image identification and selection, permit us to visualize the morphology of dendrites from quenched structures. The problem of overestimation has been related in part to coalescence of instabilities that occurs during quenching in regions where dendrites with different orientation meet during unconstrained growth (prior to quenching). By removing such features, a more accurate representation of the structure existing during solidification can be provided. The removal of coalesced instabilities would reduce overestimation. In the present study, coalescence was found in the 3D portion visualization of the sample quenched at 631 °C. Similar coalescence could also exist in the sample quenched at 620 °C which demonstrated a large overestimation of solid fraction as well. In fact, we observed 2D features within the structure of the sample quenched at 620 °C

which correspond to coalescence. Coalesce may be the cause of overestimation of solid fraction when estimating the solid fraction that existed prior to quenching (i.e. during solidification) from 2D image analysis of cross-sections.

The next section demonstrates, based on 3D microstructure reconstructions, the evolution of dendrite morphology and the mechanism of structure development during unconstrained growth is proposed.

3.6. 3D Estimation of Microstructure Development from 3D Reconstructed Structures

3.6.1. Solid fraction from 3D reconstructed images

The solid fraction was estimated from the 3D reconstructed images of the Al–7 wt.% Cu alloy samples (Fig. 3.25) and compared to the 2D measured solid fraction shown in Table 3.3. Also, the measurements are compared to the solid fraction obtained from the lever rule (f_{Si}) and from the Gulliver–Scheil approximation (f_{Ss}).

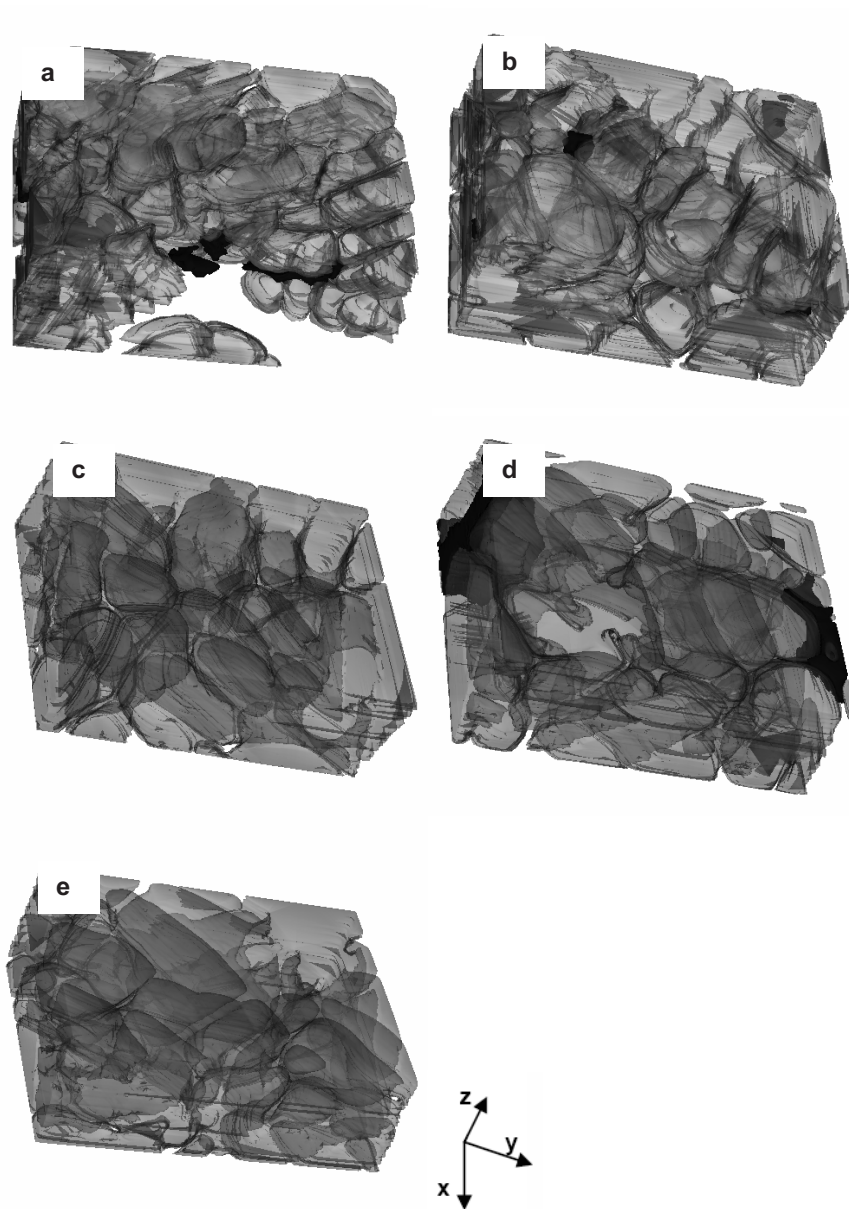


Figure 3.25. 3D microstructures of samples ($x= 318 \mu\text{m} \times y= 420 \mu\text{m} \times z= 155 \mu\text{m}$) quenched at: (a) 631 °C, (b) 620 °C, (c) 595 °C, (d) 583 °C and (e) 551 °C. Semitransparent grey and black colours represent the solid phase and porosity respectively. For the colour version of this figure see Figure A4 in Appendix.

In the present study due to image alignment and microstructure fitting for the 3D reconstruction, the selected area for reconstruction became smaller. For the microstructures quenched at T= 631, 620 and 595 °C, the reconstructed volume may have become non-representative of the entire microstructure. This is why the estimated 3D solid fraction at these temperatures became larger as compared to the measured 2D solid fraction (Table 3.3). On the other hand, samples quenched at low temperatures, close to the eutectic reaction, (i.e. 583 and 551 °C) demonstrated the same solid fraction when comparing both 2D and 3D measurements at the selected temperature. At these temperatures the solidification path has a tendency towards Gulliver–Scheil approximation. Therefore, it can be assumed that 2D statistical measurements of solid fraction are rather accurate when instabilities are not considered in the measurements (instabilities at the solid interfaces and apparent finer-structured clusters in the quenched liquid).

Table 3.3. Comparison between calculated solid fractions, 2D and 3D measured solid fractions.

Temperature (°C)	2D solid fraction (f_s) (error ~ ± 0.02)	3D solid fraction (f_{sv})	Lever rule (f_{sl})	Gulliver–Scheil approximation (f_{ss})
637	–	–	0.21	0.21
631	0.50 (0.45*)	0.59	0.41	0.37
620	0.80 (0.75*)	0.89	0.60	0.56
595	0.80	0.89	0.80	0.72
583	0.80	0.80	0.85	0.76
551	0.85	0.85	0.95	0.82

* After considering the coalesced instabilities, found within the 3D microstructure reconstructions, as part of the liquid prior to quenching and not as part of the estimated solid.

During 3D solid fraction measurements, coalescence of instabilities was taken into consideration. First, the coalescence was found to contribute about 0.05 to the apparent solid fraction. With taking into account this overestimation of solid fraction from coalesced instabilities in the 2D solid fraction measurements in the sample quenched at 631 °C, the solid fraction will turn out to be 0.45 which

is closer to lever rule $f_{SI} = 0.41$ (see Table 3.3). At the higher liquid fractions e.g. 637 °C, finer equiaxed may have developed freely and during quenching no close-range obstacles could have got into the way of developing instabilities during quenching. At 631 °C, however, dendrite envelopes might have met in some places producing some coalescence at the moment of quenching.

At 620 °C it was not possible to distinguish any features such as coalesced instabilities from the 3D reconstructions, and the 3D measurements gave also higher numbers as compared to 2D measurements, suggesting a non-representative reconstructed volume. However, 2D images (shown in Fig. 3.10c in section 3.3) showed similar features to those that have been interpreted as coalesced instabilities upon 3D reconstructions. Thus, if considering the same amount of overestimation due to coalescence f_S becomes 0.75 instead of 0.80 (see Table 3.3). Nonetheless, at this temperature overestimation still remains large. It is possible that at this stage of solidification ($f_{SI}=0.6$), impingement between dendrites, coalescence and coarsening occur and continue to develop during quenching, closing compacted spaces between dendrite branches. At the end, these phenomena produce large overestimation of solid fraction. The 3D reconstructions demonstrated gaps or spaces within the solid phase and entrapped former liquid which suggests the former explanations.

The 3D reconstruction shows that such gaps are not opened. These gaps could have been opened prior to quenching but it is difficult to confirm this from the present observations. At this stage of solidification, during unconstrained growth, thermal fields may overlap decreasing thermal gradients and delaying dendritic growth [17], enabling therefore morphological transitions such as coarsening and coalescence. It has been demonstrated by means of simulations of microstructure development that gap enclosure during coarsening exists at solid fractions between 0.5–0.8, where a minimum in the specific surface is

achieved during solidification (Fig. 3.26) [18]. From the present study it was found that such gaps exist between $f_{S_s}=0.6-0.95$ (Fig. 3.10).

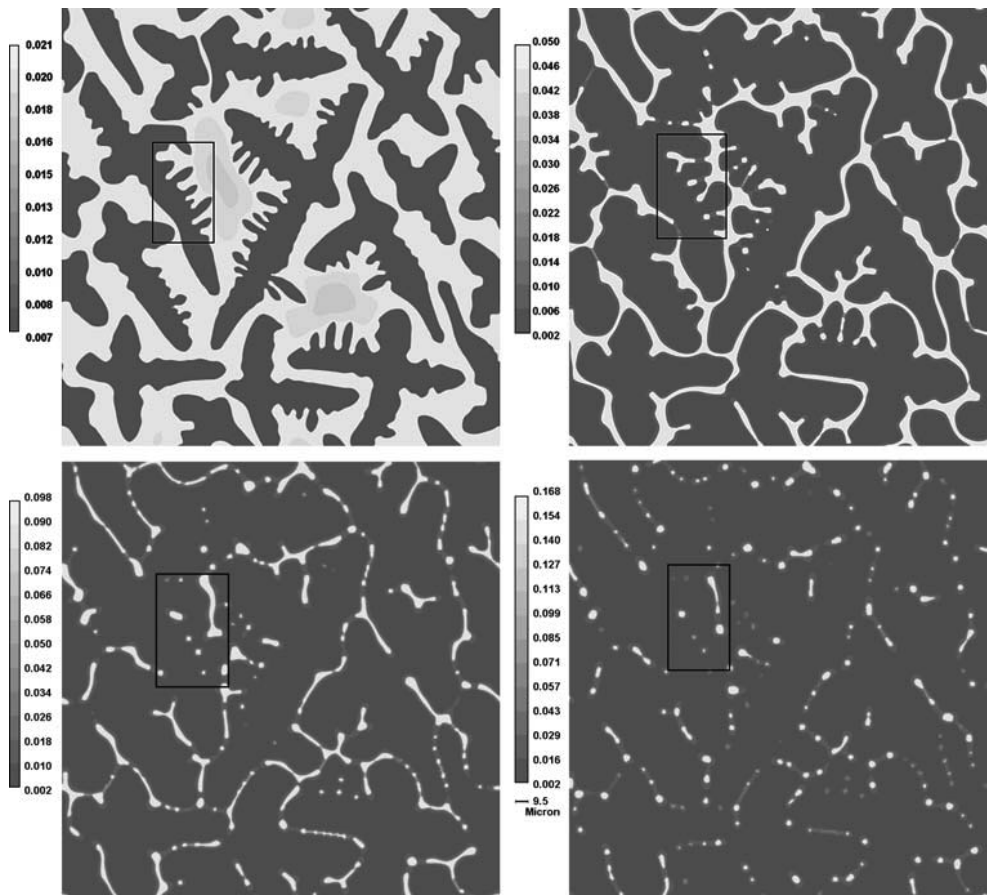


Figure 3.26. Simulated structure evolution of an Al-Cu alloy demonstrating the coarsening process and resulting enclosure of gaps within branches (after Du et al. [18])

At 595 °C 3D measurements also give a higher volume fraction of solid as compared to 2D measurements which indicates that the reconstructed volume may not be representative. Still, it is clear from 2D micrographs that the microstructure at this temperature is much more compact and liquid mainly occupies narrow channels between dendritic arms suggesting that 2D measurements of solid fraction can be accurate. The solid fraction at this

temperature ($T= 595\text{ }^{\circ}\text{C}$) fits lever rule which might mean that during relatively slow cooling, before quenching, some back diffusion may have occurred. Then at the near end of solidification, at $T= 583$ and $551\text{ }^{\circ}\text{C}$, solidification has tendency towards Gulliver–Scheil approximation suggesting that microsegregation exists within dendritic arms and the amount of remaining liquid to solidify as eutectic should, therefore, be higher than that resulting after equilibrium solidification [3].

3.6.2. Surface-to-volume ratio measurements

In order to follow the 3D morphology development of the solid phase during solidification the surface-to-volume ratio S_V was estimated. Figure 3.27 demonstrates S_V as a function of temperature. S_V decreases gradually from $0.07\text{ }\mu\text{m}^{-1}$ to $0.05\text{ }\mu\text{m}^{-1}$ without considering the sample quenched at $620\text{ }^{\circ}\text{C}$. The sample quenched at $620\text{ }^{\circ}\text{C}$ showed a S_V value equal to the sample quenched close to the eutectic line i.e. $0.05\text{ }\mu\text{m}^{-1}$. The low S_V value in the sample quenched at $620\text{ }^{\circ}\text{C}$ demonstrates the lowering in surface area due to coarsening and coalescence occurring during quenching as mentioned before. As reported elsewhere [18], coarsening and coalescence between dendrite branches diminishes S_V , in this case coarsening and coalescence is accelerated during quenching. Thus, the quenching sensitivity to overestimation of the alloy is higher at this intermediate temperature $\sim 620\text{ }^{\circ}\text{C}$ (i.e. $f_S \sim 0.60$). This may be due to an overlapping of thermal fields which delay dendrite growth, enhancing thus other morphological phenomena such as coarsening and coalescence.

The surface-to-volume ratio as a function of temperature demonstrates how the microstructure changes from a finer $0.07\text{ }\mu\text{m}^{-1}$ to a coarser dendritic structure $0.05\text{ }\mu\text{m}^{-1}$. It is clear that the quenching of the solid phase produces reasonable results providing the gradual morphological transition from a finer to a coarser

dendritic structure, which means that quenching, under the present experimental conditions, retains somewhat the morphology of the solid phase. Thus, providing the variation tendency of S_V during solidification which is with accordance to other studies, where S_V was determined from in-situ microtomography experiments [16].

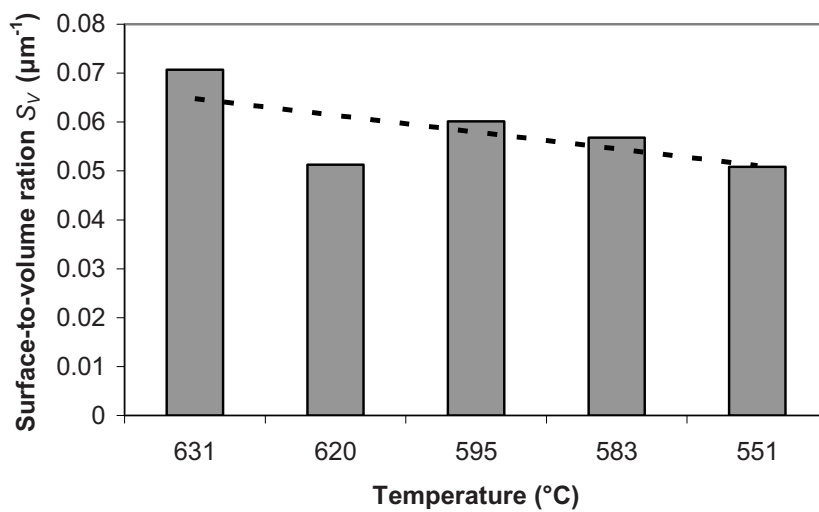


Figure 3.27. Estimated surface-to-volume ration from the 3D reconstructed solid phase as a function of temperature.

3.6.3. 3D morphological evolution of high-order dendrite branches

From 2D cross-section images it is possible to detect the structure of the solidifying Al–3 wt. % Si and Al–7 wt.% Cu alloy as being dendritic. Dendrites branches develop from coarse equiaxed dendrites, most of them being very large. However, a full appreciation of the microstructure, especially morphology of high-order branches, is not possible from simple 2D

observation. The present section demonstrates 3D portions of the reconstructed microstructures showing a complex morphology of dendrite branches. It is important to know the morphology of high-order branches since these will determine the interdendritic liquid flow during the entire solidification process and thus influence the development of the structure.

Figure 3.28 demonstrates the features that suggest the occurrence of coarsening, coalescence and competitive growth during the solidification of the Al-7 wt.% Cu alloy. Figure 3.28a shows a well developed typical dendrite branch found on the sample quenched at 620 °C. The main stem is composed of coarse secondary dendrite arms and tiny dendrite arms which are left behind due to competitive growth and dendrite coarsening due to remelting according to the Ostwald ripening mechanism. Competitive growth during the solidification of columnar dendrites has been reported before and is a common phenomenon occurring during solidification [19,20]. As suggested elsewhere [19,20] it is difficult to know if competitive growth may be a resulting effect of dendrite remelting according to the mechanism proposed by Kattamis et al. [21] (i.e. radial dissolution of weak branches and thickening of strong ones). We assume from the shape of the strong arms, which are thicker at the tip, that coarsening is occurring at the same time as competitive growth is happening. Figure 3.28b shows in 3D other dendrite arms, which also suggests coarsening by remelting; this can be observed from the central dendrite arm which thickens at the expense of the two neighbouring arms.

Coalescence of dendrite branches was observed frequently in the entire quenched structures. Dendrite branches coalesce and impinge onto each other during solidification. Complex dendrite coalescence configurations were found within the structures. Figure 3.28c demonstrates dendrite arms being coalesced giving a complex morphology close to the dendrite arm tip.

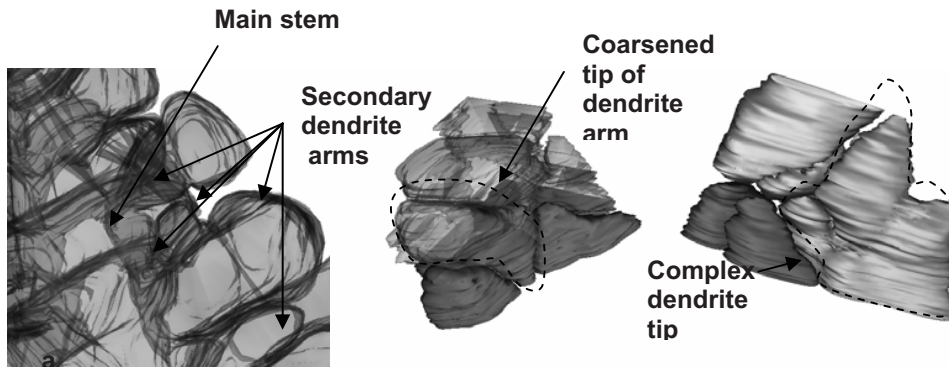


Figure 3.28. (a) Dendrite found in sample quenched at 620 °C; morphology of secondary dendrite arm tips in sample quenched at (b) 620 °C and (c) 583 °C.

Unconstrained growth induces the development of a highly interconnected dendrite structure due to coalescence. We assume that coarsening and coalescence starts as soon as dendrite envelopes start to meet due to a deceleration in local dendrite growth due to overlapping of thermal gradients as suggested elsewhere [17]. Steinbach et al. have demonstrated by dendrite growth simulations the deceleration of dendrite tip growth [22] due to the interaction of thermal fields (lowering undercooling). In our investigation, since the structure develops in 3D, it would be expected to have a stronger decrease in growth velocities.

Moreover, the reconstructed images can reveal the true 3D tip morphology of dendrite branches. Figure 3.29 demonstrates the morphology of a tip of a dendrite branch reconstructed in 3D from the sample quenched at 595 °C. The tip has a pentagonal-type geometry and this type of morphology was found throughout the entire solidification of the structure. It is important to understand the development of the tip of dendrite branches since it will determine the

undercooling, tip velocity and development of following instabilities along the main dendrite trunk (development of dendrite arms) [23,24]. Most of the studies on dendrite solidification have assumed dendrite tip morphology as having a parabolic morphology [1,2,23,24]. As presented here, another type of tip morphology may exist during the solidification of dendritic structures. It is evident, that the true morphology of features within a structure developing in 3D can only be appreciated by reconstructing it in 3D.

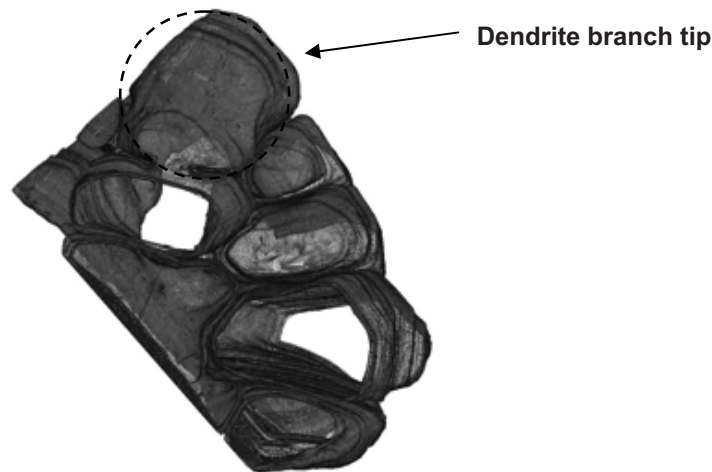


Figure 3.29. 3D morphology of dendrite branches developing during solidification.

3.7. Concluding Remarks

Overestimation of solid fraction was found when studying samples that were quenched during solidification. Samples quenched at high temperatures (i.e. low solid fractions $f_{S_s} \sim 0.2-0.5$) demonstrated larger overestimation of solid than samples quenched close to the eutectic reaction (i.e. high solid fractions $f_{S_s} \sim 0.7-0.9$). Solute distribution analysis and 3D microstructure reconstructions allowed us to uncover some of the reasons of overestimation from 2D cross-

section images and to minimize this error in order to describe the possible solidification path of the alloy.

It was found that quenching does interrupt solidification as long as the quenching rate is high enough. Thus, it is possible to identify the solid phase prior to and during quenching. By using microsegregation analysis, it was demonstrated that the solute content in the solid at the solid–liquid interface of the quenched samples correspond to that obtained with the Gulliver–Scheil approximation at different solid fractions. But still, after this analysis, it was not possible to deduce the reason of overestimation.

3D microstructure reconstructions, however, allowed the distinction of features presumably leading to the wrong stereological interpretation of the solid phase and thus erroneous estimation of solid fraction (overestimation). Coalesced instabilities were the features associated to the overestimation of solid fraction and it was possible to identify these features by reconstructing portions of the structures in 3D.

Our explanation for the existence of coalesced instabilities developed during quenching is as follows:

- 1) Unconstrained growth conditions of dendrites leads to complex morphology development due to 3D structure development;
- 2) Dendrite envelops may impinge into each other due to this solidification conditions;
- 3) During dendrite impingement, solutal and thermal gradients may overlap creating localized regions were coarsening and coalescence can be enhanced;
- 4) During quenching, finer dendrites (i.e. instabilities) appear and coalesce due to the compactness of localized regions (i.e. were dendrite envelops growth towards each other); and

5) 2D image cross-sections analysis can give wrong results when estimating the solid fraction developing prior to quenching (i.e. during solidification).

After these considerations, the following microstructure evolution path is suggested based on 2D–3D microstructure analysis and solute distribution:

- 1) Unconstrained growth of dendrites in 3D spaces evolves in a complex manner;
- 2) Dendrite envelops may eventually meet in certain places;
- 3) Due to this interaction, solutal and thermal gradients may overlap;
- 4) This behaviour lowers the growth of dendrites and may allow other phenomena to occur, such as coarsening and coalescence;
- 5) The occurrence of these phenomena in confined spaced within the microstructure can lead to complex morphology development, such as development of what we called “coupled dendrite branches” and complex dendrite tip morphologies.

3D microstructure reconstruction allowed distinguishing features which are difficult to observe in 2D images. Further stereological analysis in 3D may improve our understanding of structures developing during solidification. 3D analysis is required in structures developing under unconstrained solidification conditions in 3D spaces.

References

- [1] A.K. Dahle, D.H. StJohn, *Acta Mater.* 47 (1999) 31.
- [2] M.C. Flemings, *Solidification Processing*, McGraw-Hill, New York, 1974.
- [3] W. Kurz, D.J. Fisher, *Fundamentals of Solidification*, 3rd ed. Trans. Tech. Publications, Aedermannsdorf, Switzerland, 1992.
- [4] Ø. Nielsen, L. Arnberg, A. Mo, H. Thevik, *Metall. Mater. Trans. A* 30A (1999) 2455.
- [5] S.W. Chen, C.C. Huang, *Acta Metall.* 44 (1996) 1955.
- [6] M. Rettenmayr, O. Pompe, *J. Cryst. Growth* 173 (1997) 182.
- [7] Ø. Nielsen, S.O. Olsen, *Transactions of the American Foundryman's Society* 110 (2002) paper 02-096.
- [8] O. Pompe, M. Rettermayr, *J. Cryst. Growth* 192 (1998) 300.
- [9] E. Tzimas, A. Zavaliangos, *J. Mater. Sci.* 35 (2000) 5319.
- [10] J.C. Fiala, *J. Microscopy Pt 1* 218 (2004) 52.
- [11] D. Brandon, W.D. Kaplan, *Microstructural Characterization of Materials*, Wiley England, 2001.
- [12] N.A. Belov, D.G. Eskin, A.A. Aksenov, *Multicomponent Phase Diagrams: Applications for Commercial Aluminium Alloys*, Elsevier, Amsterdam/Boston, 2005.
- [13] D.M. Stefanescu, *ASM Handbook: Casting*, 10th ed. ASM International, vol. 15, 1991.
- [14] T. Kraft, Y.A. Chang, *J. Metals* 47 (1997) 20.
- [15] B. Niroumand, K. Xia, *Mater. Sci. Eng. A* 283A (2000) 70.
- [16] O. Ludwig, M. DiMichiel, L. Salvo, M. Suéry, P. Falus, *Metall. Mater. Trans. A* 36A (2005) 1515.
- [17] J.C LaCombe, M.B. Koss, M.E. Glicksman, *Physical Review Letters* 83

(1999) 2997.

[18] Q. Du, D.G. Eskin, A. Jacot, L. Katgerman. *Acta Mater* 55 (2007) 1523.

[19] E. Brener, D. Temkin, *Phys. Rev. E* 51 (1995) 351.

[20] Q. Li, C. Beckermann, *Acta Mater.* 47 (1999) 2345.

[21] T.Z. Kattamis, J.C. Coughlin, M.C. Flemings, *Trans. TMS_AIME* 239 (1967) 1504.

[22] I. Steinbach, H.-J. Diepers, C. Beckermann, *J. Cryst. Growth* 275 (2005) 624.

[23] G.P. Ivantsov, *Doklady, Akademii Nauk SSSR* 58 (1974) 567.

[24] A. Papapetrou, *Zeitschrift für Kristallographie* 92 (1935) 89.

Chapter 4

Microstructure Development during Constrained Solidification Conditions¹

Chapter 4 is based on in-situ analysis of directionally solidified samples (as described in Chapter 2). High-brilliance synchrotron X-radiation microscopy allowed in-situ observation of the evolving microstructure during solidification of aluminium alloys. New insights into microstructure development of solidifying columnar dendrites are presented. The influence of the structure geometrical arrangement on coarsening and growth kinetics is demonstrated. Also, a new mechanism of fragmentation due to solute enrichment is suggested.

¹ Chapter 4 is based on publications: 4, 5, 10–12 (see publications on pages 199, 200).

4.1. Introduction

Much of the analysis of coarsening in metallic-opaque systems was previously performed over post-solidified samples. By this means it is not possible to observe local velocity fluctuations and real-time evolution of microstructure. Many of the experimental studies reported in the past were also carried over steady-state solidification conditions [1]. In real casting processes, solidification will most often involve transient growth velocities due to thermal gradients existing according to the cast dimensions and shape. Transient solidification conditions have proven to influence microstructure evolution. In addition, the solidification direction (with respect to gravity) influences liquid flow and thus the development of dendrites [2,3]. It has been found that the primary dendrite arm spacing becomes larger when solidifying upwards due to solute accumulation between dendrites [4-6]. Drainage or enrichment of rejected solute during growth depends on the direction of growth [5]. Also, this depends on the density of rejected solute [6]; e.g. drainage occurs during downward solidification for the case of alloys with high density solute elements [5]. Liquid flow due to transient conditions and direction of solidification may not only affect the primary spacing but also the development of high-order branches deep in the mush [5].

In addition, as has been suggested elsewhere [7], secondary dendrite arm spacing (SDAS) measurements may not be a reliable means for studying coarsening since during continuous solidification other phenomena such as competitive high-order branch growth [8] may obscure accurate analysis. Thus, an in-situ analysis of coarsening during dendritic growth is required for a better understanding of microstructure development and a more accurately assessment of structure and defect development.

Recently, there has been several reports on the use of high-brilliance synchrotron X-radiography and tomography for studying coarsening phenomena [9-12]. Coarsening of secondary dendrite arms has been attributed to two main mechanisms: remelting and coalescence of dendrite branches [9,10]. Also, a lower coarsening exponent n (i.e. < 0.3) has been suggested as the value corresponding to pure coarsening kinetics [11,12].

Furthermore, the columnar-to-equiaxed transition (CET) that may occur during natural convection conditions is an important morphological transition which is not yet completely understood. Detachment of crystals from the dendritic network during solidification, so-called fragmentation, has been proposed as one of the feasible mechanisms to cause CET [5, 13-16], grain refinement, and the appearance of stray crystals in commercial castings [17, 18].

Both mechanical breakdown and remelting of dendrite arms have been considered to cause fragmentation. However, it is clear that mechanical forces need to be substantial in order to detach pieces of solid from the ductile dendrite network. It has been demonstrated by fluid-flow calculations that such processes are unlikely to occur under natural convective conditions [5, 19, 20]. Remelting at the neck of dendrite arms during coarsening [5, 21-23, 24,25], solute enhancement [5, 13, 25-28] or recalescence [5, 14] has been considered as potent mechanisms for initiation of fragmentation. The detailed microstructural and thermo-solutal conditions that cause remelting, however, still remain to be fully clarified. Moreover, CET and other related phenomena require survival of the fragments from dissolution (remelting) [29] and further transport of those that survive from the mush to the solidification front [5, 15, 16, 30].

Previous studies have proven that fragmentation can occur naturally during coarsening or due to recalescence upon eutectic solidification [5]. Fragments

that form deeper in the mush during these processes, however, hardly affect the solidification pattern [1-25, 31], since their survival and transport through a low-permeable region is often difficult [5, 29]. Due to better chances for survival and much easier transport, fragments detached by remelting at the root of high-order branches, closer to the solidification front, exhibit much greater potential to influence the structure development [5].

In order to clarify mechanisms behind dendrite detachment, experimental methods should be devised so as to permit in-situ studies of both morphological and solutal changes. High brilliance synchrotron X-radiation imaging has been employed recently to study several important phenomena that occur during alloy solidification [5, 20, 28, 32-35], and is, at present, the best method to obtain simultaneous and real time data during solidification on morphology evolution, microstructural transitions and micro-constitutional variations in the liquid phase [5, 32, 33].

In several earlier experimental studies, fragmentation due to remelting has been facilitated by some external manipulations of the solidification conditions, i.e. reheating, controlled variations in growth rate or induced liquid flow [5, 13, 19, 25-28, 32-35]. Thus, experimental analysis on fragmentation occurring during natural continuous growth of dendrites, during non-forced conditions, has not been presented yet.

This chapter is based on the in-situ analysis of local growth and coarsening kinetics during upward and downward directional solidification. Also, in-situ observations of dendrite fragmentation that occurs during natural transient solidification conditions are analyzed. For the first time, fragmentation is directly and simultaneously correlated to the spatiotemporal variations encountered at columnar tip, local growth, particular geometrical arrangements

and fine details of the columnar dendritic network, complemented with quantification of the local solute pile-up.

4.2. Procedure for Data Analysis²

The experimental procedure for sample preparation and directional solidification along with a description of the X-ray microscopy technique was given in Chapter 2. The present section will focus on the procedure for data analysis of the images obtained in-situ from the studied alloys i.e. Al–30 wt.% and 20 wt.% Cu alloys. The data analysis procedure describes the methodology for analyzing the evolution of the secondary dendrite arm spacing (SDAS) during solidification in order to study local growth and coarsening kinetics. Also, the procedures for image processing and analysis for studying local constitution variations in the liquid during dendrite growth and fragmentation are described.

4.2.1. Secondary dendrite arm spacing (SDAS)

4.2.1.1. SDAS measurements during downward growth on the Al–30 wt.% Cu alloy

During downward columnar dendritic growth of the Al–30 wt.% Cu alloy images were recorded as soon as the solidification front appeared in the field of view (at $t_{exp} = -9.0$ s). Velocity fluctuations were observed during the experiments. The corresponding solidification front velocities were determined

² Experimental data was provided by R.H. Mathiesen (NTNU) within the framework of the NorLight program.

previously for the three primary dendrites trunks observed in the centre of the field of view (Fig. 4.1) [32]. The sequence of images considered, corresponds to deceleration $\sim -4.9 \mu\text{m/s}^2$ and acceleration of the solidification front $\sim 13.7 \mu\text{m/s}^2$. These transient conditions occur naturally during solidification. Mathiesen and Arnberg [32] explained that these fluctuations occurred due to the continuous solute pile-up at the solidification front followed by solute settlement after certain accumulation. High-density solute-rich liquid settles down due to gravity and a cleaner melt enables development of a new boundary layer.

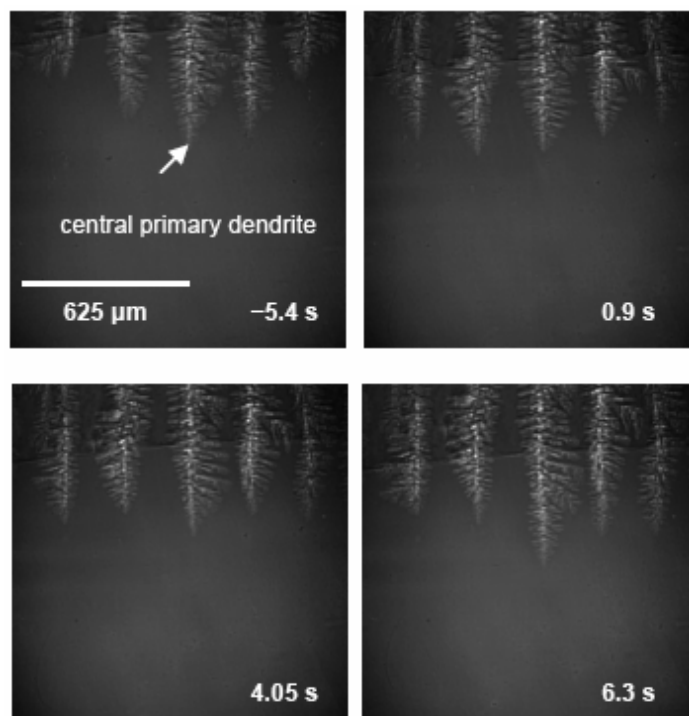


Figure 4.1. Fields of view taken at $t_{\text{exp}} = -5.4, 0.9, 4.05$ and 6.3 s for the Al-30 wt.% Cu alloy solidifying downwards.

A detailed explanation of the current experiment can be found in reference [32]. For other relevant information concerning the experimental set-up and X-ray microscopy the reader may refer to [34] and Chapter 2.

Coarsening of secondary dendrite arms developing during continuous solidification was characterized by measuring the SDAS parallel to the main dendrite trunk at different local solidification times determined according to the depth in the mush. For determining SDAS, branches which were left behind during competitive growth were not considered for the measurements and only the distance between overgrown branches was determined. The average SDAS was then measured over the secondary dendrite arms contained between the limits of the selected region at each image. Also, the measurements were taken at left-hand side and right-hand side of the dendrite trunk and at both growth regimes i.e. during deceleration and acceleration of growth rate.

The local solidification time t_s was determined from [18]:

$$t_s = \frac{a}{v_{sl}}, \quad (4.1)$$

where a corresponds to the depth within the mush and v_{sl} the velocity of the primary dendrite tip. The average local solidification time was estimated for each of the four regions delimited within the mush, taking into consideration the instant velocity of the selected dendrite (central primary dendrite in Fig. 4.1). Error measurements of the average t_s were estimated based on its deviation according to the local solidification times at the boundaries of the region according to a where the SDAS were measured. The measurements provided a

statistical SDAS vs t_S trend. Finally, from the graphs SDAS vs. t_S the coarsening constant n was determined by linear regression.

For the present investigation, the central primary dendrite from the field of view in Fig. 4.1 was studied.

4.2.1.2. SDAS measurements during upward growth on the Al–20 wt.% Cu alloy

The same procedure for obtaining SDAS vs t_S described above was applied for the Al–20 wt.% Cu alloy solidifying upward. As described in paper [5], the experimental time t_{exp} was established for the images acquired taking as $t_{exp} = 0$ the moment when fragmentation begins. The images considered for the current analysis were from -19.35 s to 0 s prior to fragmentation. Dendritic columnar grains develop with fluctuations in growth rate due to solute accumulation at the solidification front. In the present analysis, deceleration followed by minimal fluctuation in growth rate prior to fragmentation was observed. Deceleration of growth rate was estimated to be $\sim -3 \mu\text{m}/\text{s}^2$ from $t_{exp} = -19.35$ s to $t_{exp} = -13.5$ s and then small erratic fluctuations appeared from $t_{exp} = -13.05$ s to $t_{exp} = 0$ s [5]. Coarsening was characterized by measuring the SDAS during solidification. SDAS was determined at the two growth regimes (deceleration and fluctuations in growth rate) and presented as a function of t_S prior to fragmentation.

Three columnar dendrites were considered for the measurements, these were dendrites present in the middle of the field of view (Fig. 4.2). Also, the measurements were taken at the left-hand side and right-hand side of the columnar dendrites (dendrites are numbered from left to right on Fig. 4.2).

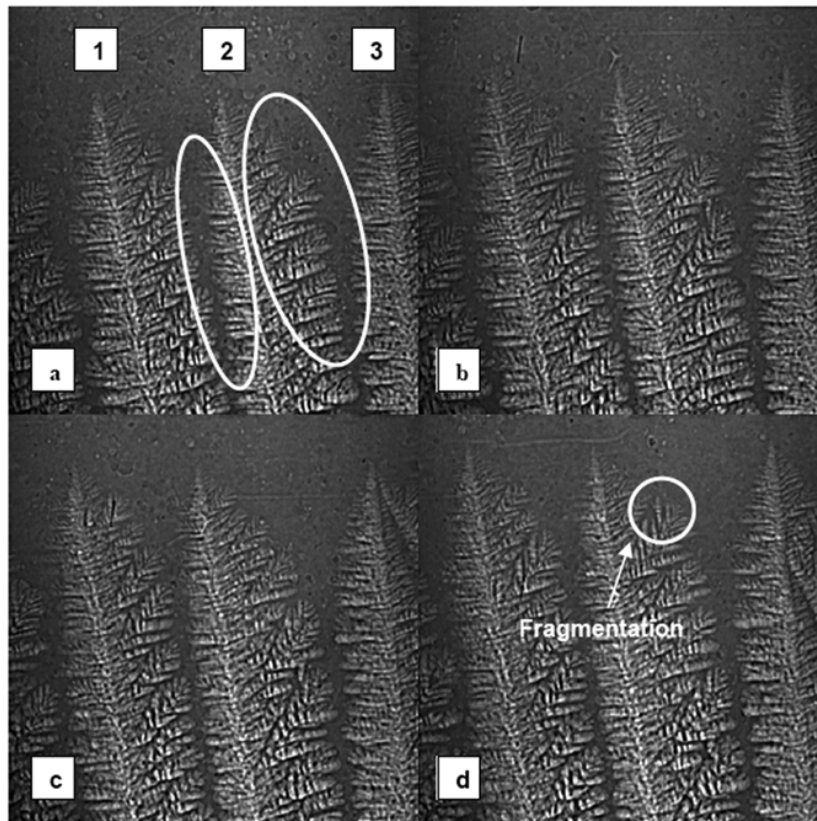


Figure 4.2. Images obtained in-situ at: a) $t_{exp} = -19.35$ s, b) $t_{exp} = -13.5$ s, c) $t_{exp} = -7.65$ s and d) $t_{exp} = 0$ s. The size of the image is $1250 \times 1250 \mu\text{m}$. Columnar dendrites are numbered in (a). Two characteristic liquid channels between columnar dendrites are shown in (a).

4.2.2. Image processing and micro-constitutional analysis in the liquid

For the Al–20 wt.% Cu alloy solidifying upwards, image sequences together with columnar tip velocities from the same solidification experiment have been presented previously in another study on detachment mechanisms at different locations in the solidification range [5], but without the local constitutional analysis presented herein.

From the 2D X-radiographic projection images, regions of interest (ROIs) were selected in the area where a tertiary arm, that eventually fragments, starts to develop. The regional images were processed using the *IDL* (Interactive Data Language) software [36]. As a first step, a binary mask is used to divide the image into sub-regions corresponding to: i) sample volumes containing primary-phase solid, and ii) regions being fully liquid. This allowed for a quantitative assignment of the local liquid concentration in the latter type of regions. The high-solute content alloy chosen for the study together with the coherency characteristics of the synchrotron beam provided enough contrast at the solid-liquid interface to identify solid-containing regions even for branches down to a thickness of 3-4 μm [32, 33]. The liquid composition was determined from the analysis of contrast in the liquid regions of interest relative to a reference region deep inside the bulk liquid, assuming the latter to be at the nominal composition $C_0 = 20 \text{ wt\% Cu}$. Discrimination of separate phase regions from the images also permitted extraction of features like solid-liquid interface coordinates and local propagation velocities [32-35].

4.3. Growth and Coarsening Kinetics during Downward Growth

4.3.1. Growth and coarsening during solidification

Figure 4.3 demonstrates four of the ROIs taken at $t_{exp} = -5.4, 0.9, 4.05$ and 6.3 s from the images shown in Fig. 4.1. Secondary dendrite arm spacing SDAS as a function of the local solidification time t_s is shown in Figure 4.4.

Coarsening and growth occurred simultaneously during solidification. There was a difference in morphology development at the left-hand and right-hand side of the primary dendrite trunk. Therefore, SDAS measurements were performed at the left-hand and right-hand side of the primary dendrite during deceleration and acceleration. Fig. 4.4a shows similar kinetics of gradual spacing development at both sides during deceleration. In this case, the SDAS close to the eutectic front is $\sim 43 \mu\text{m}$ ($t_s = 11 \text{ s}$). It was observed that during deceleration, the coarsening mechanism is thickening of secondary dendrite arms. Also, a moderate growth of tertiary dendrite arms was observed.

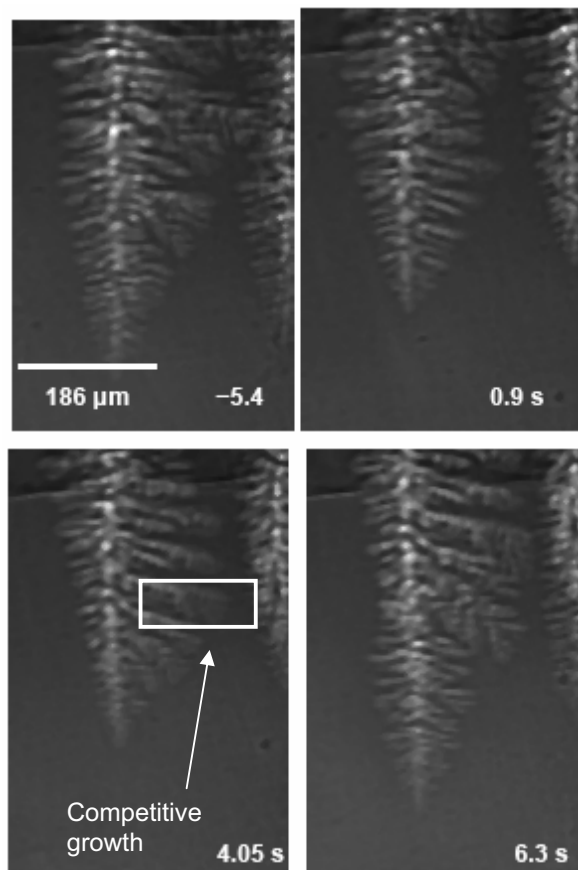


Figure 4.3. Regions of interest ROIs taken around the central primary dendrite at $t_{\text{exp}} = -5.4, 0.9, 4.05$ and 6.3 s .

During acceleration (Fig. 4.4b), the kinetics of the SDAS development differs strongly from one side to another, and from the kinetics found during deceleration. During acceleration, at the left-hand side, at t_s between 2 and 5 s, the slope is moderate, and then a sudden steeper change is shown after 5 s (dotted line in Fig. 4.4b). This abrupt change is due to thickening of branches which are close to the eutectic front.

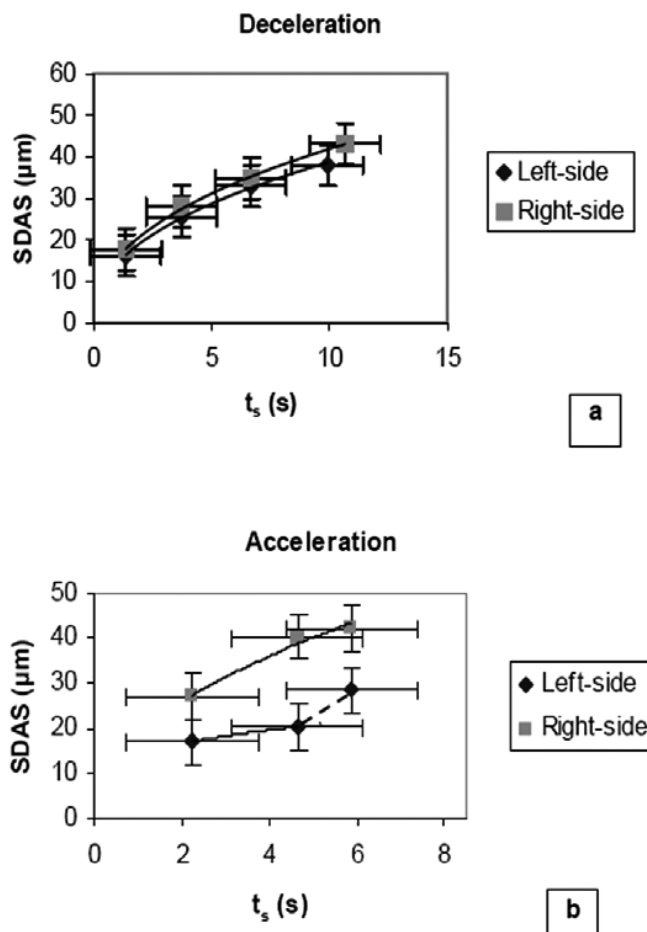


Figure 4.4. Secondary dendrite arm spacing SDAS as a function of solidification time t_s during: (a) deceleration, and (b) acceleration of the solidification front.

In contrast, the right-hand side shows a more prominent growth of tertiary dendrite arms and also the competitive growth of dendrite arms (Fig. 4.3 and 4.5), where some branches are left behind while others continue growing. During the measurements, the SDAS was taken considering the spacing between those branches that overtake in growth other branches. In addition, the SDAS at the right-hand side is larger than the SDAS at the left-hand side and the SDAS during deceleration. Furthermore, during acceleration, both sides demonstrated that some branches coalesce (Fig. 4.5). From the corresponding curves in Fig. 4.4, a correlation between the SDAS and t_s was estimated. Linear regression analysis was used to determine the relationship $SDAS \sim t_s^n$. During deceleration, the $SDAS \sim t_s^{0.4}$ at both sides of the dendrite trunk. On the other hand, during acceleration, the $SDAS \sim t_s^{0.28}$ at the left-hand side of the primary dendrite at t_s between 2 and 5 s, then changes abruptly to $SDAS \sim t_s^{0.4}$. Whereas, the $SDAS \sim t_s^{0.5}$ at the right-hand side during acceleration.

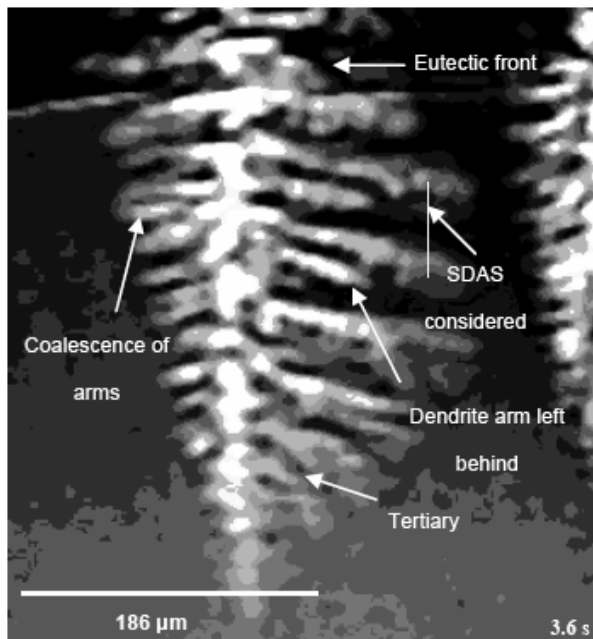


Figure 4.5. Magnification over image taken at $t_{exp} = 3.6$ s which develops during acceleration demonstrating the distinct coarsening mechanisms operating during solidification.

4.3.2. Influence of dendrite arrangement on growth and coarsening kinetics

The average total mush depth, from the tip of the dendrite to the eutectic front, adjusts in length with the velocity of the solidification front. During deceleration, the mush depth diminishes gradually from a starting measured depth of $\sim 440 \mu\text{m}$ ($t_{exp} = -5.4 \text{ s}$). At the end of the deceleration stage ($t_{exp} = 0.9 \text{ s}$), the mush depth is $\sim 335 \mu\text{m}$; then it increases gradually when acceleration starts. During acceleration the mush length adjusts at the end to $\sim 390 \mu\text{m}$ ($t_{exp} = 6.3 \text{ s}$). The equilibrium mush depth according to the equilibrium freezing range ΔT_0 and G_T , can be calculated from: $a_{eq} = \Delta T_0 / G_T$; where $\Delta T_0 = m(C_0 - C_e)$, $m = -4.9 \text{ K/wt\% Cu}$ is the equilibrium liquidus slope obtained from the Al–Cu diagram, C_0 is the nominal composition (30 wt% Cu) and C_e is the eutectic composition (33.1 wt% Cu). The calculated equilibrium depth is $a_{eq} = 560 \mu\text{m}$; compared to the maximum depth observed before deceleration starts ($\sim 440 \mu\text{m}$), $\Delta a = (a_{eq} - a) = 120 \mu\text{m}$, the difference is quite large. This highlights the influence of downward solidification and transient solidification conditions on liquid flow and thus on the microstructure. It should be noted, however, that the mush depth was estimated rather roughly from the length of the primary dendrite and the purpose of such analysis is only to relate its particular development to transient conditions and comparison with a_{eq} . The transient development of neighbouring primary dendrites affects the local mush depth at the left-hand and right-hand side of the central primary dendrite.

The solidification time is affected by the fluctuations in the solidification front velocity in the similar manner as the depth of the mush, where the local solidification time becomes shorter during acceleration than during deceleration. Accordingly, more coarsening should be expected at longer solidification times.

This is evident in Fig. 4.4a, where the SDAS is larger at both sides of the dendrite compared to the left-hand side of the same dendrite during acceleration (Fig. 4.4b). Accordingly, the right-hand side, during acceleration, has a larger SDAS compared to that found during deceleration. During acceleration it is evident that both sides of the dendrite behave differently. It is apparent, from the observations of the sequence of images (Fig. 4.1), that the spacing with neighbouring primary trunks is different. The neighbouring dendrite at the left-hand side is slightly farther away as compared to the neighbouring dendrite at the right-hand side. The distance between dendrite trunks influences liquid flow. During downward growth, solute rejection and flow of solute-rich liquid from the depth of the mush towards the solidification front (settlement) is easier at the left-hand side (more permeable) than at the right-hand side (less permeable) due to spacing between neighbouring dendrites. This may explain the different solidification kinetics at both sides of the central primary dendrite trunk. Deceleration occurs due to solute pile-up at the front. The undercooling required for growth at the solidification front is diminished due to dissipation of solute gradients. Solute-rich liquid accumulates at both sides. After certain saturation, solute-rich liquid settles due to gravity and vacates the mushy region, leaving an unsaturated melt behind as described by Mathiesen and Arnberg [32].

During solute evacuation, a solute gradient again builds up causing acceleration of growth at the front. At the left-hand side (permeable region), a larger evacuation of solute-rich liquid from the mushy zone dissipates solutal gradients and thus diminishes the constitutional undercooling. On the other hand, the mushy zone between the central primary dendrite and right-hand side primary dendrite is less permeable. Thus, during growth and solute rejection, solute-rich liquid gets trapped by the developing dendrite branches. Solute enrichment occurs, promoting a solutal gradient which enables growth. This is why growth of tertiary dendrite arms is largely observed at the right-hand side.

Moreover, coarsening at this region may be enhanced due to solute enrichment. However, growth may be the dominating factor for the increase in the SDAS along with competitive growth. High permeability at the left-hand side of the dendrite enables replacement of a clean melt, which diminishes coarsening and growth. The sudden increase in SDAS (Fig. 4.4b, left-hand side) may be due to solute that was accumulated between large secondary dendrite arms near the eutectic and did not flow. This enrichment near the eutectic causes coarsening of strong dendrite arms due to material transport and deposition caused by local solute gradients.

4.4. Growth and Coarsening Kinetics during Upward Growth: Prior to Dendrite Fragmentation

4.4.1. Growth and coarsening during solidification

Figure 4.2 demonstrates that the first two dendrites develop slightly inclined towards the left-hand side as compared to the third one. It is also clear that the sides of the first two dendrites demonstrate different development of secondary and tertiary dendrite arms. The first two columnar dendrites show at the left-hand side shorter secondary and tertiary dendrite arms than those at the right-hand side. Also, secondary dendrite arms at the right-hand side are not as perpendicular to the main dendrite trunk (having a $\sim 45^\circ$ angle with respect to the main trunk) as compared to those secondary dendrite arms at the left-hand side (which have a $\sim 90^\circ$ angle with respect to the main trunk). The left-hand

side of the third dendrite has secondary dendrite arms developing perpendicular to the main trunk and also secondary and tertiary dendrite arms are shorter than those at the right-hand side of the first two dendrites. Visually from the images, it can be seen that permeability (fluidity through the mush) should be greater between dendrite 2 and 3 than between dendrite 1 and 2. This is due to a difference in dendrite orientation between dendrite 2 and 3 which permits liquid arrival and penetration further down in the mush. Such arrangement between dendrite 2 and 3 can be defined as “grain boundary” [5].

Figures 4.6–4.8 demonstrate SDAS measurements as a function of t_s . The summary of the microstructural observations is presented in Table 4.1. It is evident that the right-hand sides of the two inclined dendrites (1,2) have different microstructural development as compared to their left-sides. At the left-hand side, high-order branches are not as developed as compared to those at the right-hand side, thus n has values between ~ 0.24 and 0.32 which are in concordance with those commonly reported in literature [1, 11, 12, 21, 37-40]. At contrast, the right-hand side has larger n values, $\sim 0.50 - 0.73$. Also, the left-hand side of dendrite 3 has also a relatively large $n \sim 0.42 - 0.49$.

Table 4.1. Summary of microstructure development observations.

Feature	Dendrite 1		Dendrite 2		Dendrite 3	
	Left	Right	Left	Right	Left	Right
Secondary dendrite arms	Yes, at $\sim 90^\circ$	Yes, at $\sim 45^\circ$	Yes, at $\sim 90^\circ$	Yes, at $\sim 45^\circ$	Yes, at $\sim 90^\circ$	–
Tertiary dendrite arms	Yes, small	Yes, large	Yes, small	Yes, large	Yes, small	–
Coarsening exponent n	$\downarrow \sim 0.32$	$\downarrow \sim 0.54$	$\downarrow \sim 0.24$	$\downarrow \sim 0.60$	$\downarrow \sim 0.49$	–
	$\uparrow \downarrow \sim 0.32$	$\uparrow \downarrow \sim 0.50$	$\uparrow \downarrow \sim 0.24$	$\uparrow \downarrow \sim 0.73$	$\uparrow \downarrow \sim 0.42$	

* Arrows mean: \downarrow : during growth deceleration and $\uparrow \downarrow$: during minimal growth fluctuations.

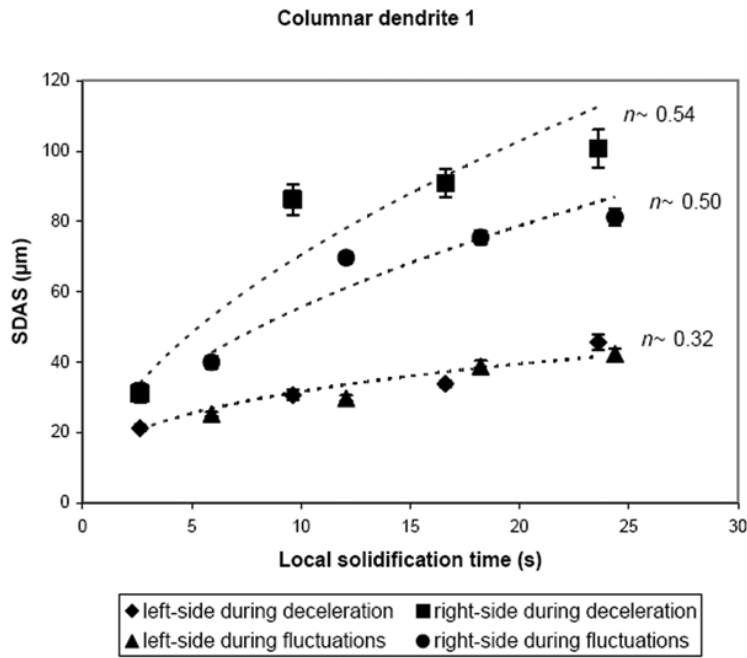


Figure 4.6. SDAS as a function of local solidification time for the columnar dendrite 1 in Fig. 4.2.

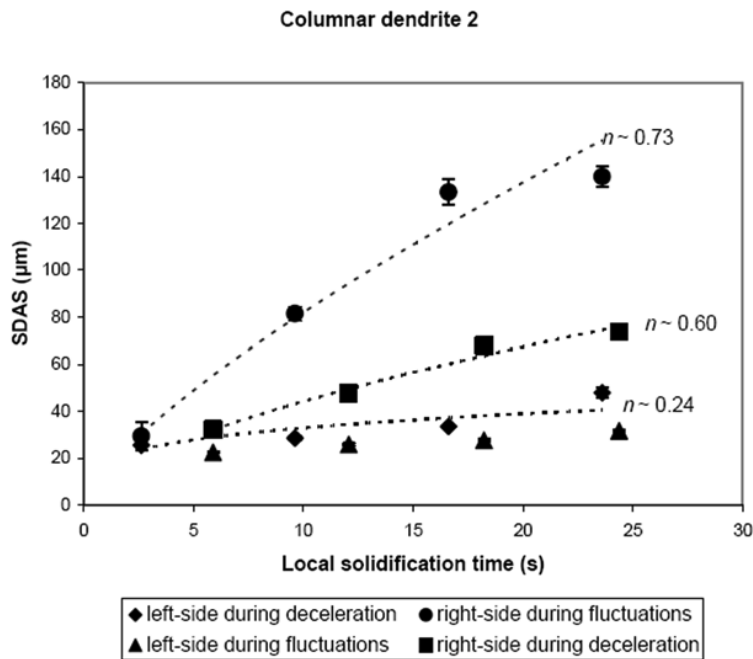


Figure 4.7. SDAS as a function of local solidification time for the columnar dendrite 2 in Fig. 4.2.

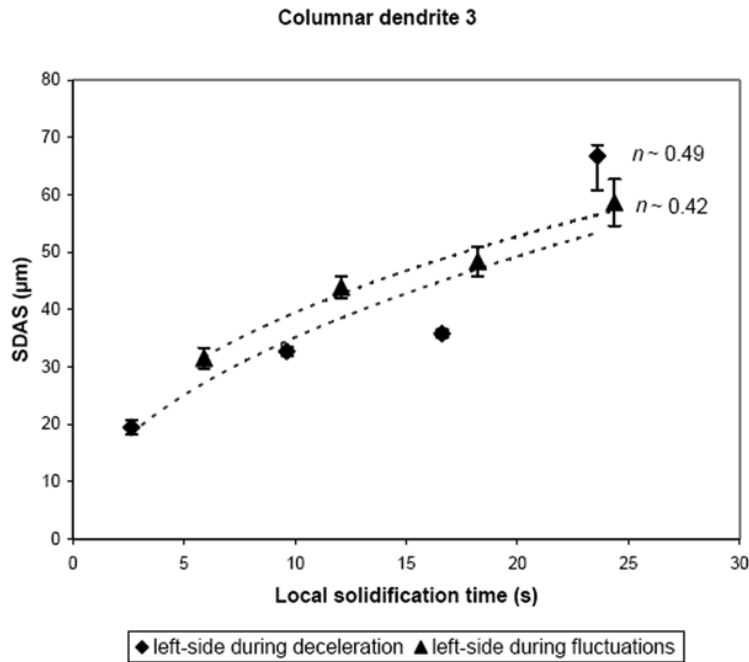


Figure 4.8. SDAS as a function of local solidification time for the columnar dendrite 3 in Fig. 4.2.

4.4.2. Influence of dendrite arrangement on growth and coarsening kinetics

As a result of the geometric arrangement and inclination evident from Fig. 4.2, the right-hand sides of dendrites 1 and 2, close to the dendrite tips, have more contact with the constitutionally undercooled liquid coming from the dendrite tips which promotes growth. Thus, tertiary dendrite arms form close to the dendrite tip and secondary dendrite arms tend to be separated during further development, increasing SDAS. Also, deeper in the mush, some secondary dendrite arms are left behind and stop developing (see Figure 4.9) leading to a further increase in SDAS. Therefore, the main mechanism of increased SDAS in these regions is the growth of tertiary dendrite arms and undergrowth of

secondary dendrite arms (i.e. competitive growth of branches). The left-hand sides, however, do not have as much contact with the undercooled liquid as the right-hand sides. Thus, weaker growth of high-order branches is observed, hence SDAS is smaller.

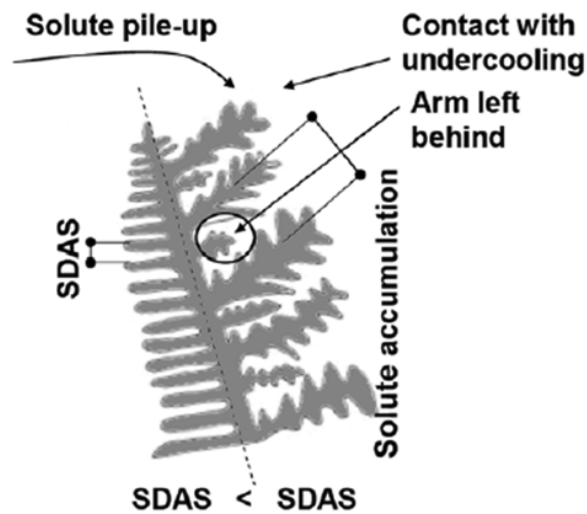


Figure 4.9. Schematic representation showing effect of dendrite arrangement on SDAS during solidification.

According to these observations, pure coarsening kinetics (thickening of arms driven by purely capillarity effects) may be more evident at the left-hand sides of the studied dendrites. The coarsening exponent at the left-hand side of the first dendrite has a value in accordance to the value frequently reported in literature (i.e. ~ 0.3); while the left-hand side of the second dendrite has a much lower value which agrees to those values recently reported for pure coarsening kinetics (i.e. ~ 0.2) [11,12].

On the other hand, at the right-hand sides coarsening becomes overshadowed by high-order branching (growth due to constitutional undercooling) that developed earlier during solidification and by the competitive growth. It has been demonstrated elsewhere [41, 42] that forced and/or natural convection can facilitate material transport and thus coarsening. However, as has been demonstrated earlier [5], due to the experimental conditions of the experiments, there is hardly any thermo-solutal convection that can affect solidification. Thus, these effects are due to the geometrical arrangement of dendrites and exposure of high-order branches to the constitutionally undercooled liquid close to the solidification front. In addition, between dendrites 2 and 3, permeability can be higher and solute tends to be accumulated in this region. These conditions also eventually produce fragmentation, at $t_{exp} \sim 0$ s, due to solute enrichment (demonstrated in Section 4.5). This can also lead to an even further increase in solute gradient and undercooling at the dendrite tip and promote growth at the right-hand side of dendrite 2 ($n \sim 0.73$).

High-order branches at the left-side of dendrite 3 (which is not inclined) have also contact with the undercooled liquid at the dendrite tip but, due to their orientation (i.e. $\sim 90^\circ$ with respect to the main dendrite trunk), the contact of these branches is limited leading to a smaller n (i.e. $\sim 0.42 - 0.49$). This value is in close agreement with Bamberger et al. [43] where n was reported to be ~ 0.43 during unsteady solidification of Al–Si alloys.

The present measurements on SDAS demonstrate how the arrangement of dendrites can influence the development of their structure. Development of high-order branches is affected by their contact with the undercooling at the dendrite tip, which depends on the arrangement of the parent dendrite trunk.

4.5. Dendrite Fragmentation due to Solute Enrichment

4.5.1. In-situ observation of fragmentation

Figure 4.10 shows the location where dendrite fragmentation starts, from images taken in-situ during solidification. Image sequences together with columnar tip velocities from the same solidification experiment have been presented previously in another study on detachment mechanisms at different locations in the solidification range [5], but without the local constitutional analysis presented herein.

At about 20 s prior to the initial detachment a modest deceleration of the columnar front i.e. $-3 \mu\text{m/s}^2$ was observed, and it was assumed that this deceleration could initiate enrichment in solute at the columnar front which due to gravity-driven-flow would settle into the mush, eventually leading to detachment of dendritic arms [5]. The moment of the initial detachment is set as $t=0$ s.



Figure 4.10. In-situ observation of localized fragmentation (in circled region) during the solidification of an Al-20wt % Cu alloy at: (a) $t=0$ s, (b) $t=2.25$ s and (c) $t=4.50$ s.

The results of the constitutional analysis are presented in Figure 4.11 as a sequence of colour contour maps. The liquid around the fragment-to-be, the central tertiary dendrite arm, gets enriched in copper as solidification proceeds. The maximum solute content measured at the tertiary root during enrichment was ~27 wt% Cu. During fragmentation, the neck radius at the root, R_{root} , decreases whereas the radius of the tip, R_{tip} , increases, as illustrated in Figure 4.12a, where R -estimates have been extracted from three adjacent trunk diameters measured at locations as indicated by the schematic drawing in Fig. 4.13. The main source for errors in R_{tip} and R_{root} is the local solid-liquid interface contrast sharpness.

A few seconds after the first fragment develops ($t \sim 3.15$ s) another tertiary dendrite arm detaches from the same secondary dendrite branch. Figure 4.14 illustrates liquid concentration contour maps for the secondary detachment, and evidently this occurs in an environment where solute enrichment has proceeded further than in the case of the first fragment. The morphologies of neighbouring tertiary dendrite arms do not change much during the detachment process, indicating that the fragment-to-be develops almost independently from the others. Figure 4.12b gives the change in radii of the root and tip, quite similar to what was found for the first fragment shown in Fig. 4.12a. The detachment process takes place in about 2.7 s in both cases, from the beginning of necking to the final detachment from the parent dendrite branch.

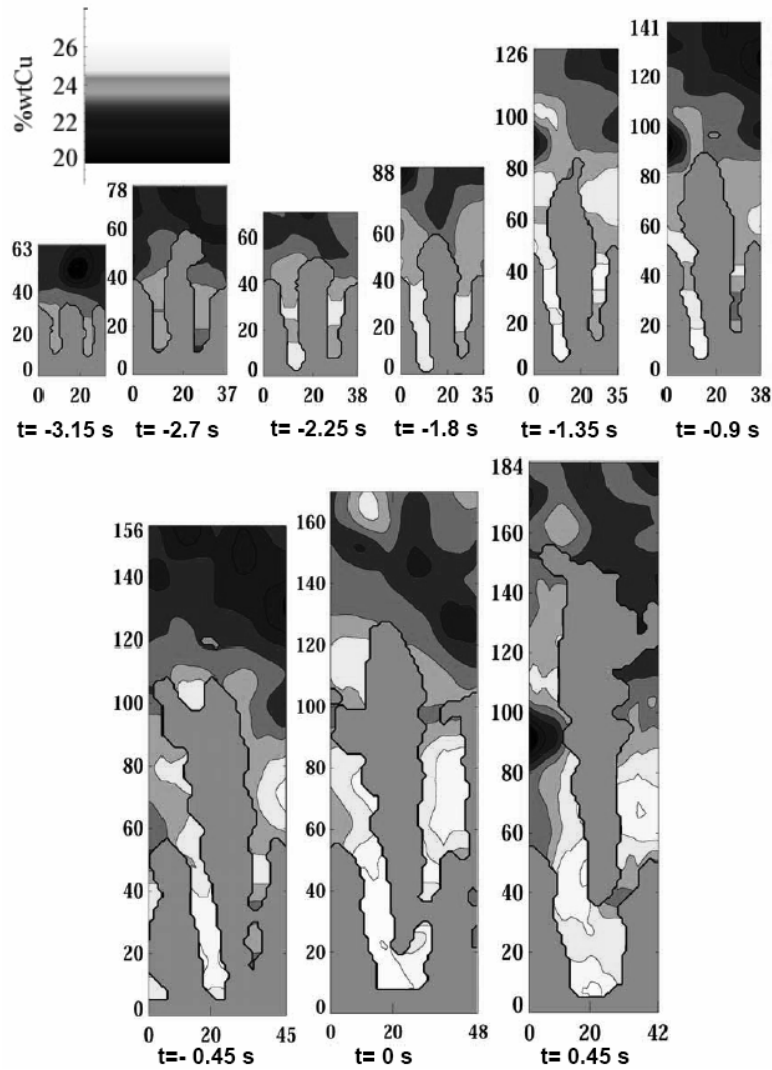
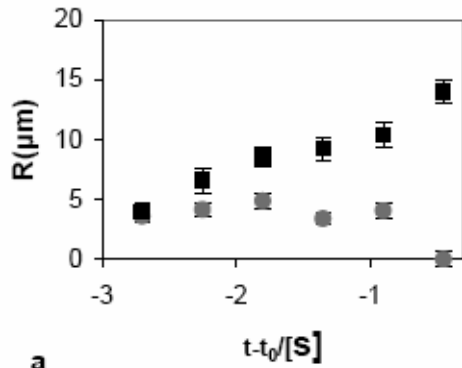
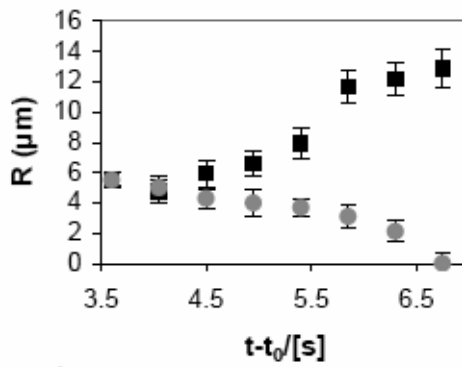


Figure 4.11. Contours showing solute enrichment during the fragmentation of the first tertiary dendrite arm (shown in Fig. 4.10). The wt.% Cu level colouring is indicated explicitly, and the masked-off solid has been coloured in grey. The scale is indicated in microns. For the colour version of this figure see Figure A5 in Appendix.



a



b



Figure 4.12. Radii values for the tertiary root and tip prior to detachment of the first (a) and second fragment (b), respectively.

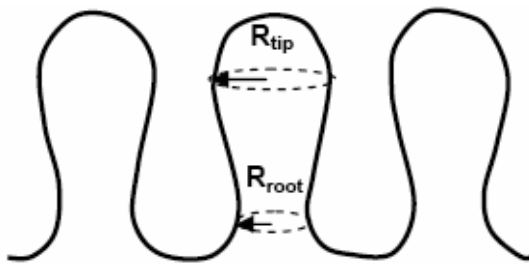


Figure 4.13. Schematic representation of tertiary dendrite arms where solute enrichment and fragmentation occurs, showing the locations of the radii R_{tip} and R_{root} .

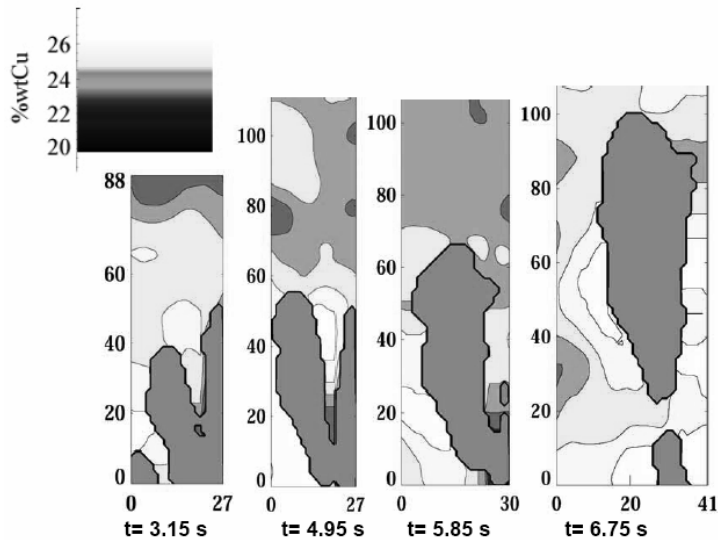


Figure 4.14. Contours showing solute enrichment during the fragmentation of a second tertiary dendrite arm (coloured in grey). The scale is indicated in microns. For the colour version of this figure see Figure A6 in Appendix.

4.5.2. Solute enrichment

As shown in Fig. 4.10, the first two columnar dendrites develop with a different inclination from the third columnar dendrite at the right-hand side which grows almost parallel to the thermal gradient G_T , indicating the presence of a grain boundary. The solute-rich liquid rejected from the columnar front flows down between the columnar dendrites that constitute the grain boundary, as illustrated in Figure 4.15. The orientation mismatch of these primary arms gives rise to dendrite array geometries where the frontal parts of secondary dendrite arms get more exposed to the incoming liquid flow (see Fig. 4.10 and Fig. 4.15) than what is found for the regular intercolumnar neighbour regions. The tertiary arms that form at the verge of the region where the incoming liquid flow arrives after passing the tip of the neighbouring secondary arm above, experience an

enhancement of tip undercooling from the solute-enriched liquid stream passing by. As a consequence the tertiary arm outgrows its neighbouring branches and advances into the incoming liquid stream (see Fig. 4.11). Consequentially, part of the incoming flow is deflected, and some of the enriched solute streams down the tertiary branch and collects in pockets around the attaching root of the arm. Also part of the solute rejected during the accelerated growth of the tertiary dendrite arm tip accumulates in these pockets. Thus the area around the root becomes rapidly enriched in solute as shown in Figures 4.11 and illustrated in Figure 4.16, and a solute-enrichment-driven remelting process at the root is initiated.

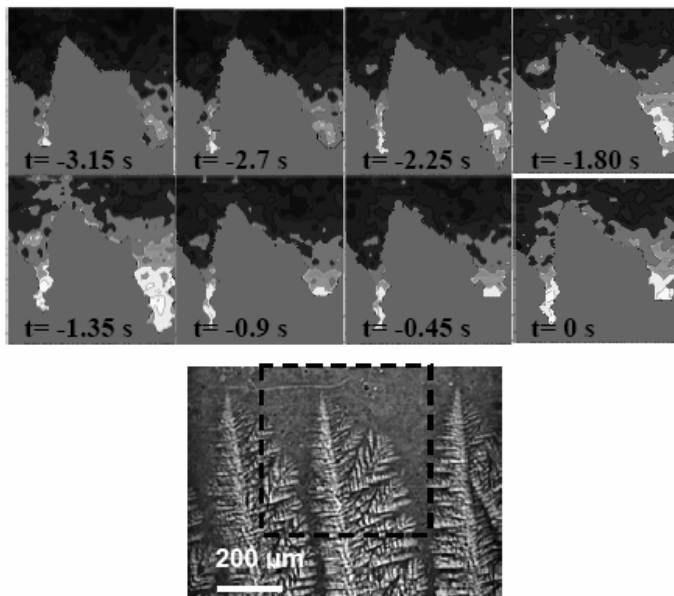


Figure 4.15. Envelops of dendrites (coloured grey) and grey-scale contours showing the solute-rich liquid streaming down from the upper part of the columnar dendrite arm. The image at the bottom indicates the region where the images were taken. For the colour version of this figure see Figure A7 in Appendix.

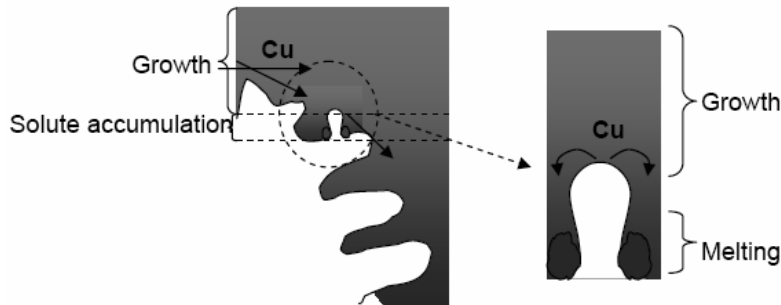


Figure 4.16. Schematic representation of solute enrichment and fragmentation, due to external solute advection and local solute rejection illustrated in dotted circle.

Local remelting at the root of weak dendrite branches is caused by a local depression of the equilibrium melting temperature (i.e. liquidus temperature) due to the increase in solute concentration (i.e. following the liquidus slope line in the Al–Cu phase diagram).

The local region where fragmentation is observed behaves as an open system, where solidification and dendrite network stability depends on changes in the local compositions [44]. In the present case, local growth and network stability are perturbed by the arrival of solute-rich liquid. In addition, it is evident that the local detachment potential is significantly enhanced by the particular network geometry encountered in grain boundary regions. This observation is confirmed by similar observations in several other X-ray imaging sequences on fragmentation [5].

4.5.3. Local solute pile-up and detachment

Local growth velocities, $V(t)$, can be assessed from the spatiotemporal interface coordinates, $r(t)$, as $V(t) = dr(t)/dt + v_{sp}$, with $r(t)$ extracted from image processing [32, 33]. The velocity profile for the central columnar tip, $V_{ct}(t)$, was

made available from previous studies [5]. Therefore all other velocities used here could be calculated relative to this reference and from the relative displacements, $\Delta r(t)$, of interfacial features during the onset of fragmentation as follows:

$$\Delta V(t) = V(t) - V_{ct}(t) = d\Delta r(t)/dt, \quad (4.2)$$

Under the assumption of thermodynamic equilibrium, relative differences in solute concentration between the central primary dendrite tip, and the tip and root of the tertiary dendrite arm that fragments can be calculated from [18]:

$$\Delta C(t) = \frac{\Delta z(t)G_T}{m}, \quad (4.3)$$

where $m = -3.7$ K/wt% Cu is the liquidus slope taken from the Al–Cu equilibrium diagram, and $\Delta z(t)$ is simply the part of $\Delta r(t)$ that is parallel with G_T . Such analysis is shown in Figure 4.17, displaying the solute content around the tertiary dendrite arm tip C_{tt} and root C_{rt} , both relative to the concentration at the columnar front, C_{ct} , and under the assumption that the relation between the concentration and temperature follows the liquidus slope. This calculation indicates that the concentration difference between the tertiary arm tip and the columnar tip is about 1.5-2 wt% Cu. The envelope contour plots in Fig. 4.15 show the difference to be substantially smaller, and since Fig. 4.17 also reveals that $\Delta C_{tt} = C_{tt} - C_{ct}$ increases quite modestly with time, apparently the undercoolings at the tertiary and primary tips are quite similar. In fact this is supported by growth velocity analysis. The average tertiary arm tip velocity over the time interval prior to detachment is earlier found to be $\langle V_{tt}(t) \rangle \sim 32$ $\mu\text{m/s}$, while $\langle V_{ct}(t) \rangle \sim 34$ $\mu\text{m/s}$ [5]. This analysis shows that the solute-rich liquid passing in front of the tertiary dendrite arm promotes local growth.

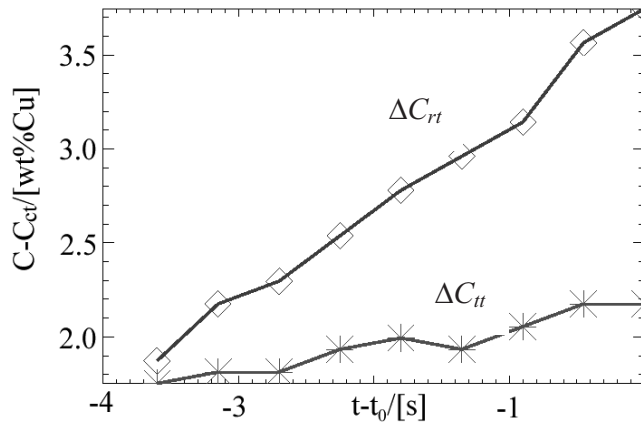


Figure 4.17. Difference in solute content from the main columnar dendrite front (C_{ct}) to the root (C_{rt}) and tip of the tertiary dendrite arm (C_{tt}), i.e. ΔC_{rt} and ΔC_{tt} respectively, during the beginning of fragmentation (considering the first fragment-to-be).

The situation at the root is quite different. The equilibrium calculations given in Fig. 4.17 indicates that the concentration difference between the columnar dendrite tip and the root of the tertiary arm (i.e. ΔC_{rt}) evolves from ~ 2.3 to about 3.7 wt% Cu prior to detachment. This compares reasonably well with the constitution plots of Fig. 4.11, where compositional differences appear to be similar or even higher. Accordingly it seems that a near-equilibrium concentration profile establishes quite rapidly in the liquid pockets between the tertiary branches. The undercooling at the tip of the tertiary arm promotes its growth accompanied by local rejection of solute. At the same time the growth of the root becomes restricted due to the solute transported from the columnar front, the tertiary dendrite arm tip and further local solidification. This solute accumulates in liquid pockets around the tertiary arm root (Fig. 4.11). Further solute supersaturation at the root, due to the openness of the network, initiates remelting of the solid phase in an attempt to re-establish the interfacial

equilibrium, and even at equilibrium conditions some local remelting may be initiated by solvent transport from the root to the tip equivalent to regular coarsening mechanisms described elsewhere [21-23]. In the later stages of remelting, imbalance between the local undercoolings and curvatures will contribute to the final pinch-off.

The errors in $\Delta C_{tt}(t)$ and $\Delta C_{rt}(t)$, as calculated from Eq. 4.3, can be found by a standard error propagation in terms of a second order series expansion. Analysis reveals these errors to be dominated primarily by the systematic deviations introduced by assuming m to be constant over the relevant CT-interval, leaving $(\sigma(\Delta C(t))/\Delta C(t)) \sim \pm 0.05$ and fairly constant. Thus, $\text{Max}(\sigma(\Delta C_{rt}(t))) \sim \pm 0.2\% \text{wtCu}$ arises as $t \rightarrow 0$, where $\text{Max}(\Delta C_{rt}(t)) \sim 3.5 \text{ wt.\% Cu}$. Obviously, these errors can be reduced by applying a non-constant $m(T)$. However, since these errors are small compared to the $1\sigma \sim 0.5 \text{ wt.\% Cu}$ accuracy level in the liquid constitution analysis (as represented by the contour plots in Figs. 4.11, 4.14 and 4.15) which the values in Fig. 4.17 are compared with, a more sophisticated model for the liquidus slope in Eq. 4.3 is not necessary.

4.5.4. Further growth and displacement

Once the first fragment is detached from the secondary branch, it continues growing dendritically while it is transported to the front of the columnar region (Fig. 4.10). This transportation is due to the buoyancy exerted on the fragment which density is only about 70-75% of that of the surrounding liquid [5]. During growth the fragment consumes local solvent from the interdendritic liquid, and consequently the liquid left behind enriches further in solute. This

process leads to a “chain reaction” of further fragmentation down into the intercolumnar region [5]. The second dendrite fragment develops further down into the mush where an environment of solute-rich liquid exists due to further enrichment. This fragment does not experience tip undercooling since solute gradients are, at this stage, lower and the fragment evolves in a solute-rich environment. This last dendrite fragmentation occurrence is just due to remelting caused by the lowering in the equilibrium melting temperature in the solid at the solid-liquid interface of weak dendrite branches due to solute saturation. Also, the latent heat release due to eutectic solidification, close to the eutectic reaction, enhances remelting by increasing the local temperature of the solute-rich liquid between columnar dendrites. The following fragments to develop do not experience dendritic-like growth (or branched growth), since fragmentation occurs due to remelting followed by detachment with no local undercooling which can cause growth of high-order branches [5].

Evidently, incoming interdendritic flow of solute-enriched liquid, due to natural convection and buoyancy forces, affects the dendritic array rather by promoting fragmentation than by increasing the primary dendrite arm spacing, as has been suggested by Apel et al. [45]. The proposed fragmentation mechanism is indeed a much faster way for the dendritic network to adapt to a situation where more solute needs to be accumulated in the mush, as compared to a rather slow process of adjustments of the primary arm spacing. Also, the dendritic arrangement will determine whether coarsening, dissolution of solid or fragmentation occurs or not. The geometry of the dendritic array and accordingly fragmentation should be considered in future microsegregation and growth models. Modelling of such processes is expected to be computationally intensive, since a very fine mesh will be needed to handle capillarity effects properly simultaneously to operating over a volume/area which must be

adequately large to account for several trunks and the fully undercooled region of the mush.

4.6. Concluding Remarks

It is clear that the openness and arrangement of primary columnar dendrites influences liquid flow and thus growth and coarsening kinetics. The interaction of liquid flow with the dendritic arrangement will also depend on the direction of growth. In this case, solute-rich liquid settles down due to gravity and thus either evacuation or accumulation of solute occurs during downward solidification and upward solidification, respectively. Fluctuations in the solidification front velocity occur naturally due to accumulation and settlement of solute-rich liquid during downward solidification and due to accumulation and further enrichment during upward growth.

During downward growth it was found that during deceleration, the SDAS increases gradually as $SDAS \sim t_s^{0.4}$. In current observations, the proximity of neighbouring dendrites (or primary dendrite arm spacing) has no effect on the SDAS during deceleration. In contrast, during acceleration the dendritic arrangement affects coarsening and growth kinetics. In this case, it was found that secondary dendrite arms coarsen more and develop tertiary dendrite arms when primary trunks are close to each other (less permeable region). This is probably due to solute accumulation which causes coarsening, and the build-up of solute gradients that promote the necessary undercooling for growth of high-order branches. Under these conditions it was found that the $SDAS \sim t_s^{0.5}$. In contrast, a more permeable region enables drainage of solute-rich liquid diminishing solute accumulation and thus coarsening. Also, dissipation of

solute gradients in this region diminishes undercooling, thus lowering growth. Liquid flow and dendritic arrangement affect the solidification process by altering the local undercooling within the mush and therefore the local growth dynamics.

During upward growth, coarsening of secondary dendrite branches is more purely reflected in regions which are in less contact with the undercooling at the solidification front. The coarsening kinetics within those regions is in concordance with literature. Quite the opposite effect occurs in regions exposed to the constitutionally undercooled liquid ahead of the dendrite tips which promotes growth of tertiary dendrite arms; which along with undergrowth of secondary arms, facilitates separation between secondary dendrite arms thus increasing the coarsening exponent to values higher than those reported in literature. These conditions would not reflect purely coarsening kinetics since coarsening is overshadowed by overgrowth of high-order branches that leads to the increase in SDAS. Regions where SDAS becomes even higher than values reported in literature ($n \sim 0.73$) are places prone to perturbations in local constitutional undercoolings which may lead to dendrite fragmentation as demonstrated here. In this case, what appears to be a “grain boundary” is a region with potential to have fragmentation of high-order branches.

Furthermore, this work has demonstrated how quantitative and qualitative information can be obtained by in-situ X-ray videomicroscopy and subsequent image processing and used to address important phenomena in solidification science. Fragmentation was studied in an Al-20 wt% Cu alloy during non-forced-convection conditions under directional solidification anti-parallel with gravity.

It was found that local fragmentation can be initiated by transient growth conditions, occurring naturally during solidification, where solute is transported into the mush by gravity-induced liquid flow. Solute-driven fragmentation is particularly favoured at grain boundaries where the openness of the dendrite network causes certain tertiary dendrite arms to be more exposed to the incoming solute-rich liquid flow. Tertiary arms in particular geometric locations may experience sudden increase in flow-induced tip undercooling, accelerating tip growth and local solute rejection. At the same time these tertiary arms may be subjected to accumulation of solute in pockets surrounding its attaching root, both by solute rejected locally, and by a partial deflection of the incoming flow by the advancement of the tertiary tip into the incoming stream. The accumulation of solute at the root of high order branches facilitates remelting by lowering the melting point of the solid-liquid interface.

It was observed that the initial fragment grows in a dendritic manner consuming most of the intercolumnar undercooling while being transported to the columnar front by buoyancy, leaving behind a solute rich liquid that settles further into the mush. In consequence, a cascade of new fragments is released in the wake of the first one. Accordingly, this mechanism can be potent for initiating CET during the solidification of microstructures in less confined systems, e.g. as in 3D-solidified castings.

References

- [1] T.Z. Kattamis, M.C. Flemings, *Trans. Metall. Soc. AIME* 233 (1965) 992.
- [2] J.E. Spinelli, M.D. Peres, A. Garcia, *J. Alloys and Compounds* 403 (2005) 228.
- [3] R.N. Grugel, *J. Mater. Sci.* 28 (1993) 677.
- [4] N. Tunca, R.W. Smith, *J. Mater. Sci.* 23 (1998) 111.
- [5] R.H. Mathiesen, L. Arnberg, P. Bleuet, A. Somogyi, *Metall. Mater. Trans. A* 37A (2006) 2515.
- [6] M.H. Burden, J.D. Hunt, *Met. Sci.* (1976) 156.
- [7] Q. Li, C. Beckermann, *Acta Mater.* 47 (1999) 2345.
- [8] E. Brener, D. Temkin, *Phys. Rev.* E51 (1995) 351.
- [9] B Li, H.D. Brody and A. Kazimirov, *Metall. Mater. Trans. A* 37A (2006) 1039.
- [10] B Li, H.D. Brody and A. Kazimirov, *Metall. Mater. Trans. A* 38A (2007) 599.
- [11] N. Limodin, L. Salvo, M. Suéry, M. DiMichiel, *Acta Mater.* 55 (2007) 3177.
- [12] S. Zabler, A. Rueda, A. Rack, H. Riesemeier, P. Zaslansky, I. Manke, F. Garcia-Moreno, J. Banhart, *Acta Mater.* 55 (2007) 5045.
- [13] A. M. Mullis, R. F. Cochrane, *J. Appl. Phys.* 82 (1997) 3783.
- [14] M. Shwarz, A. Karma, K. Eckler, D. M. Herlach, *Phys. Rev. Lett.* 73 (1994) 1380.
- [15] S. C. Flood, J. D. Hunt, *ASM Metals Handbook, Casting* 15 (1990) 130.
- [16] M. A. Martorano, C. Beckerman, Ch.-A. Gandin, *Metall. Mater. Trans. A* 34A (2003) 1657.
- [17] M.C. Flemings, *Solidification Processing*, McGraw-Hill, New York, 1974.

- [18] W. Kurz, D.J. Fisher, Fundamentals of Solidification, 3rd ed. Trans. Tech. Publications, Aedermannsdorf, Switzerland, 1992.
- [19] B. Billia, N. Bergeon, H. N. Thi, H. Jamagotchian, J. Gastaldi, G. Grange, Phys. Rev. Lett. 93, Art. No. 126105 (2004).
- [20] J. Pilling, A. Hellawell, Metall. Mater. Trans. A 2A (1996) 229.
- [21] T.Z. Kattamis, J.C. Coughlin, M.C. Flemings, Trans. TMS_AIME 239 (1967) 1504.
- [22] A.A. Chernov, Kristallografiya 1 (1956) 583.
- [23] M.O. Klia, Kristallografiya 65 (1956) 576.
- [24] A. Papapetrou, Z. Kristall. 92 (1935) 251.
- [25] K. Jackson, J. Hunt, D. Uhlmann, T. Seward, Trans. AIME, 236 (1966) 149.
- [26] A. Hellawell, S. Liu, S. Z. Lu, J. Minerals Metals Mater. 49 (1997) 18.
- [27] S. Liu, S.-Z. Lu, A. Hellawell, J. Cryst. Growth 234 (2002) 740.
- [28] H. Yasuda, I. Ohnaka, K. Kawasaki, A. Sugiyama, T. Ohmichi, J. Iwane, K. Umetani, J. Cryst. Growth 262 (2004) 645.
- [29] Q. Han, A. Hellawell, Metall. Mater. Trans. B 38B (1997) 169.
- [30] J. Hutt, D. StJohn, Int. J. Cast Metals Res. 11 (1998) 13.
- [31] B. Li, H. D. Brody, A. Kazimorov, Phys. Rev. 70E (2004).
- [32] R. H. Mathiesen, L. Arnberg, Adv. X-ray Anal. 49 (2006) 37.
- [33] R. H. Mathiesen, L. Arnberg, Acta Mater. 53 (2005) 947.
- [34] R. Mathiesen, L. Arnberg, K. Ramsøskar, T. Weitkamp, Ch. Rau, A. Snigirev, Metall. Mater. Trans. B 33B (2002) 613.
- [35] L. Arnberg, R. H. Mathiesen, Proceedings of the 9th International Conference on Aluminium Alloys, Materials Forum 28 (2004) 47.
- [36] Interactive Data Language Software (IDL), Version 6.0 (2003).
- [37] T.F. Bower, H.D. Brody, M.C. Flemings, Trans. TMS-AIME, 236 (1966) 624.

Chapter 4 – Microstructure Development during Constrained Solidification Conditions

- [38] K.P. Young, D.H. Kirkwood, *Metall. Trans. A* 6A (1975) 197.
- [39] Y.L. Liu, S.B. Kang, *Mater. Sci. Technol.* 13 (1997) 331.
- [40] V. Rontó, A. Roósz, *Int. J. Cast Metals Res.* 13 (2001) 337.
- [41] A.N. Turchin, D.G. Eskin, L. Katgerman, *Metall. Mater. Trans. A* 38A (2007) 1317.
- [42] L. Ratke, W.K. Thieringer, *Acta Metall.* 33 (1985) 1793.
- [43] M. Bamberger, I. Minkoff, M.M. Stupel, *J. Mater. Sci.* 21 (1986) 2781.
- [44] S. A. Cefalu, M. J. M. Krane, *Mater. Sci. Eng. A* 359A (2003) 91.
- [45] M. Apel, H-J. Diepers, I. Steinbach, *Model Cast. Weld. Adv. Sol. Proc. XI*, TMS, Warrandale (2006) 505.

Chapter 5

Influence of Microstructure Development on the Structure Formation¹

Chapter 5 summarizes studies that demonstrate how the microstructure evolution eventually determines the final structure. It demonstrates how coarsening and dendrite fragmentation influence the formation of non-equilibrium eutectics and duplex structures respectively. By studying samples solidified at different cooling rates, the coarsening effect on the amount of non-equilibrium eutectics is demonstrated. The study about the formation of duplex structures is based on 3D reconstructed microstructures and on the analysis of solute distribution. The appreciation of structures in 3D is shown to be important for accurate description of the morphology of solidifying structures and its relation to the solidification process.

¹ Chapter 5 is based on publications: 7, 13 (see publications on pages 199, 200).

5.1. Introduction

5.1.1. Coarsening and non-equilibrium eutectics

The final structure of a solidifying alloy is determined by the evolution of the microstructure as described in Chapter 1. In the case of DC casting, the structure development and cast defect formation will depend on the parameters of solidification process and on the phenomena (such as coarsening and fragmentation) accompanying the structure formation.

The influence of cooling rate on the structure formation has not been fully clarified, especially at intermediate cooling rates. The relationship between secondary dendrite arm spacing (SDAS) and cooling rate has been extensively reported in literature [1,8], however the results vary as shown in Table 5.1. The parameters considered to relate coarsening with the SDAS are: the alloy-dependent parameter A and the coarsening exponent n (as described in Eq. 1.5 in Chapter 1).

Despite the well documented values on the exponents A and n , discrepancies in numbers have been reported and usually vary according to composition and cooling rate (Table 5.1). Some studies have demonstrated a decrease in primary and secondary dendrite arm spacing when increasing solute elements such as Mg [9], Mg and Si [10] and Cu and Si [11], while others have reported no influence of composition on dendrite arm spacing [12]. Alloying levels below the limit solubility affect the grain size, having finer grains corresponding to higher concentration of alloying elements [13,14].

The most controversial values reported in literature concern to the influence of cooling rate on the eutectic fraction. The amount of solidifying non-equilibrium eutectics influences hot tearing sensitivity [15]. Table 5.2 demonstrates discrepancies in describing the influence of cooling rate on non-equilibrium eutectics. Flemings [1], based on his microsegregation model, showed that the cooling rate has little effect on the amount of non-equilibrium eutectics. Novikov and Zolotarevskii [25] described that the ratio between the rate of refinement of dendrite arm spacing and the rate of narrowing the periphery zone of dendrite arms enriched in solute influences the effect of cooling rate on non-equilibrium eutectics. Also, they described the influence of homogenization during cooling after solidification. Existing solidification models take into account the back diffusion, homogenization and limited diffusion in the solid e.g. [16]. However, a precise and agreeable explanation about the influence of cooling rate on the formation of non-equilibrium eutectics during solidification has not yet been given. Furthermore, the influence of cooling rate on structure development in the practically important range from 0.1 to 20 K/s is still unclear. It is of great importance to understand the influence of cooling rate within this range on structure development during solidification, since most casting processes operate inside this window (without considering rapid solidification processes).

This chapter demonstrates the influence of cooling rate on coarsening, and eventually the effect of both on the formation of non-equilibrium eutectics. Also, the effect of solute element Cu in Al–Cu alloys on coarsening and non-equilibrium eutectics is illustrated.

Table 5.1. Parameters in Eq. (1.5) for different aluminum alloys.

Alloy composition, wt. %	A	n	Ref.
2.4Cu	1.2–5.9	0.23–0.38	[2]
4.4Cu	2.6–5.0	0.23–0.37	[2]
10Cu	1.1–3.2	0.25–0.39	[2]
4.9Cu	46.6	0.29	[3]
7.12Mg	1578	0.325	[9]
11.07Mg	1313	0.325	[9]
1.2Mn, 1.0Mg grain refined	39.63	0.38	[4]
1.2Mn, 1.0Mg not grain refined	48.9	0.43	[4]
0.33Fe, 0.11Si	22.1	0.39	[5]
0.7Mg, 0.4Si (6063)	166	0.34	[6]
0.8Mg, 0.7Si (6201)	22.1	0.39	[7]
1.24Mg, 0.45Si	73.4	0.202	[10]
1.55Mg, 0.37Si	58	0.253	[10]
0.63Mg, 1.38Si	68.6	0.228	[10]
1.0Mg, 4.47Si	58.2	0.194	[10]
0.99Cu, 0.3Si	79.61	0.316	[11]
0.9Cu, 1.4Si	68.37	0.303	[11]
3.7Cu, 0.5Si	69.31	0.189	[11]
3.95Cu, 0.95Si	69.66	0.202	[11]
2.4Cu, 0.75Si	69.26	0.253	[11]
2Cu, 4.8Si	54.71	0.253	[11]

Table 5.2. Literature on data on the effect of cooling rate on the amount of non-equilibrium eutectics.

Alloy composition, wt%	Cooling rate range, K/s	Variation in the amount of non-equilibrium eutectics with cooling rate	Comments ^a	Ref.
2Cu; 3Cu; 4Cu; 4.8Cu	0.01; 0.8; 5; 50	Increase	RT	[18]
1Cu; 3Cu; 4.5Cu	1–38	Increase	End-chill casting	[19]
2.8Cu; 4.9Cu; 1Si	0.1–37000	Increase to 190 K/s, then decrease	Directional solidification	[3]
2Cu; 5Cu; 6Mg; 1.4Mn; alloy 2024	0.001–4	Initial increase to 0.002–1 K/s followed by decrease	Q	[25]
5Cu	1; 3	Increase	Calculated	[16]
7Mg; 11Mg	0.5–10000	Increase	RT	[9]
5Mg (alloy 5182)	0.5–2	Decrease ^b	RT	[20]
7.5Si– 0.45Mg (alloy 356)	0.25–1.5	Increase ^b	RT	[21]
0.94Mg– 4.11Cu	1.3–21.3	Initial increase followed by decrease	Q	[22]
0.87Mg– 5.07Cu	0.9–18.7	Increase	Q	[22]
Al–Cu–Mg (alloy 2024); Al–Mn–Mg (alloy 3004)	0.05–8.5	Decrease	Directionally solidified ingots	[23]
Steel (1.25C, 1.06Si, 6.6Mn, 1.06Al etc.)	Growth rate during directional solidification 7–450 μm/s	Initial increase followed by slight decrease	Q	[24]

^a RT means that the cooling was not interrupted to the room temperature and Q means that the alloy was quenched after the end of solidification.

^b Estimated from the fraction of solid at which the eutectic reaction starts.

5.1.2. Formation of duplex structures during casting

The influence of structure development during DC casting within the billet sump on the formation of cast defects has not been accurately clarified. In the case of duplex structures, which are related to macrosegregation (see Chapter1), the origins of so-called “floating grains” (i.e. grains assumed to form within the sump that freely move due to thermo-solutal convection) has not been studied experimentally. Since, until now, it is impossible to observe in-situ the structure development of cast billets, the formation of floating grains has not been accurately described. It is important to understand the nature of floating grains as they can affect the evolution of the entire structure.

Thermo-solutal convection acts clockwise within the sump, dragging to the centre of a billet not only floating grains but also solute-rich liquid which can affect local solidification conditions. This progressive event occurs within the slurry region and will eventually affect the developing coherent structure in the mushy region. Controversy over the influence of floating grains on segregation is still an issue, just as the disagreement on the influence of the cooling rate on the formation of non-equilibrium eutectics.

Coarse-cell floating dendritic grains have been reported to be solute-poor [26], however, as suggested by Chu and Jacoby [27], fine-cell and not coarse-cell grains are solute-poor and they are to be considered as the floating grains. Moreover, other microstructural features, such as solute depleted fragments, have been suggested to be contained within a duplex structure [28]. Furthermore, the true influence of grain refining on the structure formation and solute distributions has not been experimentally studied.

Here (in Chapter 5) we present, based on solute distribution measurements and 3D reconstruction of the microstructure, the structural differences between the features found in a duplex grain structure. Based on these observations we suggest the possible formation path for the distinctive structure features.

5.2. Procedures for Data Analysis

Here we present the analysis procedures for studying the samples described in Chapter 2 in Section 2.4. These correspond to the studies on non-equilibrium eutectics (Section 5.3) and formation of duplex structures (Section 5.4).

5.2.1. Grain size and non-equilibrium eutectics

For the microstructure analysis, the samples were cut, ground and polished. Optical image analysis consisted of measurements of grain size, SDAS and fraction of non-equilibrium eutectic. A water solution consisting of 3% HBF₄ was employed to reveal the grain size by oxidizing the surface. The grain structure was studied under cross-polarized light after anodizing the samples. The linear intercept method was used for determining: grain size, SDAS and fraction of non-equilibrium eutectic. Finally statistical analysis was performed on the results.

5.2.2. Analysis of duplex grain structures

The grain morphology such as coarse-cell grains (floating grains), fine-cell grains and less-developed grains were revealed after etching the surface of the samples with 2% NaOH solution with a 5% HNO₃ cleaning agent. The samples

for studying the duplex structure in Section 5.4 were taken from the centre of the billet (i.e. intersection between the billet vertical axis and the billet diameter). The size of the samples was 20×20 mm in cross-section.

5.2.2.1 Serial sectioning and 3D reconstruction

The serial sectioning followed by 3D serial image lapping and rendering technique was used to reconstruct two portions of the structure. Two representative portions of the microstructure were selected, one having mainly coarse-cell grains and other one having fine-cell grains and less-developed grains (possibly fragments found in these studies), and partially reconstructed in order to obtain the 3D morphology of such features (coarse-cell and fine-cell grains, and less-developed grains) in the microstructure. In addition, a portion having coarse-cell and finer-cell grains was completely reconstructed as a 3D volume.

The regions to be reconstructed were first marked with a Vickers microhardness test machine. Consecutively the depth between images (or section thickness) in the z direction was possible to measure after grinding and polishing, also the indent enabled to identify the same regions to be reconstructed during image acquisition.

Serial grinding, polishing and surface etching was the procedure employed to obtain the images. An automatic grinding-polishing machine allowed us to reproduce a depth step of $\sim 3 \pm 0.13$ μm . This depth was enough to enable 3D mesh reconstruction and rendering according to the microstructure length-scale. Figure 5.1 demonstrates the region selected for the 3D volume reconstruction. It was difficult to reproduce the same etching quality from section to section, thus

some finer details, such as narrow spacing between dendritic arms (or cell), may be lost in some images. Still, it was possible to reproduce the overall 3D morphology of the features present within the structure.

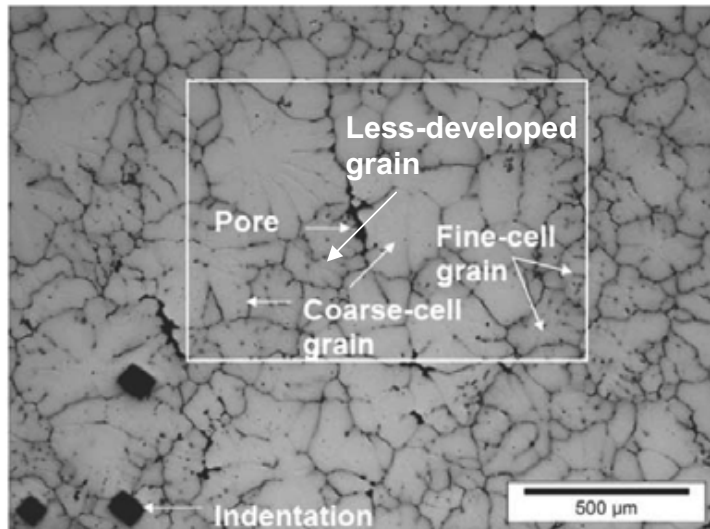


Figure 5.1. Image showing the region selected for 3D volume reconstruction.

The Reconstruct software [29] was used for image alignment, selection of features and 3D mesh rendering (as mentioned in Chapter 2). During image alignment, the region to be reconstructed became smaller due to image fitting and further displacement of images. The volume reconstructed measured $x = 1208 \mu\text{m}$, $y = 897.5 \mu\text{m}$, and $z = 274.5 \mu\text{m}$. The features within the microstructure were selected by tracing manually the boundaries of each grain during image alternation. Finally, 3D visualization was done by using a Boissonnant surface from Reconstruct [29].

5.2.2.2. 3D quantitative measurements

The surface-to-volume ratio or specific surface S_V was obtained for the different features found in the 3D-reconstructed microstructure. Several grains of the

same type were considered, i.e. 3 coarse-cell grains, 5 fine-cell grains and 7 less-developed grains; and the average values are reported. S_V was determined from:

$$S_V = \frac{A_S}{V}, \quad (5.1)$$

where A_S is the surface area of the 3D reconstructed feature and V is the internal volume of the respective feature. The surface area and internal volume were determined in the Reconstruct software [29]:

$$A_S = \sum_{\text{all sections}} L \times l, \quad (5.2)$$

where L is the length of the trace that delimits the feature boundaries and l is the section thickness. The internal volume V was determined from:

$$V = \sum_{\text{all sections}} A_i \times l, \quad (5.3)$$

where A_i is the internal area of the delimited feature and l is the section thickness.

Also the 3D S_V measurements were compared with 2D S_V measurements performed for individual cross-sections in the z direction of the features. The S_V from 2D cross-sections was measured by considering the length L of the delimiting line of the feature divided by the internal area A_i of the feature:

$$S_V = \frac{L}{A_i}, \quad (5.4)$$

Moreover, 2D S_V was estimated again by considering the spherical aberration factor k which is a morphology factor based on the sphericity of the feature defined by [30]:

$$k = \frac{L}{2\pi R}, \quad (5.5)$$

where L is the length of the delimiting line obtained from cross-section images that have the largest size of the features, and R is the radius of a perfect circle which has the same area as the one occupied by the delimited feature. A value of $k > 1$ means that the feature deviates from a perfect sphere.

Then again S_V was determined considering k -correction as [30]:

$$S_V = 3k \frac{1}{R} \quad (5.6)$$

5.2.2.3. Microsegregation measurements

The distribution of solute elements such as Mg, Cu, Zn and Ti was measured in a JEOL JXA 8900R microprobe using an electron beam with energy of 15 KeV and beam current of 100 nA employing Wavelength Dispersive Spectrometry (WDS). The distribution of solute elements was determined within the different morphologies found (i.e. coarse-cell grains, fine-cell grains and less-developed grains or fragments). The measurements were done every 2 μm along the

scanned line with an accuracy of: ± 0.1 wt.% Zn; ± 0.2 wt.% Cu; ± 0.02 wt.% Mg and ± 0.002 wt.% Ti.

The compositions of the areas occupied by the morphological features were estimated by integrating the area under the scanned concentration profiles and then normalizing it to the length of the line scan. Areas having large eutectic-rich zones were avoided to minimize the error when obtaining the measurements. The average composition was considered within the grain envelopes, i.e. considering also the composition within the cells, since these areas also reflect the microsegregation within the grains.

Thermocalc was used to estimate the solidification path of the alloy and to determine the interface concentration during solidification. The equilibrium lever rule was employed to determine the interfacial concentration of the alloying elements in the solidifying Al-phase at different temperatures within the transition region of the alloy. Assuming limited diffusivity of solute in the solid and local equilibrium at the solid-liquid interface (lever rule-type solidification); the calculated solute amount was considered as the minimum solute concentration in the centre of the dendrite cell. Following this calculation, the Gulliver–Scheil non-equilibrium solidification model was used to estimate the solidification path i.e. solid fraction as a function of temperature. Finally, the minimum solute concentration measured in the line scans, within the dendrite cells, was considered as the corresponding interfacial equilibrium composition and correlated to the corresponding solidification path. This correlation was used to determine the solid fraction at which the certain grain-cell-type was formed.

5.3. Influence of Coarsening on Non-equilibrium Eutectics

5.3.1. Dendrite arm spacing and grain size

The average SDAS and grain size diminish (i.e. the structure becomes refined) when the cooling rate and Cu concentration are increased. Figure 5.2 demonstrates the typical structures observed when varying cooling rate and Cu concentration.

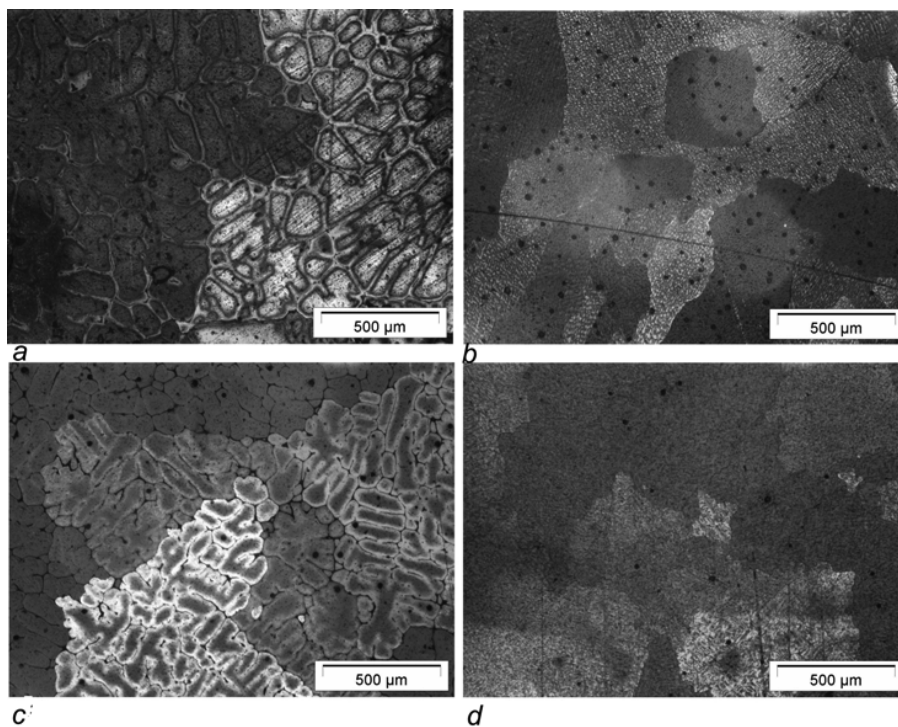


Figure 5.2. Microstructures of the alloys: (a) Al–0.98 wt.% Cu cooled at 0.3 K/s; (b) Al–0.98 wt.% Cu at 13.6 K/s; (c) Al–4.3 wt.% Cu at 0.2 K/s; and (d) Al–4.3 wt.% Cu at 9.1 K/s. The influence of cooling rate on structure can be compared between: (a) – (b), and (c) – (d), and the influence of composition on structure between (a) – (c).

The influence of cooling rate on the structure is also demonstrated based on SDAS measurements as a function of the measured total cooling rate in Figure 5.3a. The influence of the cooling rate measurement methods (linear and total cooling rates) with the SDAS relationship was compared. Table 5.3 demonstrates these comparisons based on the coefficients (from Eq. 1.5) obtained by linear regression analysis. The coefficients obtained when using the linear cooling rate showed to be higher than those values obtained with the total cooling rate. Also, Table 5.3 shows values obtained for the coefficient A when using a fixed n value of 0.33 and with the adjustment of A and n which showed the best statistical correlation (best R^2 values). In addition, the influence of Cu concentration on the coefficients is demonstrated in Figure 5.3b. The so-called “composition sensitive coefficient”, A , decreases with increasing the Cu concentration in the alloy. In contrast, n values turned out to be less sensitive to the composition.

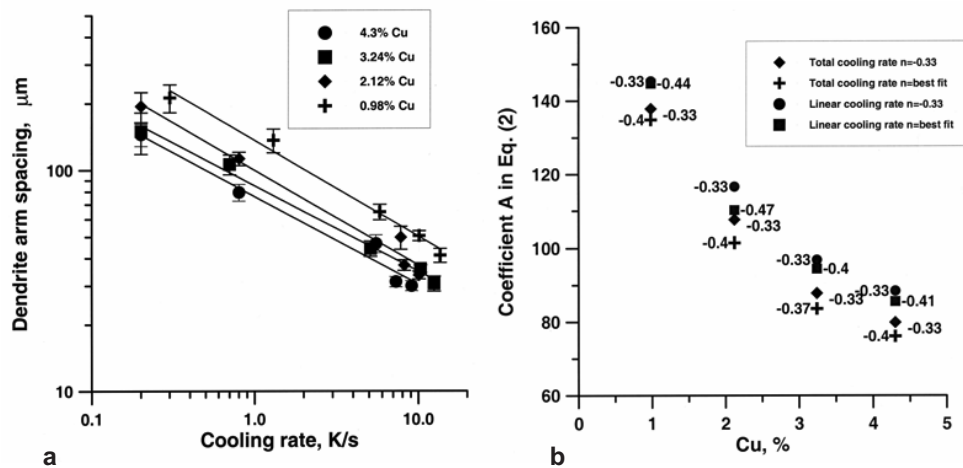


Figure 5.3. (a) Effect of cooling rate and Cu concentration on the SDAS and (b) effect of Cu on the coefficients A (Y-axis) and n (values indicated on the plot) from Eq. 1.5.

Table 5.3. Coefficients in Eq. 1.5 obtained from linear regression analysis on experimental data about SDAS for Al–Cu alloys.

Cu (%)	A	n	R ²	A	Fixed n	R ²
Coefficients in Eq. (2) with "total" cooling rate (DAS in μm)						
0.98	134.8 ± 4.4	0.40 ± 0.01	0.985	137.8 ± 7.3	0.33	0.96
2.12	101.4 ± 2.8	0.40 ± 0.01	0.996	107.6 ± 5.6	0.33	0.97
3.24	83.6 ± 0.01	0.37 ± 0.02	0.988	87.8 ± 3.1	0.33	0.98
4.3	76.1 ± 0.01	0.40 ± 0.02	0.990	79.9 ± 3.9	0.33	0.97
Coefficients in Eq. (2) with "linear" cooling rate (DAS in μm)						
0.98	144.7 ± 0.01	0.44 ± 0.03	0.99	145.3 ± 10.2	0.33	0.93
2.12	110.2 ± 2.9	0.47 ± 0.02	0.99	116.6 ± 9.2	0.33	0.93
3.24	94.4 ± 1.8	0.40 ± 0.02	0.99	96.8 ± 3.9	0.33	0.98
4.3	85.6 ± 3.8	0.41 ± 0.01	0.97	88.4 ± 5.8	0.33	0.94

R² is the statistical coefficient of determination which indicated the proximity of the fitting trendline to the actual experimental results (the value goes from 0 to 1, being 1 a 100 % fit of the trendline with the actual experimental results).

It was also observed a decrease of grain size when increasing cooling rate and Cu concentration. In the case of Cu concentration, larger refinement was observed when cooling is slow. This is demonstrated in Figure 5.4, considering the total cooling rate. The coefficients in Eq. 1.5 were also obtained for the grain size by using linear regression analysis. Table 5.4 gives the resulting coefficients.

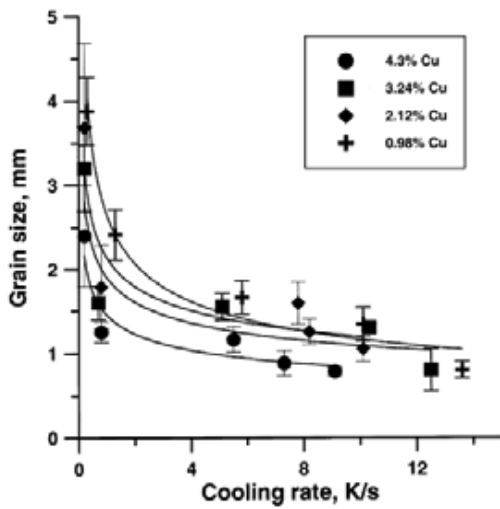


Figure 5.4. Grain size as a function of cooling rate and composition.

Table 5.4. Coefficients A and n in Eq. 1.5. considering the grain size instead of the SDAS.

Cu (wt%)	A	n	R^2
0.98	2.62	0.33	0.97
2.12	2.18	0.29	0.89
3.24	1.94	0.26	0.85
4.3	1.47	0.27	0.90

In Table 5.4, the coefficient A decreases with increasing Cu concentration. The coarsening coefficient n has values close to 0.3.

The influence of solute content (in this case Cu) and cooling rate on SDAS and grain size is a well known phenomenon. SDAS and grain size become refined with increasing cooling rate and solute content. Increasing the cooling rate reduces the local solidification time, thus reducing the time for dendrite branches to further develop by coarsening. On the other hand, the solutal influence on structure refinement is ascribed to a lowering in the dendrite tip velocity and smaller tip diameter [2, 31]. Also, hindered grain growth is caused by solute pile-up at the solid-liquid interface which can also provoke constitutional undercooling enhancing grain nucleation, and thus grain refinement

The influence of composition and cooling rate with the structure development should be considered when employing experimentally measured SDAS for the determination of the cooling rate in large ingots and billets where macrosegregation can be of great importance.

5.3.2. Non-equilibrium eutectics

As demonstrated earlier (see Table 5.2), the effect of cooling rate on the formation of non-equilibrium eutectics is the most controversial. The influence of cooling rate on the amount of eutectics has been described as follows: first, the amount of eutectics increases with increasing the cooling rate up to a point where saturation is reached (predicted with the Gulliver–Scheil model); and second, after reaching the saturation point the amount of non-equilibrium eutectics decreases at high cooling rates (i.e. in the range between $>10^2$ to 10^3 K/s) due to hindered diffusion in the liquid phase and corresponding solute trapping in the solid phase.

In our study, the amount of non-equilibrium eutectics resulting from non-equilibrium solidification due to microsegregation was determined in samples solidifying at different cooling rates. Figure 5.5a shows the effect of cooling rate, influenced by the mould size and type, on the amount of non-equilibrium eutectics. It can be observed that the amount of non-equilibrium eutectics increases with increasing Cu in the alloy in the range of slow cooling. The maximum value remains almost two times below to that predicted by using the Gulliver–Scheil approximation. The amount of eutectics decreases within the cooling range of 1–2 to 10 K/s. These results are not in accordance with the majority of reference data (see Table 5.2). At first instance, this behaviour may be due to the fact that larger-sized samples may enable thermo-solutal convection and shrinkage-driven flow which can lead to segregation and thus local decrease in the amount of eutectics.

In order to clarify the above mentioned results, another set of samples as studied. In this case, the samples had the same size and volume and the cooling rate was manipulated by exposing the samples to different cooling media (Fig. 5.5b). The same tendency behaviour was observed, however, the slope in the curve is even more pronounced than in Fig. 5.5a. Moreover, it can be seen that the amount of eutectics is larger when quenching at the eutectic temperature than when continuing cooling the sample to room temperature.

For the samples cooled with the same dimensions and volume, factors such as thermosolutal convection and/or shrinkage-driven flow should influence solidification in the samples in the same manner, thus allowing comparison of results. As it can be seen in Fig. 5.5b, the amount of non-equilibrium eutectics is influenced by the cooling rate in a rather same way as in Fig. 5.5a. Based on this observations and experimental considerations, we describe the effect of

cooling rate on non-equilibrium eutectics based on our experimental results as follows:

- 1) Back diffusion of solute in the solid phase at the solid-liquid interface during solidification and homogenization in the solid may be occurring. This effect may be facilitated in finer structures which form at high cooling rates. The liquid phase, therefore, has less solute which eventually solidifies as eutectic.
- 2) Homogenization during continuous solidification is the most dominant factor for the reduction of non-equilibrium eutectics (see Fig. 5.5b). This can be demonstrated with the samples which were cooled continuously to room temperature, since the amount of eutectics found was lower than the amount of eutectics found in samples quenched at the eutectic temperature. Thus, dissolution of non-equilibrium eutectics during homogenization is to a greater extent the main factor which decreases the amount of eutectics.

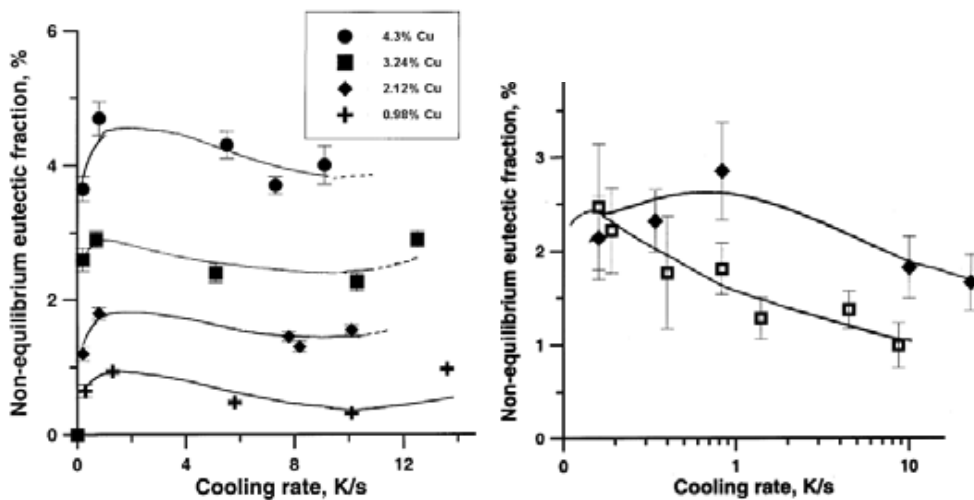


Figure 5.5. (a) Effect of cooling rate and Cu concentration on the amount of non-equilibrium eutectics; and (b) effect of the cooling rate and the cooling regime on the amount of non-equilibrium eutectics, where \square is the Al-1.83 wt.% Cu alloy cooled to room temperature and \blacklozenge is the Al-1.86 wt.% Cu alloy quenched from the eutectic temperature of the alloy.

It would be difficult to predict the same solidification process by using the available 1D models [32]. Since, these models [e.g. 33] do not incorporate structural aspects such as dendrite arm spacing, coarsening and interaction between dendrite arms during solidification.

Q. Du et al. [34] demonstrated later the influence of cooling rate on the amount of eutectics, presented here, by using a 2D microsegregation model. The pseudo-front tracking model (PFT) [35] was used to demonstrate this observation. They demonstrated that coarsening is the main phenomena dominating which influences the amount of non-equilibrium eutectics during solidification. Thus, microstructural changes such as dendrite arm spacing and interaction between dendrite arms are factors which should be consider in order to predict more accurately the solidification of alloys. This observation comes in agreement with those described in Chapter 3, where unconstrained growth of dendrites and their interaction in 3D space can influence the structure development in a more complex manner.

5.4. The Role of Fragmentation in the Formation of Duplex Structures

5.4.1. 3D grain morphology

The structure of the 7050 billet alloy (described in Section 5.2.2) was characterized by conventional 2D metallography analysis revealing an equiaxed-type grain morphology having an average grain size of $166 \pm 5 \mu\text{m}$. Fine-cell grains have an average dendrite arm spacing of $23.4 \pm 2.8 \mu\text{m}$ and coarse-cell grains, $66.3 \pm 2.2 \mu\text{m}$. The average grain size of a fine-cell grain is $155 \pm 5 \mu\text{m}$ and that of a coarse-cell grain, $230 \pm 6 \mu\text{m}$. Coarse-cell grains occupy approximately 50% of the sample area. Figure 5.6 displays the features found within the 3D-reconstructed microstructure. Figure 5.6a demonstrates a large coarse-cell grain which is $\sim 477 \mu\text{m}$ in cross-section. Figure 5.6b exhibits a fine-cell grain which is twice smaller than the one shown in Fig 5.6a. Also less-developed grains can be found within the microstructure (Fig. 5.6c), these being thinner and having a sharp protrusion. In size these less-developed grains are comparable to fine-cell equiaxed grains and have approximately the same volume but are less branched. Less-developed grains are not a common feature of the structure, they are rather scarce. As mentioned before, it is difficult to have perfect etching on some of the sections, thus the morphology of the 3D reconstructed features is not perfectly defined and sometimes appears more as a blob-type structure. Nevertheless, 3D visualization of the microstructure enables us to distinguish the different features within the overall structure and to compare the length-scale of such features. Figure 5.7 shows a complete 3D volume of the microstructure exhibiting the different grains. In addition, 3D

microstructure reconstruction reveals true interconnectivity between pores within the volume reconstructed (Fig. 5.7).

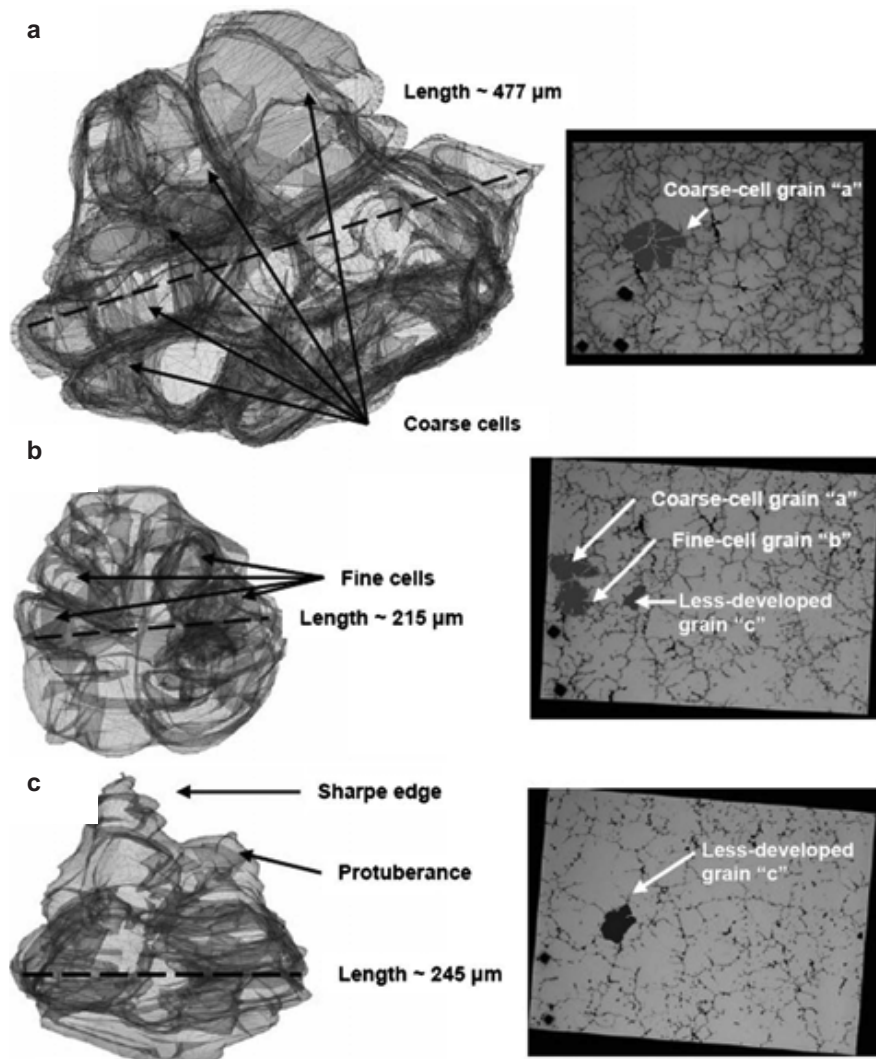


Figure 5.6. 3D-reconstructed microstructural features found within the microstructure: (a) coarse-cell equiaxed grain, (b) fine-cell equiaxed grain and (c) fragment. At the right-hand side of each feature, the section is shown where the largest cross-section of the feature was found.

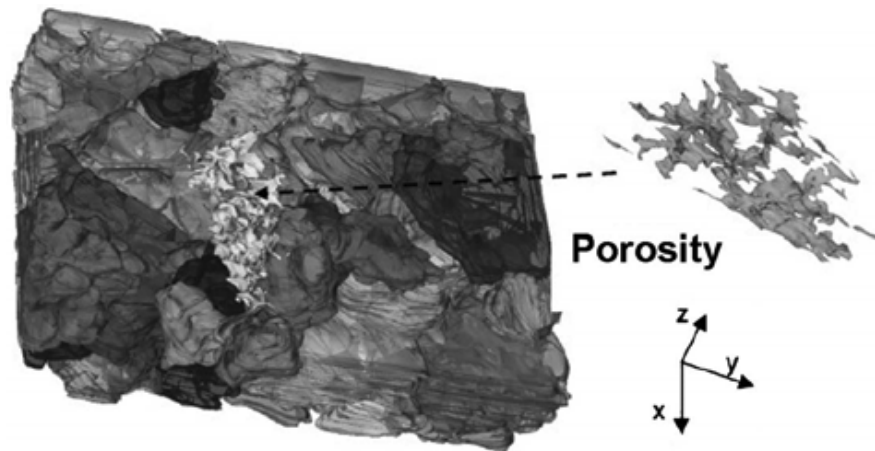


Figure 5.7. 3D volume reconstruction of the microstructure ($x= 1208 \mu\text{m}$, $y= 897.5 \mu\text{m}$ and $z= 274.5 \mu\text{m}$) showing interconnectivity of pores in 3D space (the grains within the volume are distinguished by different tone of semitransparent gray).

Figure 5.8a demonstrates the S_V obtained for the different features found within the microstructure. The S_V estimated from 2D cross-sections is lower compared to true 3D S_V measurements. The difference between 2D S_V estimation and 3D S_V measurements is about $0.005 \mu^{-1}$. After correction with the spherical aberration factor k (Fig. 5.8b), 2D S_V estimation becomes closer to 3D S_V measurements for fine-cell and coarse-cell grains (Fig. 5.8a). On the other hand, the use of k for correction of S_V for less-developed grains gives an overestimation of 3D S_V values. The S_V is larger for fine-cell grains and less-developed grains than for coarse-cell grains. This means that coarse-cell grains are indeed coarser and less branched. The secondary dendrite arm spacing is expected to be larger for these grains as compared to the secondary dendrite arm spacing of fine-cell grains and less-developed grains, since the secondary dendrite arm spacing is inversely proportional to S_V .

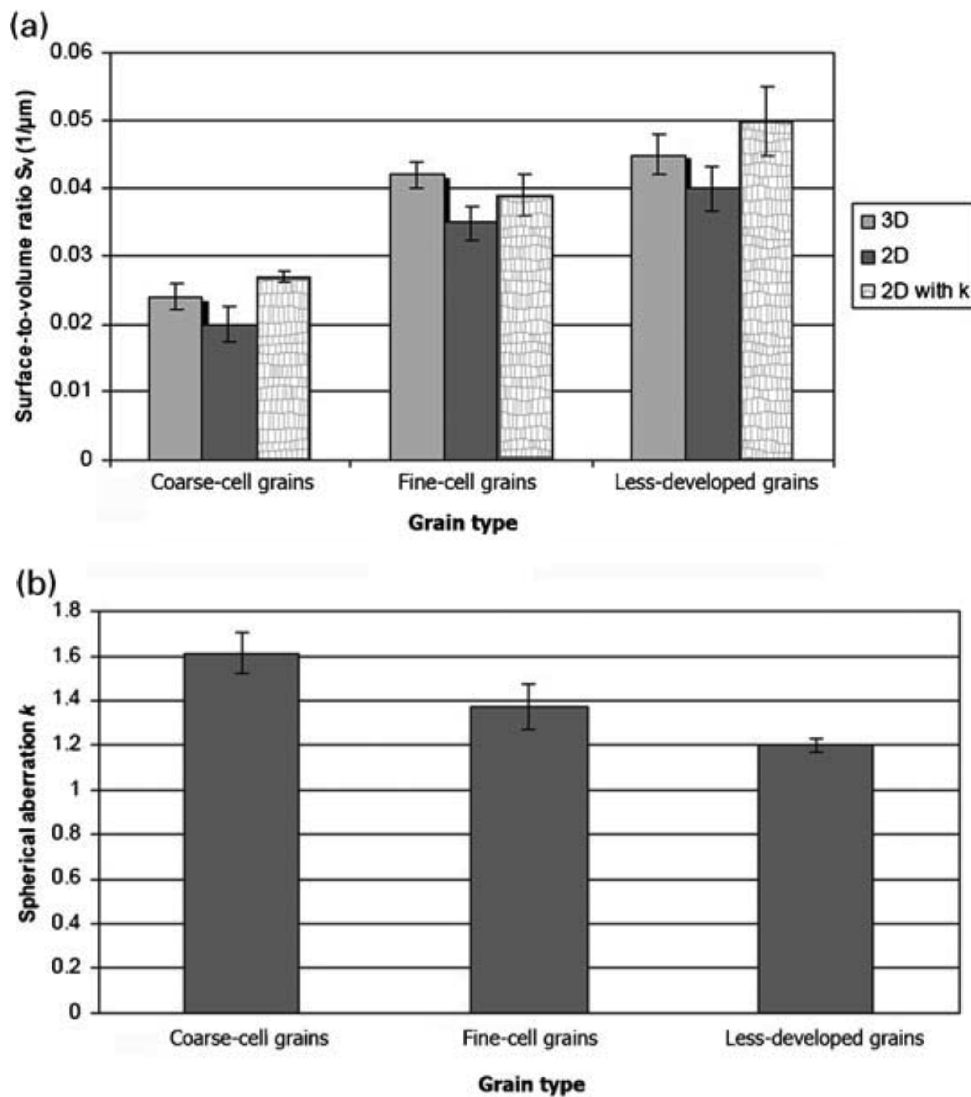


Figure 5.8. (a) Grain morphologies and their respective surface-to-volume ratio (specific surface) S_V calculated from 3D-reconstructed and 2D-acquired images and (b) estimate 2D spherical aberrations (k) from acquired 2D cross-sections.

5.4.2. Microsegregation

The line-scan measurements to analyze solute distribution were done over the features observed in the microstructure (as described in Section 5.2.2.4).

Figures 5.9–11 demonstrate examples of solute distribution profiles taken on the coarse-cell grains, fine-cell grains and less-developed dendrites (fragments). It is obvious that the coarse dendrite cells are depleted in solute (Fig. 5.9) compared to the fine dendrite cells (Fig. 5.10) and apparent fragments (Fig. 5.11). This qualitative conclusion is supported by quantitative measurements of the minimum concentrations of alloying elements in different types of dendrite cells (Table 5.5) and the average concentrations of areas occupied by different types of dendrite cells (Table 5.6). These results show that the coarse-cell areas are depleted of solute elements whereas the fine-cell areas and less developed grains are enriched in solute elements. Interestingly enough the less developed grains or fragments contain more solute elements than the fine-cell grains.

Table 5.5. Minimum concentration of alloying elements in dendrite cells.

Type of cells	Mg, %	Zn, %	Cu, %	Ti (max), %
Coarse cell	0.62 ± 0.02	4.5 ± 0.1	0.35 ± 0.2	0.050 ± 0.002
Fine cell	0.71 ± 0.02	5.8 ± 0.1	0.7 ± 0.2	0.009 ± 0.002
Fragment	1.04 ± 0.02	7.4 ± 0.1	1.1 ± 0.2	0

Table 5.6. Average concentration of areas occupied by the type of grain.

Type of cells	Mg, %	Zn, %	Cu, %	Ti, %
Coarse cell	0.86 ± 0.02	5.5 ± 0.1	0.7 ± 0.2	0.014 ± 0.002
Fine cell	1.10 ± 0.02	7.1 ± 0.1	1.4 ± 0.2	0
Fragment	1.13 ± 0.02	7.5 ± 0.1	1.5 ± 0.2	0

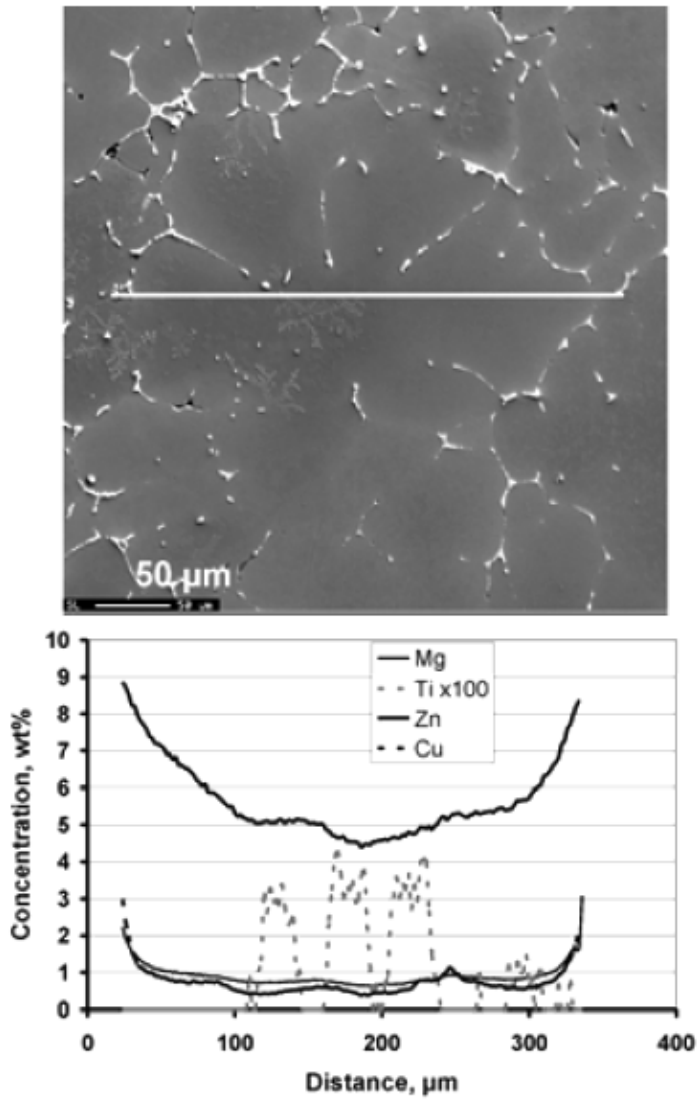


Figure 5.9. Line-scan showing solute distribution in a typical coarse-cell grain.

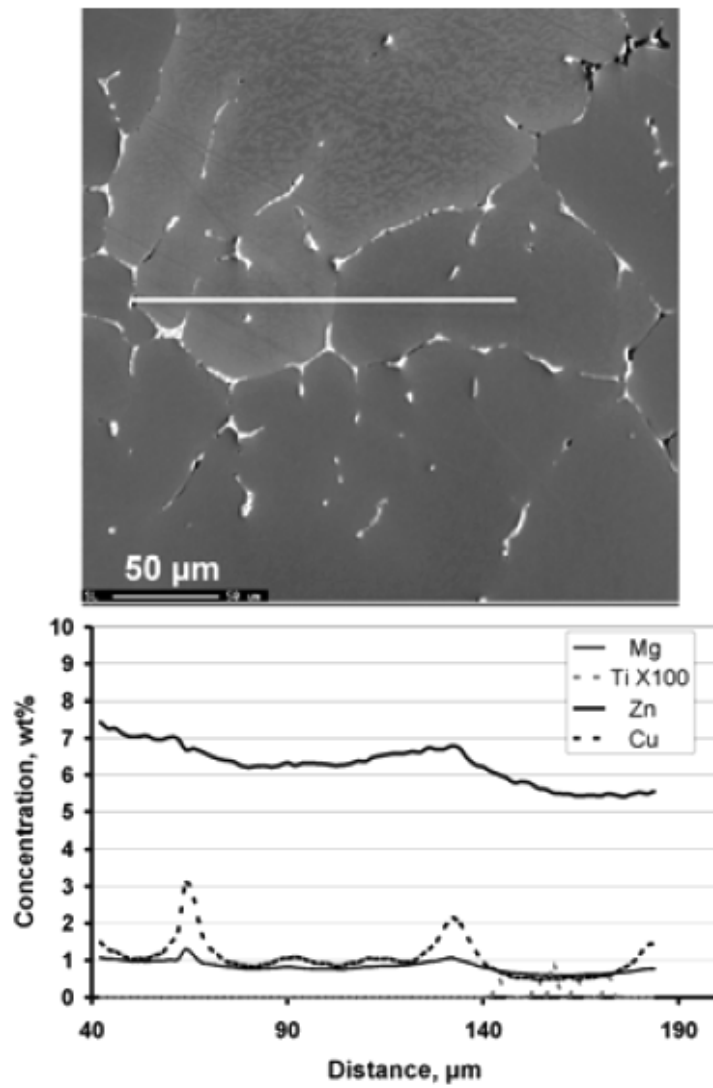


Figure 5.10. Line-scan showing solute distribution in a fine-cell grain.

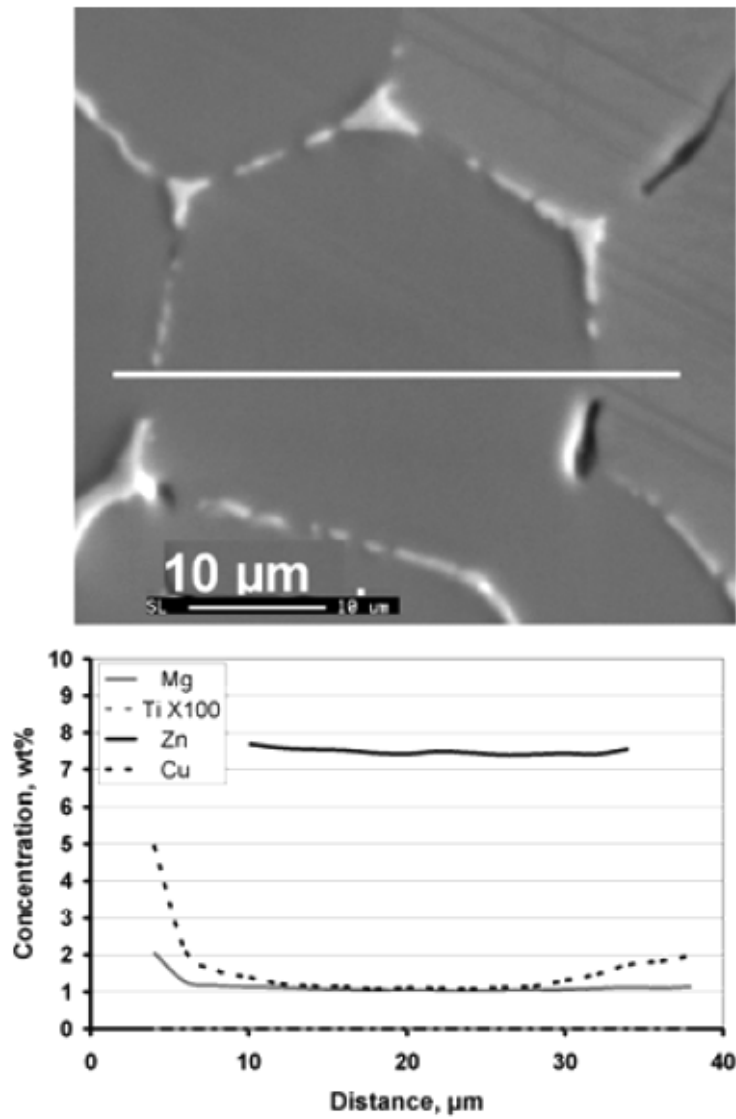


Figure 5.11. Line-scan showing solute distribution in a less-developed grain (i.e. fragment).

The solidification path of the 7075 alloy was determined by *Thermocalc* Software. The solidification path of the alloy allowed us to determine the liquidus at 640 °C, equilibrium solidus at 562 °C, and non-equilibrium solidus below 475 °C. The development of the solid fraction upon non-equilibrium (Scheil-type) solidification is shown in Figure 5.12. Table 5.7 gives the summary of equilibrium (interfacial) composition of solid (Al) phase, corresponding temperatures in the solidification range and solid fraction. The last values are determined using the plot in Fig. 5.12, i.e. non-equilibrium solidification path.

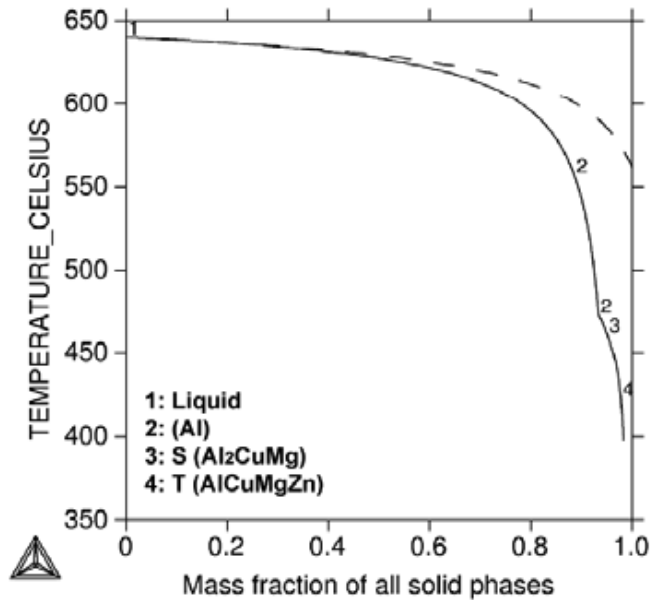


Figure 5.12. Solidification paths determined by Gulliver–Scheil approximation (solid line) and equilibrium solidification (dashed line).

Table 5.7. Calculated solute content in the solid at the solid-liquid interface and corresponding solid fractions upon Gulliver–Scheil approximation.

T, °C	Mg, wt%	Zn, wt%	Cu, wt%	Mass solid fraction
640	0.40	2.37	0.147	0
630	0.58	3.25	0.254	0.44
625	0.66	3.62	0.317	0.53
620	0.736	3.95	0.387	0.61
615	0.807	4.23	0.462	0.67
605	0.934	4.69	0.631	0.75
600	0.99	4.87	0.724	0.78
590	1.09	5.17	0.92	0.82
580	1.18	5.39	1.13	0.85
570	1.26	5.56	1.35	0.87

Three-dimensional reconstruction of as-cast structure showed the presence of three morphological types of grains, namely grains with coarse internal structure (coarse dendrite cells), grains with fine internal structure (fine dendrite cells) and grains with only few but fine dendrite cells (less-developed grains).

Quantification of these morphologies demonstrated that the specific surface area S_V of coarse-cell grains is indeed smaller than that of the fine-cell and less-developed grains. This confirms the qualitative conclusion made from 2D metallographic observations that the coarse-cell grains are indeed coarser and less branched than their fine-cell counterparts. The analysis of 3D morphologies and comparison with 2D images revealed the systematic underestimation of the tortuosity of real dendritic structure when using usual metallographic observations. It is also demonstrated that the 2D examination of microstructures can be supplemented with quantitative correction for the 3D morphology by using the k factor as given in Fig. 5.8. It is shown that the k factor estimated from 2D images of equiaxed coarse- and fine-cell grains can serve as an appropriate means to approach the true S_V . For less-developed grains, however,

such a correction results in further overestimation of S_V . Although these grains have a rather irregular shape with a sharp edge and protrusions (Fig. 5.6c), their estimated k factor is ~ 1.2 (Fig. 5.8b), which wrongly suggests that less-developed grains have a nearly spherical morphology, which is not confirmed by 3D reconstruction. Hence, the estimation of k from 2D cross-sections of fragments is not relevant.

It has been demonstrated before the contribution of coarse-cell grains to macrosegregation as being negative since they are depleted in solutes as compared to the fine-cell grains [26]. This observation can be confirmed with the analysis presented here for grain-refined 7050 alloys cast at low speeds. Thus we can suggest that, this alloy under these casting conditions can develop a duplex structure having coarse-cell grains and fine-cell grains which are depleted and enriched in solutes (according to the nominal composition of the alloy) respectively.

In addition to our observations, another type of grain was revealed from 3D reconstructed microstructures. This type of grain morphology corresponds to a less-developed grain-type, what we suggest as being a dendrite fragment. Small grains have been reported before for a non-grain-refined 5182 alloy billet [28]. The mechanism of formation of this type of grain has been suggested as being by “showering” of grains at the early state of solidification. Also, they suggested that these grains are the reason for the negative centerline segregation [28]. However, this study did not carry out a complete morphology analysis of the results, relying just on 2D stereological observations. We know that some small portions observed in a 2D plane can be in reality part of a larger grain, and for this 3D reconstruction and morphology analysis are needed. The type of less-developed small grain presented here, after 3D reconstructions) corresponds to a fragment-like structure having a protrusion and to be rather

elongated compared to the other two structures i.e. coarse-cell grains and fine-cell grains. The stereological analysis confirms the differences in morphology between the type of grains and the fragment. The protrusion of this less-developed grain suggests that it was detached from a parent branch. These grains could have been developed closer to the border between the slurry and the mushy region. Since they are enriched in solutes, we can suggest that they not contribute to the negative centerline macrosegregation.

It can be concluded that there are three types of grains with distinctly different morphologies that appear in the center of the billet. Coarse-cell grains are depleted in solutes and usually called “floating crystals” or “floating grains” indicating their origins in the semi-liquid, upper part of the two-phase solidification region. These grains may also be suspended in the upper and hotter part of the two-phase region, grow and coarsen substantially before settling to the bottom of the sump. Fine-cell grains are likely to solidify faster, going along a straighter trajectory from liquidus to solidus, or forming in a later stage of solidification, deeper in the slurry zone. Less-developed grains can represent fragments detached by melt from the coherent dendritic network and transported to the center of the billet by convective currents, or fragments formed at the coherent solidification front due to solute accumulation, or can be formed independently from the enriched liquid deeper in the slurry. The formation of less-developed grains is likely to occur at the border between the semi-liquid slurry zone and the semi-solid mushy zone. Figure 5.13 schematically represents the sump of the billet with suggested locations of growth for different types of grains observed in this study. Using the information of the minimum concentrations of solutes in the dendrite cells (Table 5.5), the calculation of equilibrium (interfacial) composition of the solid (A1) phase, and the calculation of non-equilibrium development of the solid

fraction during solidification (Table 5.7), we can attempt the evaluation of the stage of solidification when the observed morphologies have been formed.

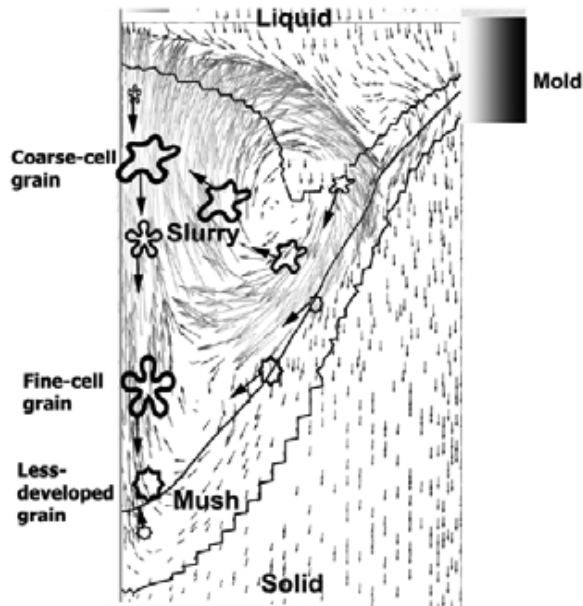


Figure 5.13. Schematic representation of one half of the billet sump with characteristics regions (centre of the billet sump at the left-hand side), flow velocity vectors, and suggested locations of growth for different grain morphologies found in the centre of the billet.

With taking into account that the billet was stress-relieved before examination, one could suggest that some solid-phase diffusion might be facilitated, increasing the measured minimum concentrations given in Table 5.5 as compared to the calculated values in Table 5.7. However, the structure with non-equilibrium eutectic veins and microsegregation profiles in Fig. 5.9-11 clearly indicates that the homogenization is far from being complete. We can then argue that the concentration of the element in Table 5.5 that gives the minimum fraction solid in Table 5.7 is the closest to the reality. It appears the concentrations of Mg and Cu are the most indicative. The analysis shows that

examined coarse-cell grains form at approximately 0.5–0.6 fraction solid; fine-cell grains at about 0.6–0.75 fraction solid, and less-developed grains at about 0.8 fraction solid. These values are of course on the higher side due to the two main reasons (1) possible diffusion during solidification, cooling in the solid state, and stress-relief annealing afterwards and (2) strict calculation conditions of the Scheil approximation (no solid diffusion). Nevertheless, these results allow us to make the following conclusions. First, there is a considerable difference in the temperature and, therefore in the stage of solidification (or position in the sump of a DC cast billet) where the grains of different morphologies are formed. Second, the coarse-cell grains are formed in the upper part of the solidification range, possibly above the coherency isotherm, which can be rather low in grain refined alloys [14]. Third, fine-cell grains and less-developed grains are formed in the lower part of the solidification range.

The mechanisms of fragmentation demonstrated in Chapter 4 can be related to the observations given here. The coarse-cell grains or floating grains can be related to the fragment which develops due to solute enrichment (in Section 4.5, Fig. 4.11) since it develops rather close to the solidification front. While less-developed grains or fragments can be related to the fragments which develop due to coarsening (in Section 4.5, Fig. 4.14) in the lower part of the solidification range. Fragments developing in open regions due to solute enrichment can develop further as described in Section 4.5.4. Thus, floating grains can develop in the same manner. On the other hand, less-developed grains, which are produced due to coarsening in the lower part of the solidification range, may encounter other dendrite branches blocking their further development.

These observations can be also analyzed as follows:

The solid fraction, at which fragmentation occurred, due to coarsening and solute enrichment, was calculated from the solidification path of the Al–20 wt.% Cu alloy (considering lever rule and Scheil approximation). This was done by determining the temperature T (assuming equilibrium) in the region where fragmentation occurred: $a = (T_L - T) / G_T$ or $T = T_L - aG_T$, where a is the mush depth from the dendrite tip to where fragmentation occurred within the mush, T_L is the liquidus temperature of the alloy (i.e. 603 °C or 876.15 K) and G_T is the thermal gradient (48 K mm⁻¹). Fragmentation due to coarsening occurred at $a = 411$ and 360 μm (two events) and due to solute enrichment at $a = 234$ μm. Substituting these values into the formula, this gives: due to coarsening $T = 583.27$ °C and 585.72 °C, and due to solute enrichment $T = 591.85$ °C. Accordingly, the solid fractions at which fragmentation occurred respectively are: ~ 0.24 (Scheil) ~ 0.27 (lever rule), and ~0.20 (Scheil) ~ 0.25 (lever rule) due to coarsening and ~ 0.15 (Scheil) ~ 0.16 (lever rule) due to solute enrichment. Therefore, fragmentation due to solute enrichment occurs at lower solid fractions as compared to fragmentation due to coarsening. In conclusion, fragments developing due to solute enrichment may further evolve as floating grains.

5.5. Concluding Remarks

The microstructure development during the solidification of aluminium alloys influences greatly the formation of the final structure. Thus, cast defects also depend on the development of the microstructure. This final chapter demonstrates, based on experimental analysis, the influence of phenomena such as coarsening and fragmentation on the composition distribution of a cast billet

(macrosegregation). In this case, it has been shown that coarsening and fragmentation influences greatly the formation of non-equilibrium eutectics and duplex structures (finer-cell and coarse-cell equiaxed grains).

The most important conclusions of this chapter are drawn as follows;

- 1) The solidification conditions influence the structure formation. The structure becomes refined in aluminium alloys when the cooling rate and the amount of Cu are increased.
- 2) The amount of non-equilibrium eutectics increases with increasing Cu concentration. The amount of eutectics increases with cooling rate in the range 0–1 K/s and then decreases in the range 1–10 K/s.
- 3) The experimentally observed dependence of the fraction of non-equilibrium eutectics on the cooling rate can be qualitatively explained in terms of the coarsening of the dendrite arms, the undercooling of the eutectic reaction and more active back diffusion in a finer structure. The homogenization and dissolution of non-equilibrium eutectics upon cooling in the solid state can further contribute to the observed decreasing amount of eutectics.
- 4) 3D microstructure reconstruction allowed the distinction of the true different morphological features that develop during casting i.e. coarse-cell grains, fine-cell grains (i.e. duplex structure) and less-developed grains.
- 5) 2D stereological correction may assist in the distinction between coarse-cell grains and fine-cell equiaxed grains. However, stereological assistance may be useless for distinguishing less-developed grains due to their less-branched morphology and different morphology (tear-like morphology).
- 6) Microsegregation analysis on coarse-cell, fine-cell and less-developed grains allowed to identify their origins during casting.
- 7) It was shown that coarse-cell grains are formed at higher temperatures in the upper part of the solidification range (slurry zone) and are depleted of solute elements. As a result their contribution to centerline macrosegregation is

negative. Fine-cell grains are formed at a lower temperature, are enriched in solute and, therefore positively contribute to the macrosegregation. Less-developed grains are formed even deeper in the two-phase region zone and are strongly enriched in solutes.

References

- [1] M.C. Flemings, *Solidification Processing*, McGraw-Hill, NY, USA, 1974.
- [2] K.P. Young, D.H. Kirkwood, *Metall. Trans. A* 6A (1975) 197.
- [3] J.A. Sarreal, G.J. Abbaschian, *Metall. Trans. A* 17A (1986) 2063.
- [4] P.N. Anyalebechi, T.N. Rouns, R.E.J. Sanders, *Light Metals 1991*, The Minerals, Metals and Materials Society, Warrendale, USA, 1991, 821.
- [5] H. Westengen, *Z. Metallkde.* 73 (1982) 360.
- [6] C. Devadas, I. Musulin, O. Celliers, *Proceedings of the Fifth International Extrusion Technology Seminar*, vol. I, The Aluminum Association, WA, USA, 1992, 121.
- [7] M.H. Mulazimoglu, J.E. Gruzleski, B. Closset, *Aluminium* 68 (1992) 489.
- [8] V.I. Dobatkin, *Neprieryvnoe Lit'e i Liteinye Svoistva Splavov (Continuous Casting and Casting Properties of Alloys)*, Oborongiz, Moscow, USSR, 1948.
- [9] Y.L. Liu, S.B. Kang, *Mater. Sci. Technol.* 13 (1997) 331.
- [10] V. Rontó, A. Roósz, *Int. J. Cast Met. Res.* 14 (2001) 131.
- [11] V. Rontó, A. Roósz, *Int. J. Cast Met. Res.* 13 (2001) 337.
- [12] J.E. Spinelli, D.M. Rosa, I.L. Ferreira, A. Garcia, *Mater. Sci. Eng. A* 383A (2004) 271.
- [13] M. Abdel-Reihim, N. Hess, W. Reif, M.E.J. Birch, *J. Mater. Sci.* 22 (1987) 213.
- [14] L. Arnberg, L. Backerud, G. Chai, *Solidification Characteristics of Aluminum Alloys, Dendrite Coherency*, vol. 3, American Foundrymen's Society, Des Plaines, USA, 1996.
- [15] Suyitno, D.G. Eskin, V.I. Savran, L. Katgerman, *Metall. Mater. Trans. A* 35A (2004) 3551.
- [16] C.-A. Gandin, Y. Bréchet, M. Rappaz, G. Canova, M. Ashby, H. Shercliff, *Acta Mater.* 50 (2002) 901.

- [17] T.P. Battle, Intern. Mater. Rev. 37 (1992) 249.
- [18] A.B. Michael, M.B. Bever, Trans. AIME J. Met. 202 (January) (1954) 47.
- [19] M.A. Taha, N.A. El-Mhallowy, R.M. Hamouda, Mater. Des. 23 (2002) 195.
- [20] S. Thompson, S.L. Cockroft, M.A. Wells, Mater. Sci. Technol. 20 (2004) 497.
- [21] S. Thompson, S.L. Cockroft, M.A. Wells, Mater. Sci. Technol. 20 (2004) 194.
- [22] A. Roósz, H.E. Exner, Acta Metall. Mater. 38 (1990) 375.
- [23] R.K. Paramatmuni, K.-M. Chang, B.S. Kang, X. Liu, Mater. Sci. Eng. A 379A (2004) 293.
- [24] G.-F. Liang, Z.-M. Xu, J.-G. Li, J. Mater. Sci. 39 (2004) 2569.
- [25] I.I. Novikov, V.S. Zolotarevskii, Dendritnaya Likvatsiya v Splavakh (Dendritic Segregation in Alloys), Nauka, Moscow, USSR, 1966.
- [26] D.G. Eskin, R. Nadella, L. Katgerman, Acta Mater. 56 (2008) 1358.
- [27] M.G. Chu, J.E. Jacoby, Light Metals 1990, C.M. Bickert, ed., TMS, Warrendale, PA, 1990, 925.
- [28] A.M. Glenn. S.P. Russo, P.J.K. Paterson, Metall. Mater. Trans. A 34A (2003)1513.
- [29] J.C. Fiala, J. Microscopy Pt 1 218 (2004) 52.
- [30] A. Thorvaldsen, Mater. Sci. Forum, 307 (1992) 94.
- [31] U. Feurer, Proceedings of Symposium Quality Control of Engineering Alloys, Delft University Press, Delft, The Netherlands, 1977, 131.
- [32] D.G. Eskin, Q. Du, D. Ruvalcaba, L. Katgerman, Mater. Sci. Eng. A 405A (2005) 1.
- [33] V.R. Voller, C. Beckermann, Metall. Mater. Trans. A 30A (1999) 2183.
- [34] Q.Du, D.G. Eskin, A. Jacot, L. Katgerman, Acta Mater. 55 (2007) 1523.
- [35] A. Jacot, M. Rappaz, Acta Mater. 50 (2002)1909.

Chapter 5 – Influence of Microstructure Development on the Structure Formation

Appendix

This appendix shows some of the figures for better appreciation of the described features which were demonstrated in grey-scale within the text.

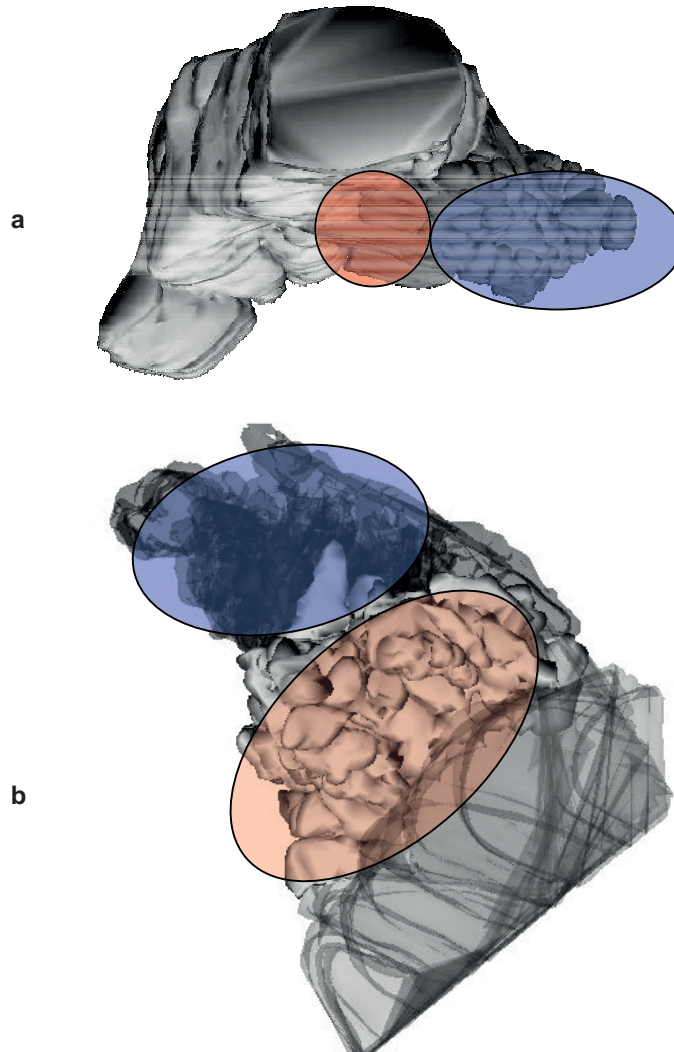


Figure A1 [Figure 3.21 in Chapter 3]. (a) Dendrite arm showing coalesced instabilities (highlighted in red) between the solid boundary and finer instabilities (highlighted in blue) and (b) dendrite tip showing coalescence of instabilities between the solid boundary and finer instabilities. 3D portion reconstructions taken from the Al-7 wt.% Cu alloy quenched at 631°C.

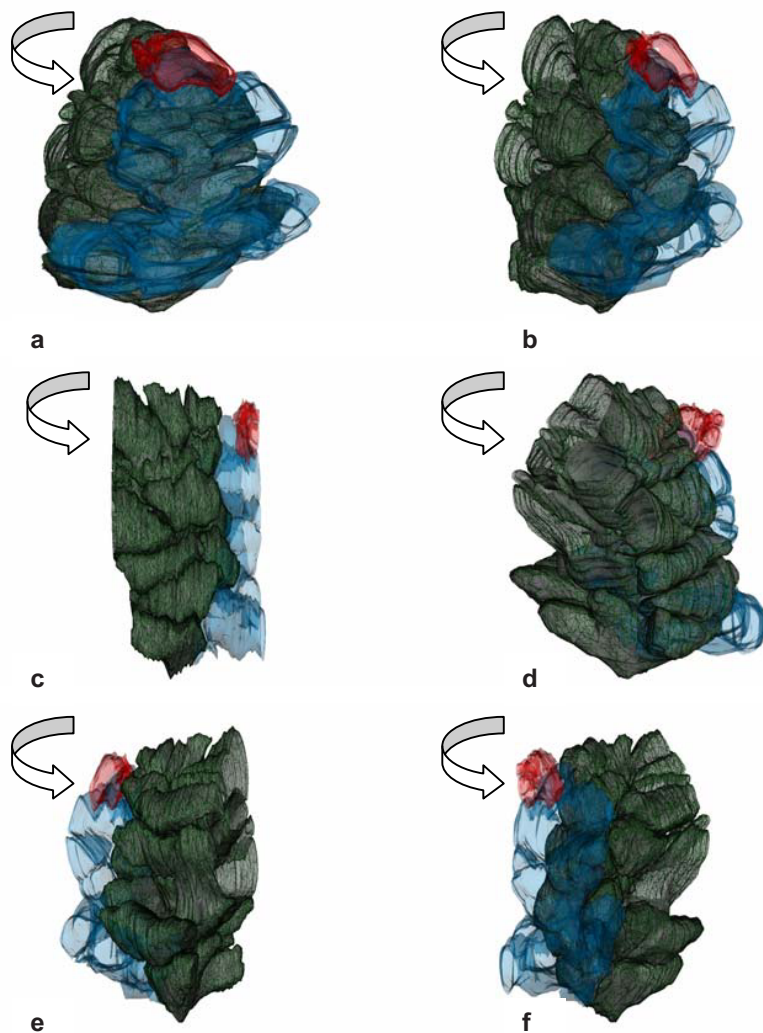


Figure A2 [Figure 3.23 in Chapter 3]. Couple dendrite branches developing due to tip splitting; where the transparent red portion corresponds to coalesced instabilities while the transparent green and transparent blue features correspond to a concave dendrite branch and to a convex dendrite branch, respectively.

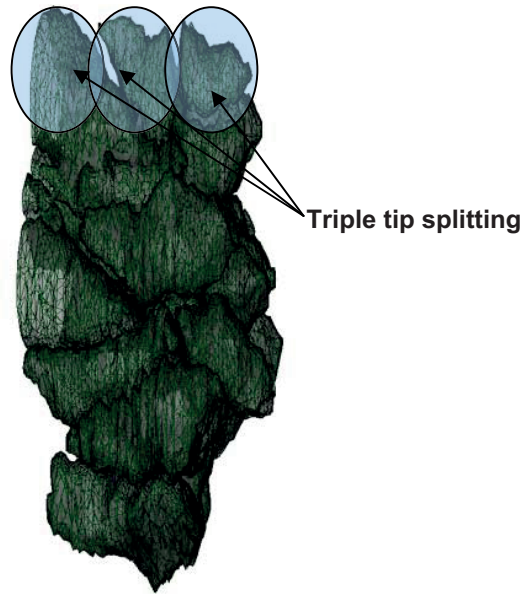


Figure A3 [Figure 3.24 in Chapter 3]. Dendrite branch after removing neighbouring dendrite branch exhibiting triple tip splitting.

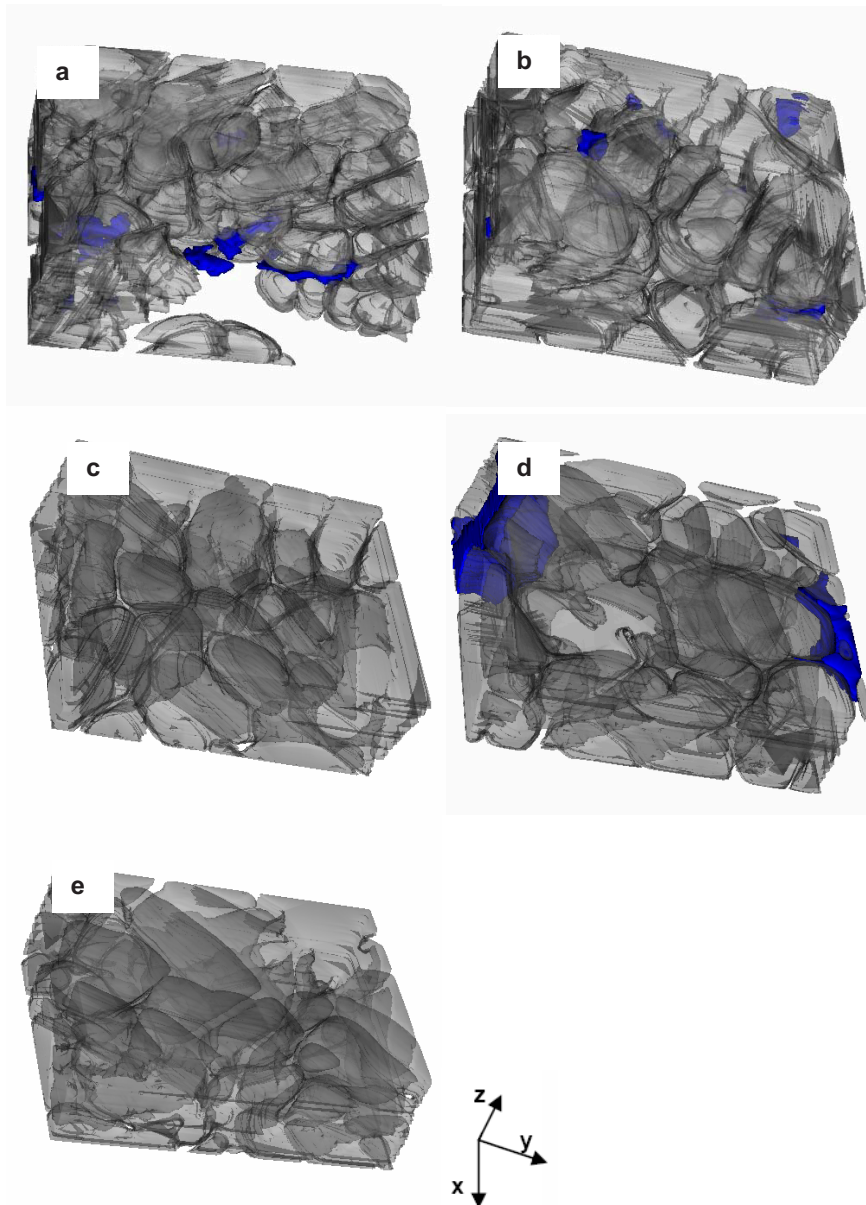


Figure A4 [Figure 3.25 in Chapter 3]. 3D microstructures of samples ($x= 318 \mu\text{m} \times y= 420 \mu\text{m} \times z= 155 \mu\text{m}$) quenched at: (a) 631 °C, (b) 620 °C, (c) 595 °C, (d) 583 °C and (e) 551 °C. Semitransparent grey and blue represent the solid phase and porosity respectively.

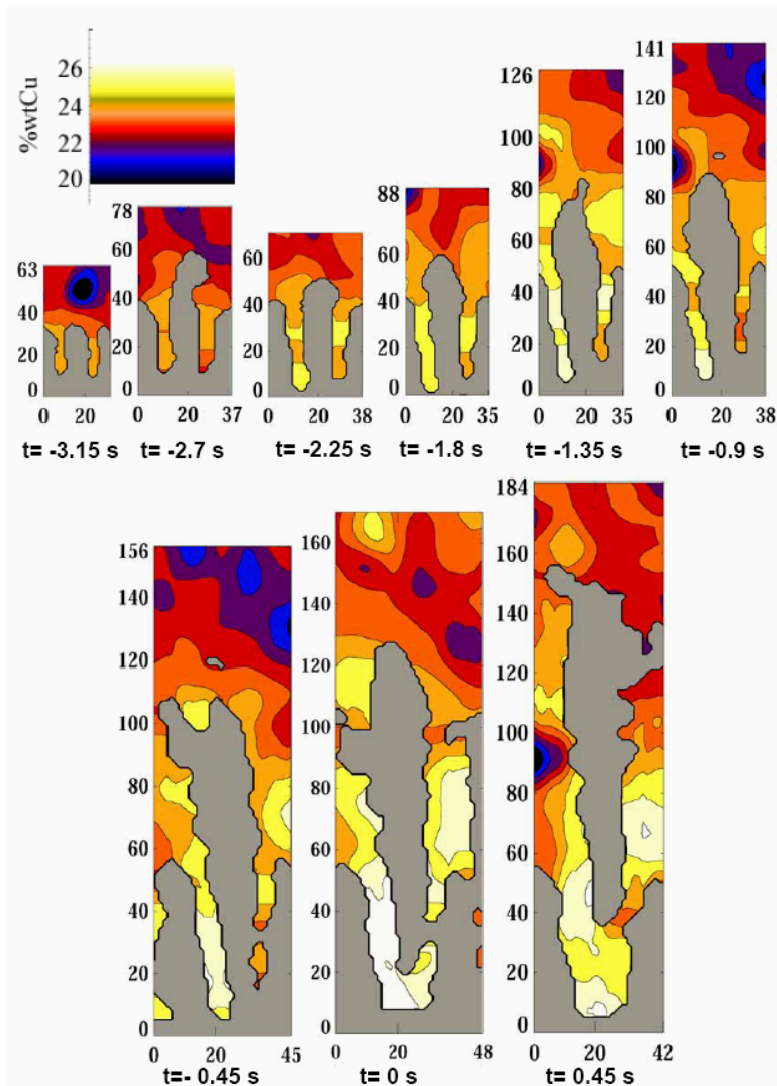


Figure A5 [Figure 4.11 in Chapter 4]. Contours showing solute enrichment during the fragmentation of the first tertiary dendrite arm (shown in Fig. 4.10). The wt.% Cu level colouring is indicated explicitly, and the masked-off solid has been coloured in grey. The scale is indicated in microns.

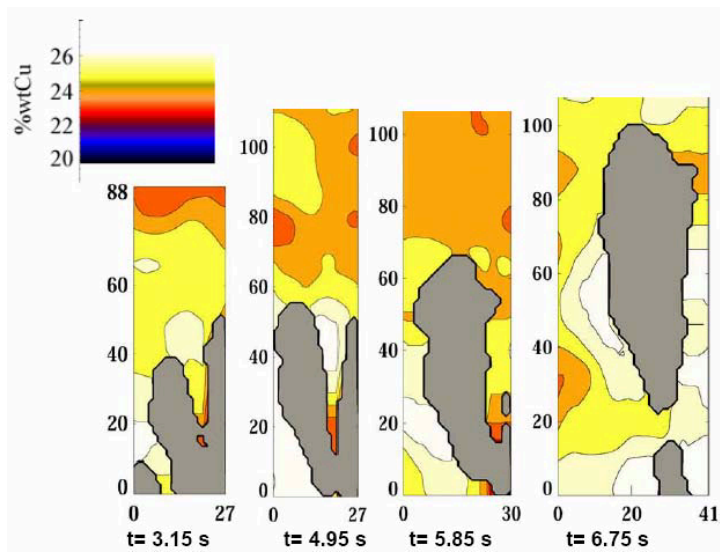


Figure A6 [Figure 4.14 in Chapter 4]. Contours showing solute enrichment during the fragmentation of a second tertiary dendrite arm (coloured in grey). The scale is indicated in microns.

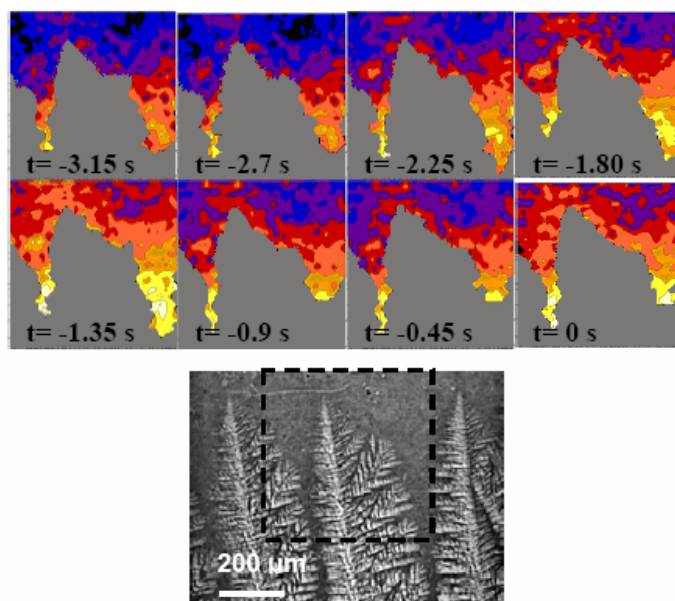


Figure A7 [Figure 4.15 in Chapter 4]. Envelops of dendrites (coloured grey) and colour contours showing the solute-rich liquid streaming down from the upper part of the columnar dendrite arm. The image at the bottom indicates the region where the images were taken.

Summary

This thesis describes experimental studies on microstructure development during the solidification of aluminium alloys. Introduction to the subject of the thesis is given in Chapter 1. Main experimental techniques and materials are described in Chapter 2. Specific details of experiments are given in the beginning of Chapters 3 through 5. The results and their discussion are reported in 3 chapters (Chapter 3, 4 and 5). The general conclusions are shown in this section. For more in detail conclusions on the results described in this thesis, the reader should refer to the Concluding Remarks at the end of Chapters 3, 4 and 5. The last chapter (Chapter 5) of the thesis demonstrates the influence of the microstructure development on the formation of the final structure and cast defects (such as macrosegregation, hot-tearing and porosity).

Studies were performed on the solidification of aluminium alloys under unconstrained and constrained solidification conditions. These conditions corresponded to solidification occurring without directionally imposed growth and with directionally imposed growth, respectively.

Unconstrained solidification of aluminium alloys [Chapter 3]. The overestimation of solid fraction found when studying the solidification of quenched structures is in part due to a rather inaccurate method of analysis, which implies the observation of 2D section images. It has been suggested that 3D microstructure reconstructions will facilitate the analysis of the true morphology of developing phases for accurate description of the solidification of alloys. Based on 3D microstructure analysis it is found that the overestimation of solid in quenched samples is due to the existence of features which have not been considered during 2D image analysis. These features

correspond to coalesced instabilities that develop during quenching and that appear as large blobs which gives the wrong impression of being part of the solid existing prior to quenching. After taking into account these observations, the measured overestimation of solid fraction becomes lower. It is concluded that the studied Al-alloys (i.e. Al-3 wt% Si and Al-7 wt% Cu), under the studied solidification conditions, have a tendency to solidify close to the Gulliver-Scheil solidification path approximation. Moreover, 3D microstructure reconstructions reveal complex morphologies which develop due to the unconstrained solidification conditions. During unconstrained solidification conditions, evolving dendrite envelopes may meet in certain places delaying the local growth due to thermal and solutal gradient overlapping. 3D structure development of alloys under unconstrained conditions can lead to complex dendrite branch morphologies which develop due to coarsening and coalescence. Complex accommodation of dendrite branches are observed in 3D reconstructed quenched structures. We call this accommodation “coupled dendrite branches”, where branches accommodate one on top of the other with one fitting side being concave while the other one from the neighbouring branch being convex.

Constrained solidification of aluminium alloys [Chapter 4]. Dendrite coarsening and fragmentation during solidification are analyzed from images taken in-situ during directional solidification of Al-high Cu alloys. It is found that the kinetics of coarsening during solidification is influenced by natural fluctuations in local segregation and dendrite growth. During downward growth, solute saturation occurs at the solidification front followed by sedimentation away from the mush. These fluctuations affect local growth and coarsening kinetics within the mush. During upward growth, on the other hand, solute saturation occurred at the front followed by solute settlement and accumulation within the mush. The solute distribution is shown to influence the growth and coarsening

kinetics. The distribution of solute-rich liquid was affected by the geometrical arrangement of dendrite branches. Based on the analysis of these observations, it is found that the coarsening exponent, which reflects the degree of coarsening of secondary dendrite branches, may become even larger than the values reported in literature. It is observed that these coarsening values may be due to the growth of higher-order branches which tend to separate branches from each other and to the competitive growth that can overshadow the true coarsening values. A new dendrite fragmentation mechanism, which has not been described before, is demonstrated in the thesis. The dendrite fragmentation phenomenon is found to be due to solute enrichment. High-order branches can become detached from the parent dendrite trunk during solidification when these are in contact to solute-rich liquid which can promote local growth undercooling at the branch tip and solute saturation at the root of the branch. Dendrite fragmentation due to solute enrichment is influenced by coarsening but mainly by the growth at the tip of high-order branches. While separated, these fragments can continue developing as equiaxed dendrites. This mechanism of fragmentation can be more potent in promoting a transition in the structure known as columnar-to-equiaxed transition (CET).

Influence of microstructure development on the structure development [Chapter 5]. Solidification conditions influence the microstructure development. It is observed that the grain size and dendrite arm spacing become finer when increasing the cooling rate and the amount of solute (in this case Cu). Also the amount of non-equilibrium eutectics increases when increasing Cu. A complex influence of cooling rate on the amount of eutectics is found. The amount of eutectics increases with cooling rate in the range 0–1 K/s and then decreases in the range 1–10 K/s. Such a variation in the amount of eutectics with cooling rate is related to the coarsening of dendrite arms, eutectic undercooling, and back diffusion occurring in a finer structure. Homogenization and dissolution of

the eutectic phase upon cooling in the solid state can enhance the observed effect of lowering of the amount of non-equilibrium eutectics. Real as-cast structure of direct-chill cast billet is frequently inhomogeneous and is represented by a mixture of different grain morphologies. 3D microstructure reconstruction allows the appreciation of the true 3D morphology of grains in the as-cast structure i.e. coarse-cell grains, fine-cell grains (i.e. duplex structure) and less-developed grains. It is found that 2D stereological correction may help in characterization of grain morphology. In spite of this, 2D stereological correction may fail in differentiating between fine-cell grains and less-developed grains. Microsegregation analysis along with the analysis of grain morphology allows us to explain the origins of different grains during casting. The formation of the different types of grains can be described as follows: coarse-cell grains are formed at higher temperatures in the upper part of the solidification range (slurry zone) and are depleted of solute elements. As a result their contribution to centerline macrosegregation in direct-chill cast billets is negative. Fine-cell grains are formed at a lower temperature, are enriched in solute and, therefore, positively contribute to the centerline macrosegregation. Less-developed grains, on the other hand, may be formed even deeper in the two-phase region and are strongly enriched in solutes. These less-developed grains may have developed as dendrite fragments during casting.

It has been demonstrated that microstructure transitions occurring during solidification can affect the final structure and thus may influence the formation of cast defects. Local changes in the microstructure formation can influence greatly the development of the large-scale structure. Thus, all factors that play a role in the structure formation (e.g. dendrite coarsening, fragmentation, coalescence and microsegregation) should be taken into account in order to understand the formation of cast defects.

Samenvatting

Dit proefschrift beschrijft een experimentele studie naar de ontwikkeling van de microstructuur tijdens de stolling van aluminiumlegeringen. Een introductie van het onderwerp wordt gegeven in hoofdstuk 1. De experimentele methode en de gebruikte materialen worden algemeen beschreven in hoofdstuk 2, en meer specifieke details van de experimenten worden steeds gegeven aan het begin van de hoofdstukken 3 tot en met 5. In deze drie hoofdstukken worden vervolgens de resultaten beschreven en bediscussieerd. De belangrijkste conclusies worden hier kort samengevat. Meer gedetailleerde conclusies worden getrokken in de *Concluding Remarks* paragraaf aan het einde van hoofdstukken 3 tot en met 5. Het laatste hoofdstuk van dit proefschrift (hoofdstuk 5) toont de invloed van microstructuurontwikkeling op de vorming van de uiteindelijke structuur en gietfouten, zoals macrosegregatie, warmzscheuren en porositeit.

Stolling van aluminiumlegeringen is onderzocht onder stollingscondities met een beperkt aantal vrijheidsgraden en onder onbeperkte condities. Deze condities komen respectievelijk overeen met stolling met en zonder richtingsafhankelijke groeicondities.

Onbeperkte stolling van aluminiumlegeringen [hoofdstuk 3]. De overschatting van de vaste aluminiumfractie bij bestudering van snel ingevroren microstructuren wordt gedeeltelijk veroorzaakt door een onnauwkeurige analysemethode, veroorzaakt door de beeldanalyse van 2D doorsneden. Een 3D reconstructie van de microstructuur zou het mogelijk maken de werkelijke morfologie van de gevormde fasen te analyseren en de stolling van de legeringen nauwkeurig te beschrijven. Op basis van 3D microstructuuranalyse

is gevonden dat de overschatting van de vaste fractie veroorzaakt wordt door structuren die niet gezien worden in 2D beeldanalyse. Deze structuren zijn kleinschalige instabiliteiten die ontstaan zijn tijdens het afschrikken en die zich door coalescentie manifesteren als grotere structuren. Deze structuren geven het foutieve beeld dat ze gevormd zijn in de vaste fractie voor het moment van afschrikken. Rekening houdend met dit verschijnsel wordt de overschatting van de vaste fractie lager. De conclusie is dat de bestudeerde legeringen (Al-3 wt% Si en Al-7 wt% Cu), onder de bestudeerde stollingscondities, een stolpad vertonen dat overeenkomt met de Gulliver-Scheil benadering. 3D microstructuurreconstructie laat complexe structuren zien die veroorzaakt worden door de onbeperkte stollingscondities. Onder deze condities kunnen ontwikkelende dendrieten elkaar ontmoeten en in hun groei beperkt worden door overlappende thermische en concentratiegradiënten. Onder deze condities kunnen complexe dendrietarmen ontstaan door processen als vergroving en samenvloeien. Complexe verzamelingen van dendrietarmen worden waargenomen in 3D reconstructies van snel gestolde structuren. Deze verzamelingen worden “gekoppelde dendrietvertakkingen” genoemd, waarin dendrietarmen in elkaar groeien, convex aan de ene zijde gekoppeld met een concave vorm aan de andere dendrietarm.

Stolling van aluminiumlegeringen met een beperkt aantal vrijheidsgraden [hoofdstuk 4]. Vergroving en fragmentatie van dendrieten tijdens stolling is bestudeerd met in-situ beelden van stolling van aluminium legeringen met een hoge koper concentratie. Er is gevonden dat de kinetiek van vergroving tijdens stolling beïnvloed wordt door lokale segregatie en dendrietgroei. Tijdens de neerwaartse stolling treedt er verzadiging van legeringselementen op aan het stolfront, gevolgd door uitzakken van deze elementen van het stolfront af. Deze fluctuaties beïnvloeden de kinetiek van de lokale groei en de vergroving aan het stolfront. Tijdens opwaartse groei echter, treedt er lokale verzadiging aan het

stolfront op, gevolgd door het neerslaan van legeringselementen en ophoping aan het stolfront. Deze verdeling van elementen beïnvloedt de kinetiek van groei en vergroving. De verdeling van de rijke vloeistof werd bepaald door de geometrische verdeling van de dendrietarmen. Op basis van deze waarnemingen is gevonden dat de vergrovingsexponent, die een maat is voor de vergroving van de secundaire dendrietarmen, groter is dan gerapporteerd in de literatuur. Er is waargenomen dat deze hoge vergrovingsexponenten veroorzaakt worden door de groei van hogere-orde dendrietvertakkingen, waardoor dendrietarmen zich van elkaar verwijderen, en door competitieve groei die de werkelijke vergroving maskeert. Een nieuw mechanisme voor dendrietfragmentatie wordt voorgesteld in deze studie. Dendrietfragmentatie wordt veroorzaakt door lokale verrijking. Hogere-orde vertakkingen raken los van de dendrietstam tijdens stolling, wanneer deze omgeven zijn door een verrijkte vloeistof. Dit mechanisme veroorzaakt lokale onderkoeling door groei en elementverrijking aan de dendrietstam. Dendrietfragmentatie door lokale verrijking wordt beïnvloed door vergroving, maar voornamelijk door groei aan de tip van hogere-orde vertakkingen. Eenmaal losgeraakt kunnen deze fragmenten uitgroeien tot dendrieten met willekeurige oriëntatie (*equiaxed*). Dit fragmentatiemechanisme kan de overgang van richtingsgebonden naar equiaxed structuren versterken.

Invloed van microstructuurontwikkeling op structuurontwikkeling [hoofdstuk 5]. De stollingscondities beïnvloeden de ontwikkeling van de microstructuur. Korrelgrootte en de afstand tussen de dendrietarmen worden kleiner bij hogere afkoelsnelheden en hogere concentraties van legeringselementen (in dit geval koper). Ook de hoeveelheid eutect groeit bij toenemende Cu concentratie. De relatie tussen de afkoelsnelheid en de hoeveelheid eutect is complexer. De hoeveelheid eutect neemt toe bij koelsnelheden van 0–1 K/s en wordt kleiner bij snelheden van 1–10 K/s. Een dergelijke relatie tussen eutect en afkoelsnelheid

wordt veroorzaakt door vergroving van dendrietarmen, eutectische onderkoeling en diffusie van elementen terug in de vaste stof bij fijnere structuren. Homogeniseren en oplossen van de eutectische fasen vergroten het waargenomen effect van een verminderde hoeveelheid eutect. Structuren van *direct-chill* (DC) gegoten perspalen zijn vaak inhomogeen en bevatten een scala aan korrelmorfologiën. De 3D microstructuurreconstructie laat de werkelijke 3D structuur van de korrels in de gegoten structuur zien: grofcellige korrels, fijncellige korrels (b.v. duplex structuren) en minder ontwikkelde korrels. Een 2D stereologische correctie kan de analyse van korrelmorfologie verbeteren, maar zij kan geen onderscheid maken tussen fijncellige korrels en minder ontwikkelde korrels. Analyse van microsegregatie, gecombineerd met een analyse van de korrelmorfologie, maakt het mogelijk om de oorsprong van korrels gedurende het gietproces te achterhalen. De vorming van verschillende korreltypes kan omschreven worden als: grofcellige korrels zijn gevormd op hoge temperatuur in de bovenste laag van het stolfront en zijn arm aan legeringselementen. Als gevolg daarvan hebben ze een negatieve invloed op de segregatie op de hartlijn van een DC gegoten perspaal. Fijncellige korrels zijn gevormd op lage temperatuur, zijn rijker aan elementen, en hebben daarom een positieve bijdrage aan de segregatie op de hartlijn. Minder ontwikkelde korrels kunnen ontstaan zijn als dendrietfragmenten tijdens het gieten.

Er is aangetoond dat overgangen in de microstructuur tijdens stolling een effect hebben op de uiteindelijke structuur. Daarom kunnen ze van invloed zijn op de vorming van gietfouten. Lokale veranderingen in de vorming van de microstructuur hebben een grote invloed op de structuur op grotere schaal. Een aanbeveling is om alle factoren die een rol spelen bij de vorming van de microstructuur (dendrietvergroving, fragmentatie, coalescentie en microsegregatie) te beschouwen om de vorming van gietfouten te begrijpen.

Publications

Conference Proceedings:

1. D. Ruvalcaba, D.G. Eskin, L. Katgerman, J. Kiersch, Behaviour of the Solid-Liquid Interface at the Moment of Quenching During the Solidification of Aluminium Alloys, Ed. H.R. Müller, *Proc. Int. Conf. Continuous Casting of Non-Ferrous Alloys*, Wiley-VCH, Weinheim, 2005, pp. 290–295.
2. D. Ruvalcaba, D.G. Eskin, L. Katgerman, Quenching Study on the Solidification of Aluminium Alloys, Ed. T.J. Galloway, *Light Metals 2006: Cast Shop Technology and Recycling Aluminum*, TMS Warrandale, Pennsylvania, 2006, pp. 813–818.
3. D. Ruvalcaba, D.G. Eskin, L. Katgerman, 3D Reconstruction of Coarse Dendritic Microstructures during the Solidification of Aluminum Alloys, Ed. J. Hoyt, M. Plapp, G. Faivre, S. Liu, *Frontiers in Solidification Science*, TMS Warrandale, Pennsylvania, 2007, pp. 1–9.
4. D. Ruvalcaba, R.H. Mathiesen, D.G. Eskin, L. Arnberg, L. Katgerman, Fragmentation due to the Interaction of Solute Flow with the Dendritic Network during the Solidification of Aluminum Alloys, Ed. H. Jones, *Proc. 5th Decennial Int. Conf. on Solidification Processing*, The University of Sheffield, U.K. 2007, pp. 321–325.
5. D. Ruvalcaba, R.H. Mathiesen, D.G. Eskin, L. Arnberg, L. Katgerman, In-situ Analysis of Coarsening during Directional Solidification Experiments in High-solute Aluminium Alloys, Ed. P.D. Lee, A. Mitchel, J.-P Bellot, A. Jardy, *Proc. Int. Symp. Liquid Metal Processing and Casting*, Nancy Bialec, France, 2007, pp. 181–185.
6. D. Ruvalcaba, D.G. Eskin, L. Katgerman, 3D Visualization of Solid Phase Morphology of Al–Cu alloys in Unconstrained and Constrained Growth Conditions, *Supplemental Proc.: Volume 2: Mater. Characterization, Computation and Modeling*, TMS Warrandale, Pennsylvania, 2008, pp. 161–166.

Journal Publications:

7. D.G. Eskin, Q. Du, D. Ruvalcaba, L. Katgerman, Experimental Study of Structure Formation in Binary Al–Cu alloys at Different Cooling Rates, *Mater. Sci. Eng. A*, 2005, vol. 405, pp. 1–10.
8. D. Ruvalcaba, D.G. Eskin, L. Katgerman, 3D Microstructure of Aluminum Alloys Quenched During Solidification, *Mater. Sci. Forum*, 2006, vols. 520–521, pp. 1707–1712.
9. D. Ruvalcaba, D.G. Eskin, L. Katgerman, 3D Microstructure Development during Unconstrained Solidification of Aluminum Alloys, *Mater. Sci. Forum*, 2007, vols. 561–565, pp. 1015–1018.
10. D. Ruvalcaba, R.H. Mathiesen, D.G. Eskin, L. Arnberg, L. Katgerman, In-situ Observation of Dendrite Fragmentation due to Local Solute Enrichment during the Solidification of an Aluminum Alloy, *Acta Mater.* 2007, vol. 55, pp. 4287–4292.
11. D. Ruvalcaba, R.H. Mathiesen, D.G. Eskin, L. Arnberg, L. Katgerman, In-situ Analysis of Coarsening during Directional Solidification Experiments in High-solute Aluminium Alloys, *Metall. Mater. Trans. B*, 2009, vol. 40B, pp. 312–316.
12. D. Ruvalcaba, R.H. Mathiesen, D.G. Eskin, L. Arnberg, L. Katgerman, Influence of Dendrite Arrangement on Coarsening during Solidification of High-solute Aluminium Alloys, *Int. J. Cast Met. Res.* 2009, vol. 22, pp. 1–4.
13. D.G. Eskin, D. Ruvalcaba, C. Kwakernaak and L. Katgerman, Different Grain Morphologies in Grain-Refined 7075 Billet, *Mater. Sci. Tech.* 2009, in press.

Acknowledgments

I express my sincere gratitude to all the people who supported me for producing this thesis. I would like to thank my supervisor and tutor Prof. L. Katgerman who motivated me and helped me throughout my PhD. I am very grateful for all of his feedback and guidance during this period. Also, I would like to thank my daily supervisor and tutor Dr. D.G. Eskin who was always there to help me and guide me. I am greatly indebted to him who was very patient in reviewing the drafts of the thesis. I had excellent feedback from our industrial partners at Corus, and therefore their participation and contribution are greatly appreciated; they are: Dr. R. Kieft, Dr. W. Boender and Dr. A. ten Cate. I also had excellent feedback from my colleagues Dr. A.N. Turchin, Dr. Q. Du and Dr. R. Nadella from the former Netherlands Institute for Metals Research (NIMR).

This thesis could never have been completely realized without the contribution and excellent cooperation of Dr. R.H. Mathiesen and Prof. L. Arnberg from the Norwegian University of Science and Technology (NTNU) as part of the Nor-Light Shaped Casting cooperation project. I would like to thank them for all the support and guidance during the realization of this cooperation project. Their feedback and comments were always of great importance to me. I had a nice time in Trondheim, Norway during my visit to the NTNU. I also spent a great time at the European Synchrotron Radiation Facility (ESRF) in Grenoble, France working with Dr. R.H. Mathiesen on ongoing scientific research.

I would like to thank the technical support at the Delft University of Technology. This goes to: J. van Etten, J. Boomsma, M.A. Leeftang, C. Kwakernaak and E.R. Peekstok. Also I express my appreciation to all of my friends and colleagues at the University. I had great time working with them, going to lunch once a day and getting the coffee twice a day “Dank u wel”. I

also won't forget my good friend F.A. Slooff, who was always there to help me in many things.

I appreciate the hospitality of the Delft University of Technology and the Materials innovation institute. This research was carried out under the project MC4.02134b in the framework of the Research Program of the Materials innovation institute M2i (www.m2i.nl), the former Netherlands Institute for Metals Research.

Last but not least, I would like to thank my family for all of their support; my father: José A. Ruvalcaba Natera, my mother: Emilia Jiménez de Ruvalcaba and my brothers: Graham D. Ruvalcaba Jiménez and Jonathan A. Ruvalcaba Jiménez. I will always carry their love in my heart. Finally, I would like to thank Crystabel Salazar Monsivais, who has been there for me in the good times and bad times. She has been very kind to me since I met her during my PhD.

About the Author

Démian Gibrán Ruvalcaba Jiménez was born in Saltillo Coahuila Mexico on September 12th, 1979. He obtained a BSc in Materials Engineering and graduated “Summa Cum Laude” at the Instituto Tecnológico de Saltillo in Saltillo, Mexico (1996–2001). Later he received an MSc in Advanced Engineering Materials at the University of Manchester Institute of Science and Technology in Manchester, United Kingdom (2002–2003). Recently, he has finished working for the Materials innovation institute (the former Netherlands Institute for Metals Research). During this time (2004–2008), he worked as a PhD researcher at the Delft University of Technology with the Materials innovation institute. During his PhD, he was part of the Light Metals Processing group where he was involved in the study of the structure development during the solidification of aluminium alloys. Recently (2008–today), he joined the Molten Aluminium Processing group at Corus Research Development and Technology in IJmuiden (Corus RD&T).

